An-Najah National University

Faculty of Graduate Studies

MAGNETOCALORIC EFFECT AND ELECTRONIC PROPERTIES OF DOPED $InSb$ -DOUBLE QUANTUM WIRE IN THE PRESENCE OF EM-FIELDS AND SPIN-ORBIT TERMS

By

Mahmoud Majed Ali

Supervisor

Prof. Mohammad Elsaid

This Dissertation is Submitted in Partial Fulfillment of the Requirements for the Degree of PhD of Physics, Faculty of Graduate Studies, An-Najah National University, Nablus - Palestine.

2025

MAGNETOCALORIC EFFECT AND ELECTRONIC PROPERTIES OF DOPED $InSb$ -DOUBLE QUANTUM WIRE IN THE PRESENCE OF EM-FIELDS AND SPIN-ORBIT TERMS

By

Mahmoud Majed Ali

This Dissertation was Defended Successfully on 09 / 07 /2025 and approved by:

Prof. Mohammad Elsaid
Supervisor

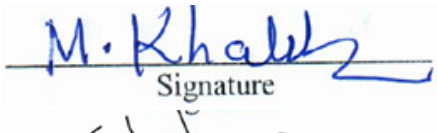

Prof. Hazem Abu Sara
External Examiner

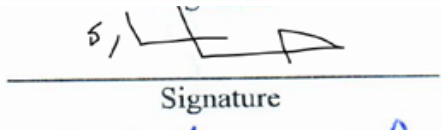

Prof. Mohammed Abu-Jafar
Internal Examiner

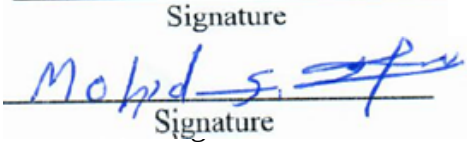

Dr. Musa Al-Hasan
Internal Examiner

An-Najah National University
Faculty of Graduate Studies

MAGNETOCALORIC EFFECT AND ELECTRONIC PROPERTIES OF DOPED $InSb$ -DOUBLE QUANTUM WIRE IN THE PRESENCE OF EM-FIELDS AND SPIN-ORBIT TERMS

By

Mahmoud Majed Ali

Supervisor

Prof. Mohammad Elsaid

In Accordance with An-Najah National University Deans Council Regulations for the award of Doctor of Philosophy, the following papers have been published after their extraction from the dissertation:

1. **Effect of structural parameters, and spin-orbit interaction on the electronic properties of double quantum wire systems in the presence of external magnetic field.**

Dedication

I dedicate this work to my parents, for their lifelong encouragement; to my wife, for her endless patience; to my daughters, Nawar and Salma, for bringing joy to my life; to my family and friends, for their unwavering support; and to my special friend, Baha Hamad, for his unwavering companionship

Acknowledgments

First and foremost, I'd want to thank Allah for helping me to finish this task. Then I am deeply grateful to my supervisor, Prof. Mohammad Elsaid, for giving me the opportunity to do this difficult task. I am thankful for his guidance, advice, encouragement, understanding, and insightful support. I also extend my thanks to my friend, Ayham Shaer, for his continuous support and encouragement.

Declaration

I, the undersigned, declare that I submitted the thesis entitled:

MAGNETOCALORIC EFFECT AND ELECTRONIC PROPERTIES OF DOPED *InSb* -DOUBLE QUANTUM WIRE IN THE PRESENCE OF EM-FIELDS AND SPIN-ORBIT TERMS

I declare that the work provided in this thesis, unless otherwise referenced, is the researcher's own work, and has not been submitted elsewhere for any other degree or qualification.

Student's Name: Mahmoud Majed Ali

Signature: M. Ali

Date: 09/07/2025

List of Contents

List of Tables

List of Figures

List of Appendices

MAGNETOCALORIC EFFECT AND ELECTRONIC PROPERTIES OF DOPED $InSb$ -DOUBLE QUANTUM WIRE IN THE PRESENCE OF EM-FIELDS AND SPIN-ORBIT TERMS

By

Mahmoud Majed Ali

Supervisor

Prof. Mohammad Elsaid

Abstract

This study provides a comprehensive theoretical analysis of the electronic, magnetic, and thermodynamic properties of a double quantum wire (DQW) system made of Indium Antimonide ($InSb$), a material known for its high electron mobility and strong spin-orbit coupling. The study investigates the effect of the structural parameters of the confining potential, Rashba spin-orbit, external electric and magnetic fields, and impurity potential on the electronic, magnetic, and thermodynamic properties. We solve the Hamiltonian by using the exact diagonalization method, and then we compute the energy spectra, probability density distributions, local density of states ($LDOS$), magnetization, magnetic susceptibility, entropy, and magnetocaloric effect (MCE) for the double quantum wire system.

Our numerical results show that the presence of the dopant potential changes the electronic structure, causing energy level shifts and breaking the symmetry between the two quantum wires. The impurity causes selective energy shifts, so that one wire undergoes large spectral changes while the other wire remains largely unchanged. Furthermore, the energy spectra and the probability density distributions analysis indicates that the quantized energy levels strongly depend on the structural parameters of the confining potential. The observed energy splitting and redistribution of probability density shows that the external fields provide a mechanism for controlling electronic properties for the system. Additionally, The effect of Rashba SOC and magnetic field variations on LDOS and spin-split state formation is explained.

The influence of temperature, SOC strength, and electric field on the magnetic properties is analyzed, focusing on the transition from diamagnetic to paramagnetic behavior. The interplay between quantum and thermal effects is discussed. Our results highlight the critical role of spin-orbit coupling and external fields in controlling the magnetic responses.

The MCE is studied by calculating entropy change and the refrigerant capacity (RC). We found that the refrigerant capacity (RC) increases nonlinearly with the Rashba spin-orbit coupling (SOC) strength. It is further enhanced when the impurity is placed at a specific position and when the external electric field is increased up to a certain value. These findings offer valuable insights for optimizing magnetocaloric materials for advanced technologies.

Keywords: Spin orbit coupling; Local density of states; Magnetization; Magnetic susceptibility; Magnetocaloric effect; Gaussian impurity; Entropy; Refrigerant capacity.

Chapter One

Introduction

The remarkable advancements in modern technology are deeply rooted in the intrinsic and tunable properties of semiconductors, which have become the foundation of the current technological era. Semiconductors possess unique electrical, optical, and thermal characteristics that can be precisely controlled through a variety of techniques, including chemical doping, strain engineering, quantum confinement, and the application of external fields. This precise control over material properties has allowed scientists and engineers to design electronic and optoelectronic devices with unprecedented performance, efficiency, and miniaturization. A key driving factor behind this technological progress is the ability to manipulate the behavior of charge carrier's electrons and holes within these materials, enabling the development of smaller, faster, and more energy-efficient components. Over the past few decades, advances in fabrication and characterization methods have further expanded the possibilities, allowing the creation of complex nanostructures such as quantum wells, nanowires, and quantum dots, where quantum mechanical effects dominate and open entirely new avenues for device functionality. These developments have had a transformative impact on a wide range of applications, including high-speed computing, advanced communication systems, infrared and visible-light optoelectronics, sensors, and emerging quantum technologies. Beyond practical applications, the study of semiconductors also provides deep insight into fundamental physical phenomena, such as carrier dynamics, spin-orbit interactions, and low-dimensional effects, which continue to inspire both theoretical exploration and technological innovation. The ongoing ability to manipulate semiconductor properties not only drives progress in current technologies but also lays the groundwork for future breakthroughs in nanoscience, quantum information processing, and energy-efficient devices [1, 2].

When semiconductor materials reduced to nanoscale dimensions, their physical properties differ from those of bulk materials due to quantum confinement effect. In particular, low-dimensional semiconductor systems exhibit unique electronic and optical properties that make them highly attractive for novel device applications. Among these systems, quantum wires are a very important type in the world of

nanostructures in which charge carriers are spatially confined in two dimensions, allowing free movement along one dimension.

Due to their exciting electronic, thermal, and optical characteristics, quantum wires have been the focus of extensive research, with a growing number of studies exploring their characteristics These structures have various technological applications, including quantum wire lasers, transistors, light-emitting diodes, sensors, solar cells, and optical filters [3-7] Over the years, various fabrication techniques have been developed to create quantum wires experimentally. Some of the most widely used methods include the vapor-liquid-solid (VLS) growth mechanism, electron-beam lithography (EBL), nano-sphere lithography, quantum well etching, and ion implantation [8, 9].

A double quantum wire (DQW) is formed when two nearly identical, quasi-one-dimensional quantum wires are placed close to each other, this achieved by introducing additional lateral confinement, which influences the electronic coupling between the two wires [10]. By carefully tuning the confinement potential, researchers can fabricate double quantum wire heterostructures with adjustable tunneling barriers, allowing precise control over carrier interactions and transport properties. These advancements enable a new device applications and help the researchers to explore quantum effects in small semiconductor structures.

1.1 Quantum confinement

Quantum confinement is a fundamental concept in nanoscience and quantum mechanics, referring to the phenomenon that occurs when the dimensions of a material are reduced to a scale comparable to the de Broglie wavelength of its charge carriers, such as electrons and holes. When the material's dimensions are reduced to the nanoscale, typically less than 100 nanometers, the electrons and holes can no longer move freely in all three dimensions. Depending on the degree of confinement, the charge carriers can be move freely in two dimensions (quantum wells), one dimension (quantum wires), or zero dimension (quantum dots). Each of these structures exhibits unique quantum behaviors, and the degree of confinement affects the energy quantization and the resulting physical properties [11-14].

In bulk materials, the electronic states form continuous energy bands, enabling the free motion of charge carriers. However, in confined systems, the energy levels become discrete due to the boundary conditions imposed on the particle's wavefunction. The smaller the dimensions of the confinement region, the larger the energy spacing between the levels, which directly impacts the material's electronic and optical properties. For instance, the bandgap of a semiconductor material can be engineered by controlling its size, leading to size-dependent optical absorption and emission characteristics—a phenomenon widely exploited in quantum dot applications [15-17].

The quantum confinement effect is obviously observed in low-dimensional systems such as nanowires, nanotubes, graphene, and quantum dots. Due to the unique properties of these systems, they are used in many fields such as light-emitting diodes ($LEDs$), solar cells, biological imaging, quantum well transistors, and quantum computing [2, 18-21].

The advances in nanofabrication techniques, such as molecular beam epitaxy, chemical vapor deposition, and colloidal synthesis, have enabled the production of high-quality nanostructures with controlled properties [8]. Moreover, advanced characterization tools, including atomic force microscopy, scanning tunneling microscopy, and ultrafast spectroscopy, are essential for probing the quantum-confined states and understanding their behavior [22].

1.2 Double quantum wires (DQW)

Double quantum wires are a specialized class of quantum confinement structures formed by two closely spaced potential wells, often separated by a thin barrier layer made from a different semiconductor material. This arrangement creates a coupled system where the behavior of charge carriers in one wire can be influenced by the presence of the other. Within such a configuration, electrons and holes are not strictly confined to their original wire; instead, they may tunnel through the barrier into the adjacent wire. The likelihood of this tunneling is strongly determined by the barrier's thickness and material properties, which affect the degree of wavefunction overlap between the two wires. A thinner barrier promotes stronger coupling, enabling significant inter-wire carrier exchange, while a thicker barrier restricts tunneling and preserves more independent carrier dynamics in each wire. This tunable coupling plays

a key role in modifying the system's transport and optical responses, making double quantum wires an attractive platform for studying quantum coherence, carrier interactions, and the influence of external fields in low-dimensional systems.

When the energy levels of the two wires match, the probability of tunneling increases significantly. This effect is used in devices such as resonant tunneling diodes [23]. Additionally, double quantum wires are used in advanced optoelectronic devices like lasers [24]. Moreover, quantum wires have also played a major and important role in the field of quantum information technologies [25].

1.3 Spintronics

Spintronics is a rapidly advancing research field which uses the spin of electrons rather than their charge. By studying spin dynamics, researchers aim to develop advanced electronic devices. The most promising applications of spintronics are the field-effect transistors and magnetoresistive random-access memory ($MRAM$) [26].

The study of spin-orbit coupling in confined quantum structures is of great importance because it plays an important role in spintronics devices. These devices are designed to operate at very high speeds and efficiency while reducing energy consumption to the lowest possible level [20, 27-29]. The key princible behind these technologies is the ability to manipulate and control the spin orientation of electrons in semiconductor structures [30-32].

Rashba spin-orbit coupling ($RSOC$) is a fundamental quantum phenomenon that emerges in low-dimensional semiconductor systems due to the presence of a macroscopic electric field, which is itself a direct consequence of structural inversion asymmetry (SIA) in the material. Structural inversion asymmetry occurs when the potential energy profile along the growth or confinement direction of the nanostructure lacks mirror symmetry, meaning that electrons on one side of the structure experience a different potential compared to the opposite side. This asymmetry generates an effective internal electric field that interacts with the motion of electrons in the plane of confinement, coupling their linear momentum to their intrinsic spin degree of freedom. As a result, the spin and orbital motion of electrons are no longer independent, leading to the characteristic Rashba spin splitting in the energy spectrum.

This spin splitting has profound implications for the electronic, optical, and transport properties of low-dimensional systems, such as quantum wells, quantum wires, and quantum dots. In these nanostructures, $RSOC$ modifies the subband structure, influences carrier scattering rates, and introduces spin-dependent transport channels, all of which are critical for spintronic applications where control over spin currents is required. One of the most remarkable aspects of $RSOC$ is its tenability, the strength of the spin-orbit interaction can be externally controlled by applying gate voltages, modifying asymmetric doping profiles, or engineering the heterostructure design. This tunability enables precise manipulation of spin states, allowing for the realization of devices such as spin transistors, spin filters, and elements for quantum computation, where the ability to coherently control electron spin is essential.

Furthermore, in coupled systems like double quantum wires, $RSOC$ plays an even more complex and intriguing role. The interplay between tunneling, confinement, and spin-orbit interaction can lead to unique phenomena such as spin-dependent interference, anisotropic spin splitting, and enhanced magneto-electric coupling. These effects not only provide a deeper understanding of fundamental spin physics in low-dimensional materials but also open pathways for engineering novel devices that exploit spin and charge simultaneously for advanced functionalities. The study of Rashba spin-orbit coupling therefore represents a critical intersection of condensed matter physics, nanotechnology, and device engineering, highlighting the importance of structural design and external field control in tailoring the quantum properties of modern nanoscale materials. $RSOC$ arises due to a macroscopic electric field, which is linked to the structural inversion asymmetry of the potential in the material. This inversion asymmetry means that the potential energy landscape along the growth direction of the structure is not symmetric. For this reason, an effective electric field is generated, which simultaneously interacts with both the electron motion as well as its spin, causing spin-orbit coupling. The Rashba spin-orbit coupling strength can be controlled by an external electric field, making it an effective and practical mechanism for controlling spin-dependent effects in spintronic devices [33].

1.4 The density of the states and the local density of states

The density of states (DOS) describes how many electronic states are available per unit energy in a material. The shape and behavior of the DOS strongly depend on the dimensionality of the system, meaning whether the electrons are confined in three, two, one, or zero dimensions as shown in FigureB1.

1. **Three-Dimensional (**$3D$**) Systems: Bulk Materials**

In a $3D$ system, such as a bulk semiconductor or metal, electrons are free to move in all three spatial directions. The density of states increases smoothly with energy. This means that in a $3D$ material, the DOS starts from zero at the bottom of the conduction band and increases with energy. The smooth increase allows for a continuous range of available states, leading to the electronic properties observed in bulk materials.

2. **Two-Dimensional (**$2D$**) Systems: Quantum Wells**

In a $2D$ system, such as a quantum well, electrons are confined in one direction but free to move in the other two. This confinement causes the DOS to take a step-like shape. Unlike the $3D$ case, where the DOS gradually increases with energy, in $2D$ systems, the DOS remains constant within each energy subband and jumps to a higher value when a new subband becomes available. This results in a layered electronic structure, which is essential in modern electronic and optoelectronic devices like MOSFETs and quantum well lasers**.**

3**. One-Dimensional (**$1D$**) Systems: Quantum Wires**

In a $1D$ system, such as a quantum wire, electrons are confined in two directions but free to move along the remaining one. As a result, the DOS in $1D$ systems exhibits sharp peaks at the onset of each energy subband. These peaks, significantly affect the electrical and optical properties of nanowires, making them highly sensitive to external perturbations such as electric and magnetic fields.

4**. Zero-Dimensional (**$0D$**) Systems: Quantum Dots**

In a $0D$ system, such as a quantum dot, electrons are confined in all three spatial directions, meaning they can only occupy discrete energy levels. This results in a discrete DOS, where states appear as a line at specific energy value. Since electrons can

only occupy certain quantized states, quantum dots behave like artificial atoms, leading to unique optical and electronic properties used in applications like quantum computing.

Table 1

The effect of spatial confinement on DOS as a function of energy

System	Dimensionality	$DOS\ vs.\ E$
Bulk	$3D$	$DOS \propto \sqrt{E}$
Quantum well	$2D$	$DOS \propto Constant$
Quantum wire	$1D$	$DOS \propto \frac{1}{\sqrt{E}}$
Quantum dot	$0D$	$DOS \propto \delta\,(E - E_n)$

In Table 1, the expressions for the DOS in different dimensionalities ($3D$, $2D$, $1D$, and $0D$) are summarized. The general shapes of the materials corresponding to each confinement type are shown in Figure26 (Appendix B). In Conclusion, as the dimensionality of a system decreases, the density of states shifts from a continuous function in $3D$ materials to discrete energy levels in $0D$ systems. This transition leads to significant changes in the electronic, optical, and transport properties of nanomaterials. Understanding these effects is crucial in designing and optimizing nanostructures for advanced electronic and photonic applications.

When a nanomaterial is subjected to an external magnetic field, the dynamics of its charge carriers, such as electrons or holes, are profoundly affected by the Lorentz force. This force causes the carriers to move in circular or spiral trajectories perpendicular to the direction of the applied field. In classical physics, these orbits are continuous, but in quantum mechanics, the motion of the carriers becomes quantized. This quantization arises from the restriction that only certain discrete energy states are allowed for electrons moving in a magnetic field, giving rise to what are known as Landau levels a phenomenon referred to as Landau quantization. Each Landau level corresponds to a quantized cyclotron orbit, and the spacing between these levels depends on fundamental parameters such as the strength of the applied magnetic field and the effective mass of the carriers. As the field strength increases, the separation between adjacent Landau levels widens, leading to more pronounced quantum effects.

The concept of Landau quantization fundamentally changes our understanding of the electronic structure of materials under magnetic fields. Instead of a continuous energy spectrum, electrons occupy discrete, highly degenerate energy states, each associated with a specific Landau level. This discretization has a direct impact on the density of electronic states in the system, producing sharp peaks at the energies corresponding to the Landau levels. These peaks significantly influence the material's transport, optical, and thermodynamic properties. For instance, in two-dimensional electron systems such as quantum wells, Landau quantization is responsible for the formation of the integer and fractional quantum Hall effects, which have been observed experimentally as quantized plateaus in the Hall resistance. Similarly, oscillatory behavior in magnetoresistance, known as Shubnikov–de Haas oscillations, arises directly from the filling and depopulation of Landau levels as the magnetic field is varied. These phenomena are not only of fundamental interest but also have practical implications for high-precision metrology and the design of nanoscale electronic devices.

In low-dimensional systems, including quantum wires, quantum dots, and double quantum wire structures, the effects of Landau quantization become even more pronounced due to the additional confinement of charge carriers. The combination of spatial confinement and magnetic quantization leads to a rich energy spectrum in which subbands of the system interact with Landau levels, producing complex splitting and shifting of energy states. In such systems, the interplay between confinement, magnetic field strength, and spin-orbit interactions, such as Rashba coupling, introduces new degrees of freedom for controlling the electronic and spin properties. For example, in double quantum wires, tunneling between the wires can couple with Landau quantization to produce spin-dependent energy dispersions, which are crucial for applications in spintronics and quantum information processing. These effects highlight the intricate connection between fundamental quantum phenomena and the engineering of nanostructured materials for advanced device functionality.

Beyond their impact on electronic properties, Landau levels also play a central role in magneto-thermodynamic phenomena. When a system is exposed to varying magnetic fields, the occupancy of Landau levels changes, modifying the magnetic entropy of the system. This effect underpins the magnetocaloric response of low-dimensional materials and has direct relevance for emerging technologies in solid-state cooling. By carefully

tuning the magnetic field and exploiting the quantized energy levels, it is possible to enhance the efficiency of energy conversion processes and thermal management in nanoscale devices. Moreover, Landau quantization affects the optical response of materials: the discrete energy levels allow for sharp, well-defined optical transitions that can be probed using spectroscopic techniques. These transitions provide direct insight into the effective mass, carrier density, and interaction effects in the system, offering a powerful tool for both fundamental research and device characterization.

In addition, Landau quantization is intimately linked to the quantum coherence and many-body interactions in low-dimensional systems. The high degeneracy of each Landau level enhances electron-electron interactions, giving rise to correlated phenomena such as Wigner crystallization, fractional quantum Hall states, and magneto-excitonic effects in nanostructures. In quantum dots, the interplay between confinement, Coulomb interactions, and Landau quantization defines the addition energy spectrum and dictates the behavior of single-electron transport, which is essential for applications in quantum computing and single-electron transistors. These effects illustrate the profound role of Landau quantization in shaping the electronic, magnetic, and optical properties of nanomaterials, highlighting its significance not only as a fundamental quantum phenomenon but also as a practical tool for designing next-generation nanoscale devices.

In summary, Landau quantization represents a cornerstone concept in condensed matter physics, providing a bridge between the fundamental behavior of charge carriers in magnetic fields and the rich physics of low-dimensional and nanostructured systems. Its influence extends across electronic transport, optical transitions, thermodynamic responses, and spin-dependent phenomena, making it a critical aspect of research in quantum wires, quantum dots, and double quantum wire systems. The ability to understand, control, and exploit Landau levels opens pathways for both fundamental discoveries and innovative applications, ranging from precision metrology to quantum information technologies and advanced magnetocaloric materials. By combining magnetic field control with nanoscale engineering, researchers can harness Landau quantization to explore novel physical effects and design devices with unprecedented performance and functionality.

The local density of states ($LDOS$) is the number of energy states per unit energy at a specific point within the material, it offers more specific insight into the electronic states at a particular location within the material, making it a highly localized measure of the system's electronic structure.

Unlike the total density of states, which provides a global average over the entire system, the $LDOS$ captures spatial variations in the electronic structure, offering a more detailed and localized perspective. It reflects how the distribution of states changes from one position to another, which is particularly important in nanostructures, heterojunctions, and systems with spatially varying potentials. By focusing on a precise location, the $LDOS$ enables direct investigation of how factors such as impurities, defects, external fields, or quantum confinement influence the accessibility of electronic states in that region. This makes it an essential quantity for analyzing and interpreting the electronic behavior of low-dimensional systems, including double quantum wires, where the spatial modulation of electronic states plays a critical role in transport and optical properties.

One of the most effective and versatile techniques for investigating the local density of states ($LDOS$) in materials is scanning tunneling microscopy (STM). scanning tunneling microscopy operates on the fundamental principle of quantum tunneling, where electrons can move across a potential barrier even when classical physics predicts that they should not. In the STM setup, a sharp metallic tip is positioned extremely close to the sample surface typically at distances of just a few angstroms. When a bias voltage is applied between the tip and the sample, electrons tunnel through the vacuum gap, producing a measurable tunneling current. The magnitude of this current is highly sensitive to the electronic states available at the precise location under the tip. Specifically, the tunneling current is directly proportional to the $LDOS$ at the tip position, which allows STM to probe the spatial distribution of electronic states with atomic-scale resolution.

By systematically varying the bias voltage, STM is capable of mapping the $LDOS$ as a function of energy, providing a direct visualization of the electronic structure across different regions of the material. This capability makes it possible to identify and characterize features such as energy gaps, impurity states, localized defect levels, and surface reconstructions. In low-dimensional systems such as quantum wells, nanowires,

quantum dots, and double quantum wire structures STM has proven to be an invaluable tool because the $LDOS$ can vary significantly over very short spatial scales due to quantum confinement effects. For example, in quantum wires, the $LDOS$ may reveal discrete subbands associated with lateral confinement, while in quantum dots, scanning tunneling microscopy can directly image the spatial distribution of confined electron states.

Furthermore, STM is instrumental in studying more complex phenomena, such as Landau quantization in the presence of a magnetic field or Rashba spin-orbit splitting in asymmetric nanostructures. When combined with external perturbations like magnetic or electric fields, scanning tunneling microscopy can provide real-space and energy-resolved insights into how these factors influence the $LDOS$. This allows researchers to observe subtle effects such as spin-dependent energy splitting, edge states in topological systems, and electron localization around impurities or interfaces. The combination of atomic spatial resolution and fine energy resolution makes STM one of the most powerful experimental techniques for connecting theoretical predictions with experimental observations in condensed matter physics.

In addition to its spatial and energy-resolving capabilities, STM can be operated in several modes to extract further information about a material. For instance, spectroscopic modes, such as scanning tunneling spectroscopy (STS), directly measure the differential conductance as a function of voltage, which is proportional to the $LDOS$ at a given energy. This enables precise characterization of electronic excitations, band edges, and energy-dependent phenomena at the nanoscale. scanning tunneling microscopy has also been used to study dynamic processes, such as electron-phonon interactions, local magnetic behavior, and charge transfer events, by monitoring variations in the tunneling current under controlled experimental conditions.

The ability of scanning tunneling microscopy to probe the $LDOS$ with such high resolution has had a profound impact on both fundamental research and technological development. It allows for a detailed understanding of the electronic properties of nanostructures, facilitates the design of spintronic and quantum devices, and provides insight into the behavior of materials under external fields or structural modifications. By combining scanning tunneling microscopy measurements with theoretical modeling,

including density functional theory and tight-binding calculations, researchers can achieve a comprehensive understanding of how local electronic states influence macroscopic properties. In this way, scanning tunneling microscopy bridges the gap between atomic-scale physics and device-level applications, offering a direct window into the quantum world.

Overall, scanning tunneling microscopy is not just a tool for imaging surfaces it is a critical technique for exploring the fundamental electronic structure of materials at the nanoscale. Its capacity to map the $LDOS$ with simultaneous spatial and energy resolution makes it indispensable for studying quantum confinement effects, spin-orbit interactions, magneto-thermodynamic phenomena, and other nanoscale properties. As nanotechnology and quantum device engineering continue to advance, STM will remain a cornerstone method for understanding and manipulating the electronic behavior of low-dimensional and nanoscale systems, providing insights that are both scientifically profound and technologically transformative.

Scanning Tunneling Microscopy (STM) is based on a quantum mechanical tunneling, small particles like electrons (show wave-like properties), penetrate potential barriers. In general, STM involves a very sharp conductive tip that is brought within tunneling distance (few nanometers) of the sample surface, then the tunneling wave function of the sample electrons (ψ_s) and the wave function of a STM tip electrons (ψ_t) overlap in the insulating gap as shown in figure 27 (Appendix B), (we consider the square magnitude of the wave function, which represents the probability of finding an electron at a given location), allowing a current to flow.

In metals, electrons fill the continuous energy levels up to the Fermi level (E_F), which defines an upper boundary, we can raise the Fermi level by applying a voltage. Thus, to observe the tunneling current I of electrons through the vacuum gap between the sample and the tip, a bias voltage, V_{bias}, is applied, as shown in figure28 (Appendix B), at $V_{bias} = 0$, the electrons cannot flow in either direction ,when $V_{bias} > 0$ (positive bias), the Fermi level of the sample is raised by V_{bias}, and the electrons in the occupied state of the sample can tunnel into the unoccupied state of the tip. Similarly, when $V_{bias} < 0$ (negative bias), the electrons in the occupied state of the tip tunnel into the unoccupied state of the sample.

In semiconductor as shown in figure 29 (Appendix B), the filled area is not uniform, there is a variation in the electrons density, and the unoccupied levels have a variation in density of the energy levels that the tunneling electrons can occupy.

The tunneling current strongly affected by the density of states (DOS) of the sample at the surface [34],

$$I \propto \int dE\ \rho_s(r,E)\ \rho_t(E-eV)(\ f(E-eV)-f(E)) \tag{1.1}$$

Where $\rho_s(r,E)$ is the local density of states of the sample at the position of the tip, ρ_t is the tip density of states , e is the electron charge, V is the voltage bias applied to the sample and $f(E)$ is the Fermi-Dirac distribution.

The STM current is able to provide a local information, $LDOS$ rather than average DOS, where the tunneling current I is recorded at each location with bias voltage V_{bias}, STM tunneling spectroscopy ($I-V$ curve) generating a map of tunneling conductance I/V_{bias} .Assuming that the tip density of state (ρ_s) is flat in the choised applied energy range , by taking the derivative of the current with respect to the bias voltage (V_{bia}) , we have the differential conductance found to be directly proportional to the sample's local density of state [35].

$$\frac{dI_t}{dV_{bias}}(r) \propto \rho_s(r,E) = \sum_0^\infty \int \psi^2\ \delta\left(E-E_n(k)\right)dk \tag{1.2}$$

The scanning tunneling spectroscopy (STS), is a local way, that can be used to obtain information about the density of states of the nanomaterial sample. We vary the bias voltage and record the tunneling current.

STS is one of the most powerful techniques for probing the quantization of Landau levels (LLs). These LLs appear as a clear sequence of peaks in the differential conductance ($\frac{dI}{dV}$) spectra which is proportional to ρ_s of the sample. The measurements of LLs quantization have been observed and reported experimentally in different nanomaterial material systems like graphene presented in an applied magnetic field [36].

1.5 Magnetocaloric effect

The magnetocaloric effect (MCE) is a fundamental thermodynamic phenomenon observed in magnetic materials, characterized by a change in temperature when the material is subjected to a varying external magnetic field. At its core, the magnetocaloric effect arises from the intimate coupling between the magnetic degrees of freedom of a material and its thermal energy. When a magnetic field is applied, the magnetic moments of atoms, ions, or electrons within the material tend to align with the field. This alignment reduces the disorder in the magnetic subsystem, effectively decreasing the magnetic entropy. Under adiabatic conditions, where no heat is exchanged with the surroundings, the reduction in magnetic entropy must be compensated by an increase in the thermal energy of the lattice, resulting in a measurable rise in temperature. Conversely, when the external magnetic field is decreased or removed, the magnetic moments tend to adopt more random orientations, increasing magnetic entropy and causing the material to cool. This reversible heating and cooling behavior forms the basis of the MCE and represents a direct manifestation of the interplay between magnetic order and thermal energy in condensed matter systems.

The strength and magnitude of the MCE are influenced by several intrinsic and extrinsic factors. Intrinsic factors include the magnetic moment of the constituent atoms, the type of magnetic ordering present (ferromagnetic, antiferromagnetic, or paramagnetic), and the nature of the magnetic interactions within the material. Materials that undergo sharp magnetic phase transitions, particularly ferromagnetic-to-paramagnetic transitions near their Curie temperature, often exhibit the strongest magnetocaloric responses, as even a small change in the magnetic field can induce a substantial change in magnetic entropy. Extrinsic factors include the strength and rate of change of the applied magnetic field, the dimensionality of the system, and the presence of structural or compositional modifications. In low-dimensional systems, such as thin films, nanowires, quantum dots, and double quantum wire structures, quantum confinement and reduced dimensionality can significantly modify the density of magnetic states and amplify the sensitivity of the system to external fields, potentially enhancing the magnetocaloric effect compared to bulk counterparts.

The practical significance of the MCE extends beyond fundamental physics. One of its most widely studied applications is in solid-state magnetic refrigeration, which leverages the reversible heating and cooling of magnetocaloric materials under varying magnetic fields to transfer thermal energy without relying on environmentally harmful refrigerants. Compared to traditional gas-compression refrigeration systems, magnetic refrigeration offers higher energy efficiency, reduced mechanical complexity, quieter operation, and a smaller environmental footprint. By carefully engineering the composition, crystallinity, and nanostructure of magnetocaloric materials, it is possible to tailor the temperature range, entropy change, and thermal conductivity for specific cooling applications, ranging from household appliances to industrial-scale thermal management systems.

Beyond refrigeration, the magnetocaloric effect plays a crucial role in biomedical applications, such as magnetic hyperthermia for cancer therapy. In this technique, magnetic nanoparticles, quantum dots, or nanowires are introduced into tumor tissue. When exposed to an external alternating magnetic field, these materials generate localized heating due to the magnetocaloric effect, raising the temperature of the targeted tissue to a level that can damage or destroy cancerous cells without affecting surrounding healthy tissue. The tunability of the MCE through material composition, particle size, and external field strength provides a high degree of control over the heating process, making it a promising tool for precision medical treatments.

From a theoretical perspective, studying the magnetocaloric effect in low-dimensional and nanoscale systems, including double quantum wire structures, also offers deep insight into the interplay of quantum confinement, spin-orbit interactions, and magnetic ordering. For instance, in systems where Rashba spin-orbit coupling is present, the splitting of spin states can alter the magnetic entropy landscape, influencing the magnetocaloric response in ways that can be harnessed for advanced device applications. Similarly, the presence of Landau quantization in strong magnetic fields can modify the density of electronic states, further impacting the magnitude and behavior of the MCE. These considerations underscore the importance of carefully designed experiments and theoretical models to predict and optimize the magnetocaloric performance of nanostructured materials.

In conclusion, the magnetocaloric effect represents a unique and versatile bridge between magnetic, thermal, and quantum properties of materials. Its study not only deepens our understanding of fundamental condensed matter physics but also provides a pathway for innovative applications in energy-efficient cooling technologies, biomedical treatments, and nanoscale devices. By exploring the MCE in both bulk and low-dimensional systems, researchers can uncover new strategies to manipulate magnetic entropy, optimize thermal performance, and design next-generation materials with tailored magnetothermal properties, highlighting the continuing importance and transformative potential of this remarkable phenomenon.

The magnetocaloric effect refers to the change in temperature of a magnetic material when it is exposed to a varying magnetic field. This effect can lead to either heating or cooling, depending on whether the magnetic field is applied or removed, as illustrated in figure30 (Appendix B). The fundamental reason behind this effect lies in the behavior of magnetic moments in response to an external magnetic field.

When a magnetic field is applied adiabatically to a magnetic material, the magnetic moments within the material tend to align with the field. This alignment reduces the magnetic contribution to the total entropy of the system. Since the process is adiabatic, the total entropy

$$S\,(T,B) = S_{\text{magnetic}}(T,B) + S_{\text{lattice}}(T) + S_{\text{electronic}}(T) \qquad (1.3)$$

must remain constant. When the magnetic field is applied, the decrease in the magnetic entropy must be compensated by an increase in the lattice entropy, to keep the total entropy constant. This increase in lattice entropy corresponds to an increase in the temperature, causing the material to heat up.

On the other hand, when the magnetic field is adiabatically removed, the previously aligned magnetic moments become disordered. This increases the magnetic entropy, requiring a decrease in the lattice entropy to keep the total entropy constant. As a result, the material cools down.

The magnetocaloric effect is typically quantified using two main parameters:

1. Isothermal entropy change (ΔS_{iso}): This measures the change in entropy of the system when the magnetic field is varied while keeping the temperature constant.

2. Adiabatic temperature change (ΔT_{ad}): This represents the change in temperature of the material when the magnetic field is altered under adiabatic condition (no heat exchange during field variation).

The adiabatic temperature change, ΔT_{ad}, can be determined experimentally by directly measuring the temperature using a thermometer. Alternatively, it can be estimated indirectly using specific heat and magnetization data, according to the following relation: [37],

$$\Delta T_{ad} = -\int_{B_i}^{B_f} \frac{T}{C_B} \left(\frac{\partial M}{\partial T}\right)_B dB \tag{1.4}$$

The isothermal entropy change, ΔS_{iso}, can be calculated by using the magnetization data as follows: [37],

$$\Delta S_{iso} = \int_{B_i}^{B_f} \left(\frac{\partial M}{\partial T}\right)_B dB \tag{1.5}$$

One of the important applications of the magnetocaloric effect lies in the field of medical treatments, particularly in targeted cancer therapy. A specialized technique known as magnetic hyperthermia utilizes this principle to selectively heat cancerous cells without causing significant damage to surrounding healthy tissue. In this approach, magnetic nanomaterials—such as quantum dots, magnetic nanoparticles, or nanowires—are introduced into the tumor site. When subjected to an external, time-varying magnetic field, these nanomaterials dissipate energy in the form of localized heat due to magnetic relaxation and hysteresis losses. This controlled temperature rise, this can weaken or destroy cancer cells by disrupting their metabolic processes and structural integrity. The localized nature of the heating allows for precise targeting, making magnetic hyperthermia a promising complementary technique to conventional cancer treatments such as chemotherapy and radiotherapy, while potentially reducing systemic side effects [38].

Another major and rapidly developing application of the magnetocaloric effect is in the field of magnetic refrigeration, which is currently considered one of the most promising alternatives to conventional cooling technologies. Traditional refrigeration systems rely on gas-compression cycles, typically using refrigerant gases such as hydrofluorocarbons ($HFCs$) or chlorofluorocarbons ($CFCs$), which not only consume significant amounts of

energy but also contribute to environmental problems, including global warming and ozone layer depletion. In contrast, magnetic refrigeration is based on the solid-state properties of magnetocaloric materials, eliminating the need for harmful refrigerants and offering a much more sustainable cooling approach. The principle relies on the reversible temperature changes of these materials when exposed to a changing magnetic field: as the field is applied, the magnetic moments of the atoms in the material tend to align, reducing magnetic entropy and causing the material to heat up; when the field is removed, the magnetic moments become disordered, increasing entropy and cooling the material. This cyclic process allows for highly efficient heat exchange with minimal energy losses. Beyond energy efficiency, magnetic refrigeration offers several additional advantages, including quieter operation, fewer moving mechanical parts, and the potential for miniaturization, which makes it suitable not only for household appliances but also for industrial, electronic, and medical cooling applications. Current research is focused on discovering and engineering materials with strong magnetocaloric effects near room temperature, optimizing their thermal conductivity, and designing practical devices capable of achieving large-scale, efficient, and environmentally friendly refrigeration. The development of magnetic refrigeration thus represents a significant step toward sustainable technology, combining fundamental physics, materials science, and engineering to address both energy efficiency and environmental concerns.

The magnetocaloric effect (MCE) in diamagnetic materials is generally very weak, especially when compared to the pronounced effects observed in ferromagnetic and paramagnetic materials. This disparity stems from the intrinsic magnetic properties of diamagnetic systems. Unlike ferromagnets, which possess permanent magnetic moments that can align under an external field, diamagnetic materials do not have inherent magnetic moments. Instead, their magnetic response is induced only in the presence of an applied external field and is typically small in magnitude, acting in opposition to the field. As a result, when the magnetic field is varied, the induced changes in magnetic entropy are minimal, leading to correspondingly tiny temperature variations. These changes are insufficient to generate the substantial heating or cooling necessary for practical applications such as magnetic refrigeration. In contrast, ferromagnetic materials exhibit strong alignment of their intrinsic moments under an external field, producing significant entropy changes and large temperature shifts, which

are critical for achieving efficient cooling cycles. Because of this, diamagnetic materials are rarely considered suitable for magnetocaloric applications where a pronounced thermal response is essential. Nevertheless, studying the weak MCE in diamagnets provides valuable insight into the fundamental mechanisms of magnetism and the role of intrinsic versus induced magnetic moments in determining a material's thermodynamic response. Furthermore, this understanding underscores the importance of material selection in designing magnetocaloric devices: choosing materials with strong magnetic ordering and high susceptibility ensures a larger entropy change and, therefore, greater efficiency in magnetic cooling technologies. By highlighting these limitations, researchers can better focus on optimizing material properties, such as magnetic moment density, Curie temperature, and lattice interactions, to maximize the performance of magnetocaloric systems for practical applications.

However, despite their weak MCE, diamagnetic materials have important applications in a high sensitive magnetic field sensor [39-41]. Such sensors can detect extremely weak magnetic fields with high sensitivity, making them valuable in various advanced technologies.

Due to these advantages, researchers are actively working on developing high-performance magnetocaloric materials and optimizing their properties for practical applications [37, 42].

1.6 Indium Antimonide ($InSb$) properties

Indium antimonide ($InSb$) is a binary compound semiconductor made of indium (In) and antimony (Sb). It belongs to the III-V group of semiconductors, which are widely studied due to their excellent electronic and optical properties [43]. $InSb$ crystallizes in the zinc blende structure. One of the most important characteristics of $InSb$ is its narrow bandgap, which is approximately 0.17 eV at room temperature. Because of this small bandgap, electrons in $InSb$ require only a small amount of energy to move from the valence band to the conduction band. This property allows $InSb$ to be highly responsive to infrared radiation, making it one of the best materials for infrared detectors [44]. Some key properties of $InSb$, including its bandgap and electron mobility, are listed in Table 2. In addition to its narrow bandgap, $InSb$ has very high electron mobility, meaning that electrons can move through the material with very little resistance. This

property makes $InSb$ highly suitable for high-speed electronics, where fast response is required. Furthermore, the combination of its electronic properties and quantum mechanical effects makes $InSb$ an important material for quantum devices, such as those used in quantum computing and spintronics [45, 46].

The unique characteristics of $InSb$ arise from its small effective mass of charge carriers, high carrier mobility, and low bandgap energy. These properties enable efficient operation in the infrared spectral range, making $InSb$ a preferred choice for thermal imaging cameras, spectroscopy equipment, and night vision systems [43, 47]. Furthermore, its high sensitivity to magnetic fields and low thermal conductivity make it a valuable material for Hall effect sensors and thermoelectric devices [48].

In recent years, significant advancements in material synthesis and characterization techniques have made it possible to fabricate high-quality indium antimonide ($InSb$) nanostructures with remarkable precision and control. These developments have enabled the creation of a variety of low-dimensional systems, including quantum wells, nanowires, and quantum dots, each offering unique electronic and optical properties. The ability to engineer $InSb$ at the nanoscale allows researchers to precisely tune parameters such as size, shape, composition, and confinement potential, which directly influence quantum confinement effects, carrier mobility, and spin-orbit interactions. High-quality fabrication also minimizes defects and impurities, ensuring that the intrinsic properties of $InSb$ dominate the observed behavior, which is critical for both fundamental studies and technological applications. These nanostructures have attracted extensive interest for use in high-speed electronics, infrared optoelectronic devices, spintronic systems, and quantum information processing, highlighting the versatile and transformative potential of $InSb$-based nanoscale materials in modern condensed matter physics and device engineering.

Table 2

Material Properties of InSb Quantum Wire [14, 49-52]

Property	Value/Description
Crystal Structure	Zinc blende
Lattice Constant	6.479 Å
Bandgap	0.17 eV (at 300 K)
Electron Mobility	~77,000 $cm^2/V{\cdot}s$ (at 300 K)
Hole Mobility	~850 $cm^2/V{\cdot}s$ (at 300 K)
Dielectric Constant	~16.8
Effective Mass	Electron: $0.015m_n$; Hole: $\sim 0.41m_n$
Landé $\boldsymbol{g}$ −factor	~ 50
Melting Point	~525 °C
Magnetic Properties	Diamagnetic
Density	~5.78 g/cm^3
Refractive Index	~ 4.0 (at 10 μm)
Intrinsic Carrier Concentration	~ 10^{12}

1.7 Literature survey

Researchers have been interested in the low-dimensional systems: Quantum wells, single quantum Wires and quantum dots, and a large number of theoretical researches have been carried out to investigate the effect of external fields on thermal, magnetic, and optical properties of these nanosystems [53-57]. In Ref [53], Gumber et.al. have calculated the heat capacity and the entropy of the cylindrical quantum dot as function of temperature, confinement strength and magnetic field. In addition, they have displayed a contour plot for the magnetic phase transition in the zero-dimensional quantum dot system made for GaAs material.

The researchers found that the presence of impurities has a significant effect on the properties of the systems [58-65]. Abu Alia et.al. have used the exact diagonalization method to calculate the effect of donor impurity and magnetic field on the heat capacity of quantum dot made from GaAs material. They found that the impurity had great effect on the QD-heat capacity [55]. In Ref. [62], for single doped-quantum wire made of GaAs, Hosseinpour found that the attractive impurity reduces the energy eigenvalues, as compared to the repulsive impurity and influence significantly the thermal properties also. Many theoretical works have investigated the effect of Rashba and Dresselhaus spin-orbit coupling on the physical properties of the low-dimensional systems [66-70].

The influences of external fields upon both the electronic and transport properties of the DQW system, have been analyzed theoretically [71-73] and experimentally [74]. The effect of a tilted magnetic field on the modulation of tunneling, conductance and the magnetization is studied for GaAs double quantum wires in reference [72, 75]. Gudmundsson et al. have made a theoretical study of the magneto transport properties of a parabolic double quantum wires made of GaAs in an external perpendicular magnetic field [75], Yenal Karaaslan et al. have investigated the electronic structure, spin and transport properties of InAs double quantum wires subjected to an external magnetic field by taking into account Rashba and Dresselhaus spin-orbit couplings [76].

The electronic transport properties of double QWs made of GaAs by considering impurity and external magnetic field were investigated by Korepov [77]. Sevil Sarikurt et al. investigated theoretically the effect of spin–orbit coupling on the energy level spectrum of $GaAs$ quantum wire with a parabolic confining potential subjected to the perpendicular magnetic field [78]. The effects of Rashba spin–orbit interaction on the electronic energy dispersion and zero-temperature conductance of $InAs$ double quantum wire under the influence of perpendicular magnetic field had been investigated in reference [79], the computed results show that the competition between spin-orbit interaction and magnetic field modify strongly energy band structure of the $DQWs$. Yenal Karaaslan et al. studied the influence of electric field on the electronic energy band structure and the optical properties of double quantum wire made of $InAs$ exposed to a perpendicular magnetic field and Rashba and Dresselhaus spin-orbit interactions [80].

The magnetocaloric properties of diamagnetic materials have been studied [81, 82]. It turns out that both entropy and temperature change cause oscillations when the applied field is varied. Alisultanov studied the effect of the diamagnetic film thickness on the magnetocaloric effect in presence of transverse magnetic field [83]. In addition ,anthers have been investigated the oscillating magnetocaloric effect on a quasi-one-dimensional electron gas with parabolic confinement potential, with and without applied magnetic field [84].

Many researchers have been interested in studying the local density of states spectra and compare the reported experimental ($LDOS$) results [22, 85, 86], with the theoretical ones [87, 88] for various quantum systems. In reference [88] the effect of the dielectric

permeability on the local density of states of the superlattice have been studied. The researchers calculated the local density of states using Green's functions for a photonic crystal of alternating air and semiconductor layers ($GaAs, Si, and\ SiO2$) and then studied the effect of pressure on the local density of states [87]. Cristina Bena and Steven A. Kivelson calculated the local density of states in graphite theoretically in presence of impurity [89]. The authors in reference [90] obtained the local density of states in Graphene numerically by using the tight-binding model.

The unique properties of $InSb$ nanostructures make them highly suitable for various applications in optoelectronics and spin-based devices, attracting significant research interest in studying their characteristics.

The effect of the applied magnetic field, Rashba and Dresselhaus spin orbit interaction on the photoconductivity of $InSb$ single-nanowire has been experimentally studied in reference [91]. In reference [92] the authors theoretically calculated the conductivity of an InSb quantum wire subject to Rashba spin-orbit coupling and a perpendicular magnetic field. The authors in reference [93] calculated the binding energy of a hydrogen-like impurity in a thin size-quantized wire of the $InSb/GaAs$ semiconductors with presence of external magnetic field. The spin flip time has been theoretically studied for $InSb$ nanowire with spin–orbit coupling in a magnetic field in reference [94]. In reference [95] the local density-of-state spectra in $InSb$ micro grains have been studied experimentally using the scanning tunneling microscope.

The exceptional material properties of $InSb$ semiconductors, combined with their potential applications in next-generation quantum devices, make them an ideal candidate for theoretical investigation. In this study, we focus on an InSb-based double quantum wire (DQW) system, a crucial step toward developing scalable quantum nanotechnology.

1.8 Research gap

Motivated by the unique material properties of $InSb$ semiconductors and its device potential applications, we have chosen $InSb$ as a research material to study theoretically a system consisting of $InSb$ double quantum wire which is a key step in achieving scalable quantum nanotechnology devices. We have calculated the MCE which has not been studied before for a double quantum wires made from $InSb$. This research will be

a source of very important theoretical information about the roles of the impurities, SOC and the electric field on MCE, magnetic, thermal, electronic properties as well as how to control them in a double quantum wire fabricated from $InSb$ nanomaterial. The focus will be on obtaining noticeable changes, in both, the entropy and thus the change in temperature, at any small variation in the magnetic field. These results will have future device applications in sensitive magnetic field sensors. We have studied the magnetic susceptibility, and investigate the expected magnetic susceptibility oscillations and the magnetic phase transitions in the material sample. The dependence of these physical quantities on the applied fields, Spin-orbit interactions and impurity have been theoretically studied. To our knowledge the MCE for DQW made from $InSb$ nanomaterials has not been studied before. This encourages us to investigate the MCE in DQW made from one dimensional nanomaterial, $InSb$, as a research target in this work.

1.9 Research objectives

The main objectives of this research work can be summarized as follows:

1. provide a numerical solution of single-particle full-Hamiltonian of an electron confined in the double quantum wire (DQW) which is made of Indium Antimonide ($InSb$) nanomaterial taking into consideration the Rashba spin-orbit coupling, the presence of an external magnetic and electric fields and the impurity potential. The computed eigenenergies and eigenfunctions, as an output significant spectroscopic data of the nanomaterial, will be used to display the dependence of the density of states as function of various physical quantities.

2. Investigate the transport properties of the $InSb$ -DQW by calculating the local density of states $LDOS$ of an electron in DQW which has close link to the differential conductance of the material quantum wire measured by scanning tunneling spectroscopy technique (STS). The $LDOS$ spectra will be displayed against the applied fields, Rashba terms and impurity effects.

3. Study the quantum oscillation phenomena in the magnetic quantities of the DQW like magnetization, magnetic susceptibility. The influence of the impurity position and strength of the Gaussian-type potential on the properties of DQW will be studied.

4. Study the behavior of the magnetocaloric effect (MCE) under the influence of applied fields, impurities and Rashba Spin-Orbit terms. The change in the entropy of the DQW will be computed as function of the Hamiltonian physical parameters.

1.10 Structure of dissertation

The dissertation is structured into four chapters as follows:

Chapter One: Introduction: This chapter provides a comprehensive introduction to the quantum confinement of charge carriers, spintronics, local density of states, and magnetocaloric effect. It also highlights the primary differences between the current research and previous studies in the research gap section. Additionally, it includes a literature review of prior work related to the confinement in double quantum wires, numerical methods, and spin-orbit interaction studies.

Chapter Two: Theory: The second chapter details the construction of the Hamiltonian for an electron in a double quantum wire, including the effects of an external magnetic and electric field, the presence of a Gaussian impurity, and Rashba spin-orbit coupling. It also describes the numerical method used to solve the Schrödinger equation through the exact diagonalization method and explains the physical significance of the calculated properties, such as the energy spectra of the electron, probability density, statistical average energy, local density of states, magnetization, and magnetic susceptibility. Furthermore, this chapter presents all the necessary mathematical expressions and steps for simplifying the Hamiltonian matrix.

Chapter Three: Results and Discussion: This chapter shows the calculated results through figures and tables, providing both physical and mathematical analyses of the properties of double quantum wires.

Chapter Four: Conclusion: The final chapter summarizes the findings of the research, associating to the results presented in Chapter 3, and provides conclusive remarks on the implications of the study.

Chapter Two

Hamiltonian Theory and Computation Method

2.1 Hamiltonian and physical Interpretation

The total Hamiltonian which describes the motion of an electron in a doped double quantum wire (DQW) subjected to an external electric field along the x-direction and a magnetic field along the z-direction, in the presence of the Rashba spin-orbit coupling. The Hamiltonian is expressed as:

$$\widehat{H} = \frac{(\vec{p}-e\vec{A})^2}{2m^*} + V_{\text{conf}}(x) + H_{\text{electrical}} + V_{\text{imp}}(x) + H_R + H_{\text{Zeeman}} \quad (2.1)$$

where each term represents a specific contribution to the electron's energy in the DQW system:

The first term, $\frac{(\vec{p}-e\vec{A})^2}{2m^*}$, describes the kinetic energy of the electron. Here, $\vec{\mathrm{p}}$ is the momentum operator, e is the electron charge, $\vec{\mathrm{A}}$ is the magnetic vector potential associated with the external magnetic field, and m^* is the effective mass of the electron in the $InSb$ medium.

2.1.1 DQW confinement potential

The confinement potential plays a critical role in shaping the electronic properties of the system. It governs the spatial confinement of the electron wavefunctions, determining the quantized energy levels in the nanostructure. For the DQW, the confinement potential is expressed as:

$$V_{\text{conf}}(x) = \frac{1}{4}\lambda\left(x^2 - \frac{\mu^2}{\lambda}\right)^2 \quad (2.2)$$

where:

λ is a parameter that controls the strength of the confinement. A larger λ results in a steeper potential well, leading to stronger confinement of electrons.

μ represents the separation between the minima of the double-well potential, which corresponds to the spatial separation of the two wells in the DQW system. x is the position variable along the direction of confinement (typically the x-direction in this case).

The DQW potential has the following Features:

- Double-wire nature: The form of $V_{conf}\ (x)$ ensures the potential has two symmetric minima located at $x = \pm\sqrt{\mu^2/\lambda}$. These minima correspond to the locations of the two wells in the DQW system.

- Barrier between the two wires: The barrier height, separating the two wells, is proportional to the parameter $\mu^2/(4\lambda)$. A larger μ increases the separation between the wires and increases the barrier height, reducing tunneling between the wells.

- Effective confinement for electron: near each wire's minimum, the potential can be approximated as a harmonic oscillator: $V_{conf} \approx \frac{1}{2}k_{eff}(x - x_o)^2$ where k_{eff} is an effective spring constant determined by λ and the curvature of the potential at the minima. This leads to quantized energy levels in each wire.

- The separation between quantized levels depends on k_{eff} which is proportional to λ

- Tunneling between the two wires: the finite barrier allows quantum tunneling between the wires. The tunneling rate depends on the barrier height.

2.1.2 Electric field

The interaction of an electron in the double quantum wire (DQW) with an external electric field applied along the x-direction is represented by the term:

$$\widehat{H}_{electrical} = eFx \tag{2.3}$$

where:

- e is the electron charge,

- F is the strength of the electric field, applied along the x-axis,

- x is the position operator along the x-direction.

The electric field potential has the following Features:

- Linear Potential from the Electric Field: the term eFx represents the potential energy of an electron in a uniform electric field. This arises because the electric field exerts a force on the charge, resulting in a linear energy gradient along the x-direction.

- Modification of the Confinement Potential: When the electric potential combined with the confinement potential $V_{conf}(x)$, the total potential experienced by the electron becomes asymmetric

- This tilting of the potential leads to different energy levels for each wire of the DQW; The well on the side closer to the negative x-direction (where eFx is lower) will have a lower potential energy.

- Control of electron states: the electric field provides a tool to control electron dynamics in the DQW.

2.1.3 Impurity Potential

The impurity in the DQW is modeled as a Gaussian impurity

The impurity potential is represented as:

$$V_{imp}(x) = \mathrm{V_0 e}^{-\frac{(\mathrm{x}-\mathrm{x_1})^2}{\mathrm{d}^2}} \tag{2.4}$$

where $\mathrm{V_0}$ represents the impurity strength, $x_1$denotes the impurity position, and d is a tunable parameter that controls the spatial extent of the impurity. The Gaussian form ensures that the impurity potential is localized, with its maximum value occurring at $x_1 = x$ and decaying smoothly away from this point.

$\mathrm{V_0}$ determines whether the impurity acts as a potential well ($\mathrm{V_0} < 0$), which attracts charge carriers, or as a potential barrier ($\mathrm{V_0} > 0$), which repels them. The width of the impurity region is controlled by d, with smaller values leading to a sharply localized impurity and larger values resulting in a more extended potential.

Since this impurity potential introduces an additional energy contribution to the system, it significantly influences the electronic properties of the DQW. Depending on its position, the impurity may affect one or both wires, modifying charge distribution, tunneling processes, and quantum states.

2.1.4 Rashba Spin-Orbit Coupling

The Rashba spin-orbit coupling arises from structural inversion asymmetry in the double quantum nanowire (DQW), often induced by the external electric field apply on the nanostructure. The Hamiltonian for Rashba spin-orbit coupling is given as:

$$\widehat{H}_R = \frac{\alpha_R}{\hbar}\left[\sigma_x\left(p_y + eBx\right) - \sigma_y p_x\right] \tag{2.5}$$

Where:

- α_R: Rashba spin-orbit coupling parameter, which quantifies the strength of the coupling. It depends on the applied electric field and the material's properties.
- $\hbar$: Reduced Planck's constant.
- $\sigma_x = \begin{pmatrix} 0 & 1 \\ 1 & 0 \end{pmatrix}$, $\sigma_y = \begin{pmatrix} 0 & -i \\ i & 0 \end{pmatrix}$: x and y-components of the Pauli matrices, which describe the spin degree of freedom.
- p_x, p_y: Components of the electron momentum operator.
- eBx: Term arising from the vector potential of the applied magnetic field along the z-direction, in the Landau gauge.

The Rashba term couples the electron's spin with its momentum components p_x, p_y and the magnetic field B. The coupling introduces spin splitting in the electron energy spectrum, even without an external magnetic field, due to the asymmetric potential environment. The eBx term reflects the orbital effects of the magnetic field on the spin-orbit coupling. It modifies the spin-dependent energy levels and introduces a field-dependent contribution to the Rashba interaction.

2.1.5 Zeeman Effect in the Double Quantum Nanowire (DQW)

The interaction between the electron's spin and the external magnetic field is described by the Zeeman effect. This interaction is modeled by the Zeeman Hamiltonian:

$$\widehat{H}_{Zeeman} = \frac{1}{2} g^* \mu_B B \sigma_z \tag{2.6}$$

Where:

- g^* is the effective Lande g-factor, a material-dependent constant that characterizes the strength of the coupling between the magnetic moment and the external magnetic field.
- μ_B: Bohr magneton, representing the magnetic moment of an electron due to its spin.
- σ_z=$\begin{pmatrix} 1 & 0 \\ 0 & -1 \end{pmatrix}$: z-component of the Pauli matrices, which represents the projection of the electron spin along the z-axis (the direction of the applied magnetic field).

The Zeeman interaction splits the electron's spin states into two energy levels, depending on the spin orientation relative to the magnetic field, $E_{\pm} = \pm\frac{1}{2} g^* \mu_B B$ where B is the magnitude of the external magnetic field.

- The + corresponds to the spin state aligned with the magnetic field.
- The $-$ corresponds to the spin state anti-aligned with the magnetic field.

The energy splitting between the two spin states is proportional to the applied magnetic field strength and the Landé g $-$factor. In materials like $InSb$ g^* can be very large ($g^* \sim 50$) [96], resulting in a pronounced Zeeman effect even at low magnetic fields. By tuning the external magnetic field, the energy splitting can be controlled, providing a mechanism for manipulating spin states. This is essential for spin-based devices; such as spin filters or quantum bits in spintronic applications.

In $DQWs$, the Zeeman effect works in conjunction with Rashba spin-orbit coupling. Rashba creates spin-splitting depends on the momentum, while the Zeeman effect provides a constant spin-splitting. The combined effects lead to a complex spin textures in the energy bands.

2.2 Analytical expressions of the energy matrix elements

The energy eigenfunctions of the Hamiltonian can be expressed in terms of plane waves due to translational invariance along the y-direction as:

$$\psi(x,y) \;=\; \varphi(x)\, exp(ik_y\, y) \tag{2.7}$$

where k_y represents the wave numbers of the plane wave along the *y*-direction. The Schrödinger equation becomes separable in *x* and *y* and accordingly the Hamiltonian ($H = H_1 + H_2 + H_R + V_{imp}$) can be rewritten as:

$$H_1 = \left[-\frac{\hbar^2}{2m^*}\frac{d^2}{dx^2} + \frac{1}{2}m^*\omega^2(x-x_0)^2 + \frac{\omega_0^2}{\omega^2}\frac{\hbar^2 k_y^2}{2m^*}\right]\sigma_0 \;+\frac{1}{2}g^*\mu_B B\sigma_z, \tag{2.8}$$

$$H_2 = \left[-\frac{1}{2}(m^*\omega_0^2+\mu^2)x^2 + \frac{1}{4}\lambda x^4 + \frac{1}{4}\frac{\mu^4}{\lambda}\right]\sigma_0, \tag{2.9}$$

$$H_R = \alpha_R\left[\sigma_x\left(k_y + \frac{eB}{\hbar}x\right) + i\sigma_y\frac{d}{dx}\right], \tag{2.10}$$

$$V_{imp}(x) = \mathrm{V_0 e}^{-\frac{(\mathrm{x}-\mathrm{x_1})^2}{\mathrm{d}^2}}. \tag{2.11}$$

Where ω_0 is the harmonic oscillator frequency, $\omega = \sqrt{\omega_0^2+\omega_c^2}$ is the effective oscillator frequency and $\omega_c = eB/m^*$ is the cyclotron frequency. $l_0 = \sqrt{\hbar/m^*\omega_0}$ is the characteristic length of the harmonic oscillator and $x_0 = -\frac{l_0^2\widetilde{\omega}_c\, k_y}{\widetilde{\omega}_c^2+1} - \frac{l_0\tilde{F}}{\widetilde{\omega}_c^2+1}$ is the guiding center coordinate where $\widetilde{\omega}_c = \frac{\omega_c}{\omega_0}$, $\widetilde{\omega} = \frac{\omega}{\omega_0} = \sqrt{\widetilde{\omega}_c^2+1}$ and $\tilde{F} = \frac{el_0F}{\hbar\omega_0}$.

The set of eigenfunctions of H_1 is given as:

$$\phi_{n\sigma}(x) = \frac{1}{\sqrt{l_0\sqrt{\frac{\pi}{\sqrt{\widetilde{\omega}_c^2+1}}}2^n n!}} H_n\left(\frac{x-x_0}{\frac{l_0}{\sqrt[4]{\widetilde{\omega}_c^2+1}}}\right)\times \exp\left(-\frac{1}{2}\left(\frac{x-x_0}{\frac{l_0}{\sqrt[4]{\widetilde{\omega}_c^2+1}}}\right)^2\right)\chi_\sigma \tag{2.12}$$

Where $H_n(x)$ are the Hermite polynomials of integer order n, χ_σ are spinor functions with

$\chi_+ = \binom{1}{0}$ for spin-up and $\chi_- = \binom{0}{1}$ for spin-down in the z-direction.

By using the set of eigenfunctions of H_1 the matrix elements of the whole Hamiltonian can be written as:

$$\langle \phi_{n\sigma}|H|\phi_{m\sigma'}\rangle =$$
$$\langle \phi_{n\sigma}|H_1|\phi_{m\sigma'}\rangle + \langle \phi_{n\sigma}|H_2|\phi_{m\sigma'}\rangle + \langle \phi_{n\sigma}|H_R|\phi_{m\sigma'}\rangle + \langle \phi_{n\sigma}|V_{imp}|\phi_{m\sigma'}\rangle \quad (2.13)$$

The energy eigenvalues corresponding to H_1 are:

$$\frac{E_1}{\hbar\omega_0} = \sqrt{\widetilde{\omega}_c^2+1}\left(n+\frac{1}{2}\right) + \frac{1}{2(\widetilde{\omega}_c^2+1)}(l_0^2k_y^2 - 2l_0k_y\tilde{F}\widetilde{\omega}_c - \tilde{F}^2) \pm \frac{g^*\mu_B B}{2\hbar\omega_0} \quad (2.14)$$

And the matrix elements corresponding to H_2 are:

$$\left\langle \phi_{n\sigma}\left|\frac{H_2}{\hbar\omega_0}\right|\phi_{m\sigma'}\right\rangle = A_{-4}\delta_{n,m-4} + A_{-3}\delta_{n,m-3} + A_{-2}\delta_{n,m-2} + A_{-1}\delta_{n,m-1} + A_0\delta_{n,m}$$
$$+A_{+1}\delta_{n,m+1} + A_{+2}\delta_{n,m+2} + A_{+3}\delta_{n,m+3} + A_{+4}\delta_{n,m+4}. \quad (2.15)$$

Where:

$$A_{-4} = \frac{1}{16}\frac{\tilde{\lambda}}{\widetilde{\omega}_c^2+1}\sqrt{(n+4)(n+3)(n+2)(n+1)},$$

$$A_{-3} = \frac{1}{4}\frac{x_0}{l_0\sqrt{\widetilde{\omega}_c^2+1}}\tilde{\lambda}\sqrt{\frac{2}{\sqrt{\widetilde{\omega}_c^2+1}}(n+3)(n+2)(n+1)},$$

$$A_{-2} = \frac{1}{4\sqrt{\widetilde{\omega}_c^2+1}}\sqrt{(n+2)(n+1)}\left[\tilde{\lambda}\left(3\frac{x_0^2}{l_0^2} + \frac{1}{\sqrt{\widetilde{\omega}_c^2+1}}\left(n+\frac{3}{2}\right)\right) - (1+\tilde{\mu}^2)\right],$$

$$A_{-1} = \frac{1}{2}\frac{x_0}{l_0}\sqrt{\frac{2}{\sqrt{\widetilde{\omega}_c^2+1}}(n+1)}\left[\tilde{\lambda}\left(\frac{x_0^2}{l_0^2} + \frac{3}{2\sqrt{\widetilde{\omega}_c^2+1}}(n+1)\right) - (1+\tilde{\mu}^2)\right],$$

$$A_0 = \frac{1}{4}\tilde{\lambda}\left[\frac{x_0^4}{l_0^4} + \frac{3}{\sqrt{\tilde{\omega}_c^2+1}}\frac{x_0^2}{l_0^2}(2n+1) + \frac{\tilde{\mu}^4}{\tilde{\lambda}^2}\right] + \frac{1}{4}\tilde{\lambda}\left[\frac{3}{2(\tilde{\omega}_c^2+1)}\left(n^2+n+\frac{1}{2}\right)\right] - \frac{1}{2}(1+\tilde{\mu}^2)\left[\frac{x_0^2}{l_0^2} + \frac{1}{\sqrt{\tilde{\omega}_c^2+1}}\left(n+\frac{1}{2}\right)\right],$$

$$A_{+1} = \frac{1}{2}\frac{x_0}{l_0}\sqrt{\frac{2}{\sqrt{\tilde{\omega}_c^2+1}}n}\left[\tilde{\lambda}\left(\frac{x_0^2}{l_0^2} + \frac{3}{2\sqrt{\tilde{\omega}_c^2+1}}n\right) - (1+\tilde{\mu}^2)\right],$$

$$A_{+2} = \frac{1}{4\sqrt{\tilde{\omega}_c^2+1}}\sqrt{n(n-1)}\left[\tilde{\lambda}\left(3\frac{x_0^2}{l_0^2} + \frac{1}{\sqrt{\tilde{\omega}_c^2+1}}\left(n-\frac{1}{2}\right)\right) - (1+\tilde{\mu}^2)\right],$$

$$A_{+3} = \frac{1}{4}\tilde{\lambda}\frac{x_0}{l_0\sqrt{\tilde{\omega}_c^2+1}}\sqrt{\frac{2}{\sqrt{\tilde{\omega}_c^2+1}}n(n-1)(n-2)},$$

$$A_{+4} = \frac{1}{16(\tilde{\omega}_c^2+1)}\tilde{\lambda}\sqrt{n(n-1)(n-2)(n-3)},$$

With $\tilde{\lambda} = \frac{\lambda\hbar\omega_0}{\left(m^*\omega_0^2\right)^2}$ and $\tilde{\mu} = \frac{\mu}{\sqrt{m^*}\omega_0}$.

The matrix elements of Rashba Hamiltonian H_R are given by:

$$\left\langle \phi_{n\sigma}\left|\frac{H_R}{\hbar\omega_0}\right|\phi_{m\sigma'}\right\rangle =$$

$$\sqrt{2\frac{\Delta_R}{\hbar\omega_0}}\left[l_0 k_y\left(1-\frac{\tilde{\omega}_c^2}{\tilde{\omega}_c^2+1}\right) - \frac{\tilde{\omega}_c}{\tilde{\omega}_c^2+1}\tilde{F}\right]\delta_{n,m} +$$

$$\sqrt{2\frac{\Delta_R}{\hbar\omega_0}\sqrt{\tilde{\omega}_c^2+1}}\left[\left(\frac{\tilde{\omega}_c}{\sqrt{\tilde{\omega}_c^2+1}} \pm 1\right)\sqrt{\frac{(n+1)}{2}}\delta_{n,m-1} + \left(\frac{\tilde{\omega}_c}{\sqrt{\tilde{\omega}_c^2+1}} \mp 1\right)\sqrt{\frac{n}{2}}\delta_{n,m+1}\right] \qquad (2.16)$$

Where: $\Delta_R = \frac{\alpha_R^2 m^*}{2\hbar^2}$.

The matrix elements of the Gaussian impurity Hamiltonian $V_{imp}(x)$ are:

$$\left\langle \phi_{n\sigma} \left| \frac{V_{imp}(x)}{\hbar\omega_0} \right| \phi_{m\sigma'} \right\rangle = \left\langle \phi_{n\sigma} \left| \frac{V_0}{\hbar\omega_0} e^{-\frac{(x-x_1)^2}{d^2}} \right| \phi_{m\sigma'} \right\rangle \tag{2.17}$$

With the help of the standard integral [62],

$$\int_{-\infty}^{\infty} e^{-(x-y)^2} H_m(\alpha x) H_n(\alpha x) dx = \pi^{1/2} \sum_{k=0}^{min(m,n)} 2^k k! \binom{m}{k}\binom{n}{k} (1-\alpha^2)^{\frac{m+n}{2}-k} H_{m+n-2k}\left[\frac{\alpha y}{(1-\alpha^2)^{1/2}}\right] \tag{2.18}$$

The matrix elements of $V_{imp}(x)$ can be written as:

$$\left\langle \phi_{n\sigma} \left| \frac{V_{imp}(x)}{\hbar\omega_0} \right| \phi_{m\sigma'} \right\rangle = \frac{V_0}{\sqrt{2^{n+m} n!\, m!}} \times \sqrt{\frac{\sqrt{\tilde{\omega}_c^2+1}}{(\sqrt{\tilde{\omega}_c^2+1}+\frac{1}{d^2})}} \times e^{\frac{-(x_0-x_1)^2\left(1-\left(\frac{1}{d^2}\right)\right)}{\left(\frac{\sqrt{\tilde{\omega}_c^2+1}}{(\sqrt{\tilde{\omega}_c^2+1}+\frac{1}{d^2})}\right)d^2}}$$

$$\times \sum_{k=0}^{min(m,n)} 2^k k! \binom{m}{k}\binom{n}{k} \times \left(\frac{\sqrt{\tilde{\omega}_c^2+1}}{\left(\sqrt{\tilde{\omega}_c^2+1}+\frac{1}{d^2}\right)}\right)^{\frac{m+n}{2}-k} H_{m+n-2k}\left[\frac{\frac{-(x_0-x_1)}{d^2}\sqrt{\tilde{\omega}_c^2+1}/(\sqrt{\tilde{\omega}_c^2+1}+\frac{1}{d^2})}{\sqrt{\left(1-\sqrt{\tilde{\omega}_c^2+1}\right)/\sqrt{\tilde{\omega}_c^2+1}+\frac{1}{d^2}}}\right]. \tag{2.19}$$

2.3 Electronic, magnetic and thermal properties of the DQW

From the numerical outputs (the energy spectra), it becomes possible to calculate the partition function using canonical definition :

$$Z = \sum_{n}^{\infty} e^{-\beta E_n} \tag{2.20}$$

Where $= 1/k_B T$, k_B is a Boltzmann constant.

The entropy (S) can be achieved by the following formula [37]:

$$S = \frac{\partial}{\partial T}(K_B T LnZ) \tag{2.21}$$

For the isothermal process, the quantity ΔS is given by [97]:

$$\Delta S_{iso} = S\,(B) - S(B = 0) \tag{2.22}$$

Which is used to characterize the magnetocaloric properties of the system.

The electronic density of state (DOS) is another physical quantity that can give important information about the electronic structure of the nanomaterial, which is given as the sum of a series of δ functions as,

$$DOS(E) = \sum_{n=1}^{N} \delta(E - E_n) \tag{2.23}$$

The delta function which appears in the DOS can be replaced by a more practical expression in the computational process [98],

$$DOS(E) = \frac{1}{\sqrt{2\pi\Gamma^2}} \sum_n e^{-\frac{(E-E_n)^2}{2\Gamma^2}} \tag{2.24}$$

where Γ is the broadening factor and E_n is the energy value for the nth eigenstate

The local density of states which can give information about the tunneling current and the tunneling conductance in the STM spectroscopy.

$$LDOS(r, E) = \sum_{n=1}^{N} |\psi_n|^2 \delta(E - E_{\mathrm{n}}) \tag{2.25}$$

The magnetization (M) of the double quantum wire serves as an indicator of the system's magnetic response to external magnetic field. Defined as the derivative of the system-averaged energy $\langle E \rangle$ with respect to the applied magnetic field B,

$$M = -\frac{\partial \langle E \rangle}{\partial B} \tag{2.26}$$

where the average energy can be calculated by using the standard statistical expression:

$$\langle E \rangle = -\frac{\partial\, Ln(Z)}{\partial \beta} \tag{2.27}$$

The magnetic susceptibility (χ) classifies a material as diamagnetic when ($\chi < 0$) and paramagnetic when ($\chi > 0$). The material's magnetic susceptibility can be obtained by computing the derivative of magnetization (M) with respect to the magnetic field.

$$\chi = \frac{\partial \mathrm{M}}{\partial \mathrm{B}} \tag{2.28}$$

It is important to note that obtaining the exact derivative in an analytical form is not possible, as the diagonalization process provides only numerical values for the energy spectrum. Consequently, the derivative is evaluated using its fundamental definition. For instance, the magnetization can be determined using the following finite difference approximation:

$$M = \lim_{\Delta B \to 0} \frac{\langle E(B + \Delta B)\rangle - \langle E(B)\rangle}{\Delta B} \tag{2.29}$$

Similarly, magnetic susceptibility can be computed following the same approach,

$$\chi = \lim_{\Delta B \to 0} \frac{M(B + \Delta B) - \ M(B)}{\Delta B} \tag{2.30}$$

2.4 Energy spectra computation by exact diagonalization method

The wavefunctions, which form the basis of the one-dimensional harmonic oscillator, form a complete set. This means that any function can be represented as a linear combination of these basis.

In quantum systems, the exact energy spectrum can only be obtained by constructing a Hamiltonian matrix with an infinite number of dimensions. This is because an infinite basis set is required to fully describe all possible quantum states. However, in practical calculations, working with an infinitely large matrix is impossible. Instead, we must choose a finite basis size that is sufficiently large to ensure accurate results. Since the dimension of the Hamiltonian matrix is determined by the number of basis states included, selecting an appropriate basis is critical for achieving reliable numerical solutions.

As the number of basis states (N), increases, the representation of the system improves, and the results become more accurate. However, beyond a certain point, further increasing N does not significantly change the computed low-lying excited states, as they have already reached their true values within a given accuracy. This means that for a sufficiently large N, the calculated energy levels become stable, and additional basis states only introduce negligible corrections.

To ensure accuracy, we choose N such that the highest energy level of interest, labeled as E_f, approaches a fixed value as N increases. Mathematically, this condition of convergence can be expressed as,

$$\left|E_f(\,N+1\,) - E_f(N)\right| = \delta_1 < \epsilon_1 \tag{2.31}$$

Where, ϵ_1 represents the maximum acceptable tolerance for the energy value, which is determined by the required accuracy of the calculation. This tolerance ensures that the computed energy values do not change significantly when increasing the basis size from N to $N+1$. In other words, ϵ_1 controls the difference between the energy values obtained for two successive basis sizes, ensuring that the results have reached a stable and convergent form.

The method used to obtain these energy values is known as exact diagonalization. This numerical approach involves constructing the Hamiltonian matrix in a chosen basis and solving for its eigenvalues and eigenvectors.

The eigenvalues correspond to the possible energy levels of the system, while the eigenvectors represent the associated quantum states. Since the Hamiltonian matrix has a finite dimension in practical calculations, the accuracy of the computed energy levels depends on how large the chosen basis is.

By selecting an appropreate tolerance ϵ_1, we can systimatically check whether increasing N further has a noticeable effect on the results. If the difference in the computed energy values between N and $N+1$ is smaller than ϵ_1, we consider the solution to have converged. This ensures that the numerical results are reliable without the need for unnecessary computational effort. Thus, exact diagonalization provides highly accurate solutions within the limits of a chosen.

Chapter Three

Results and Discussions

This chapter presents a detailed analysis of the physical properties of a double quantum wire (DQW) system composed of $InSb$. The investigation is based on the Hamiltonian that describes the system.

This chapter is divided into three main sections. The first section discusses the electronic properties of the DQW, including energy dispersion and the effects of external fields. The second section explores the magnetic properties, focusing on magnetization and magnetic susceptibility. The third section examines the magnetocaloric effect (MCE), analyzing its behavior under varying magnetic fields and other parameters.

3.1 Electronic Properties of Double Quantum Wire Systems

In this section, we examine the probability density, energy spectrum, the local density of states, and the role of external influences such as electric and magnetic fields. The confinement potential and SOC significantly affect the sub-band structure and energy dispersion. Additionally, the presence of impurities modifies the local density of states. Understanding these electronic properties provides a foundation for analyzing the system's magnetic and thermal behavior in subsequent sections.

The changes in the confinement potential shape, influenced by structural parameters and varying across the x-coordinates, are illustrated in Figure1, while keeping the parameter λ constant. In Figure1.a, it is evident that when $\mu = 0$, the confinement exhibits a SQW (single quantum wire) structure. However, for $\mu \neq 0$, the potential confines the carriers within two narrower wires, resulting in a DQW (double quantum wire) confinement. To investigate the influence of the adjustable parameter μ, the confinement potential has been graphically represented for various μ values in figure1.b. As μ increases, the barrier between the two wires becomes higher. Consequently, the probability of carriers tunneling from one wire to the other decreases. Therefore, the increase in μ acts as a controlling factor, influencing the confinement potential and, in turn, limiting the probability of quantum tunneling events between the two distinct wires.

Figure 1

Confinement potential profile versus the growth direction coordinate a) SQW and DQW profiles. b) DQW profile for different μ values at fixed λ value ($\lambda = 3 * 10^{-4}\ meV/nm^4$).

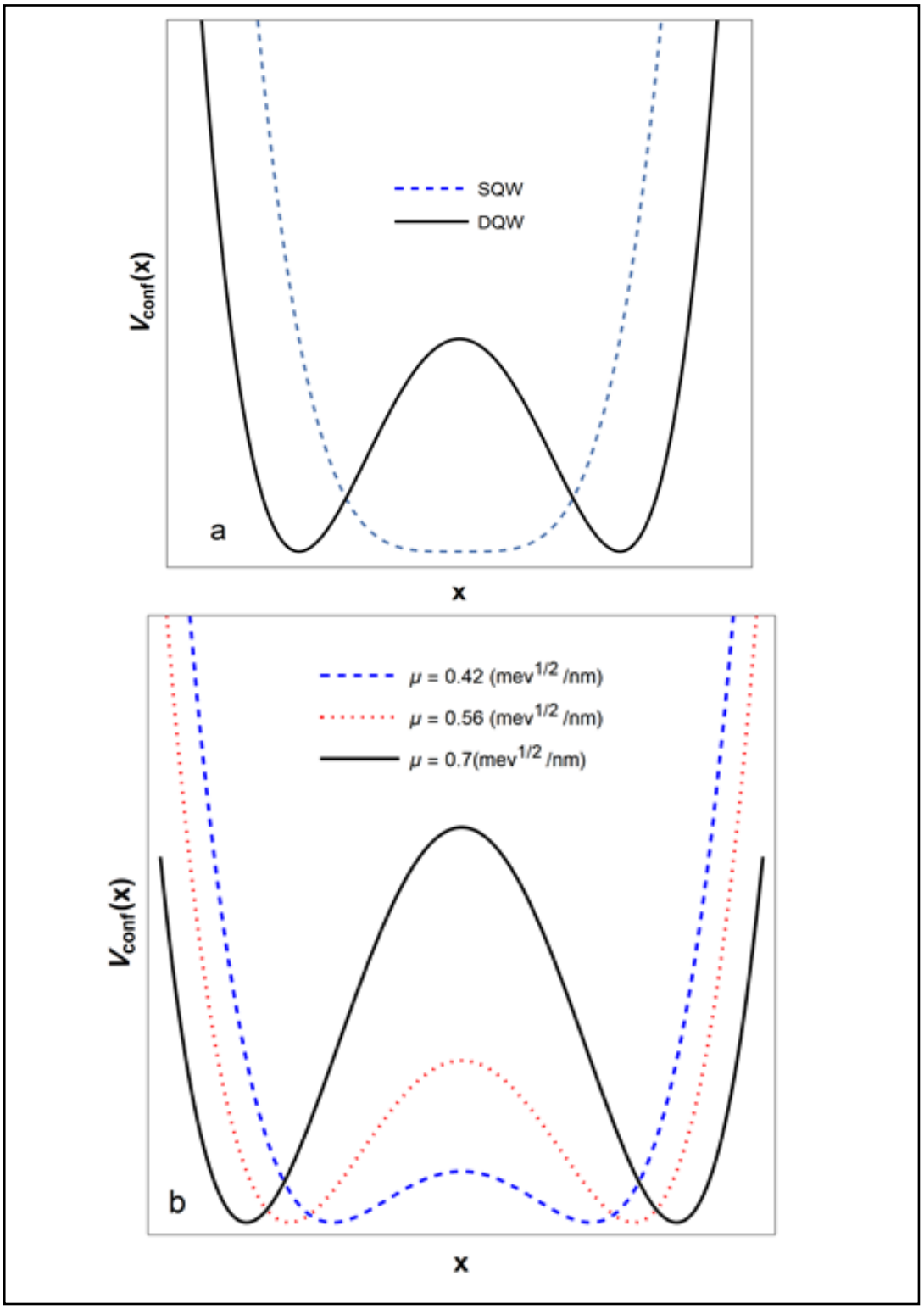

Figure 2

The confinement potential and square wave functions corresponding to the first few energy levels a) for SQW and b) DQW at $\mu = 0.56\ meV^{\frac{1}{2}}/nm$ *and* $\lambda = 3 * 10^{-4}\ meV/nm^4$ *c) DQW at* $\mu = 0.7\ meV^{\frac{1}{2}}/nm$ *and* $\lambda = 3 * 10^{-4}\ meV/nm^4$.

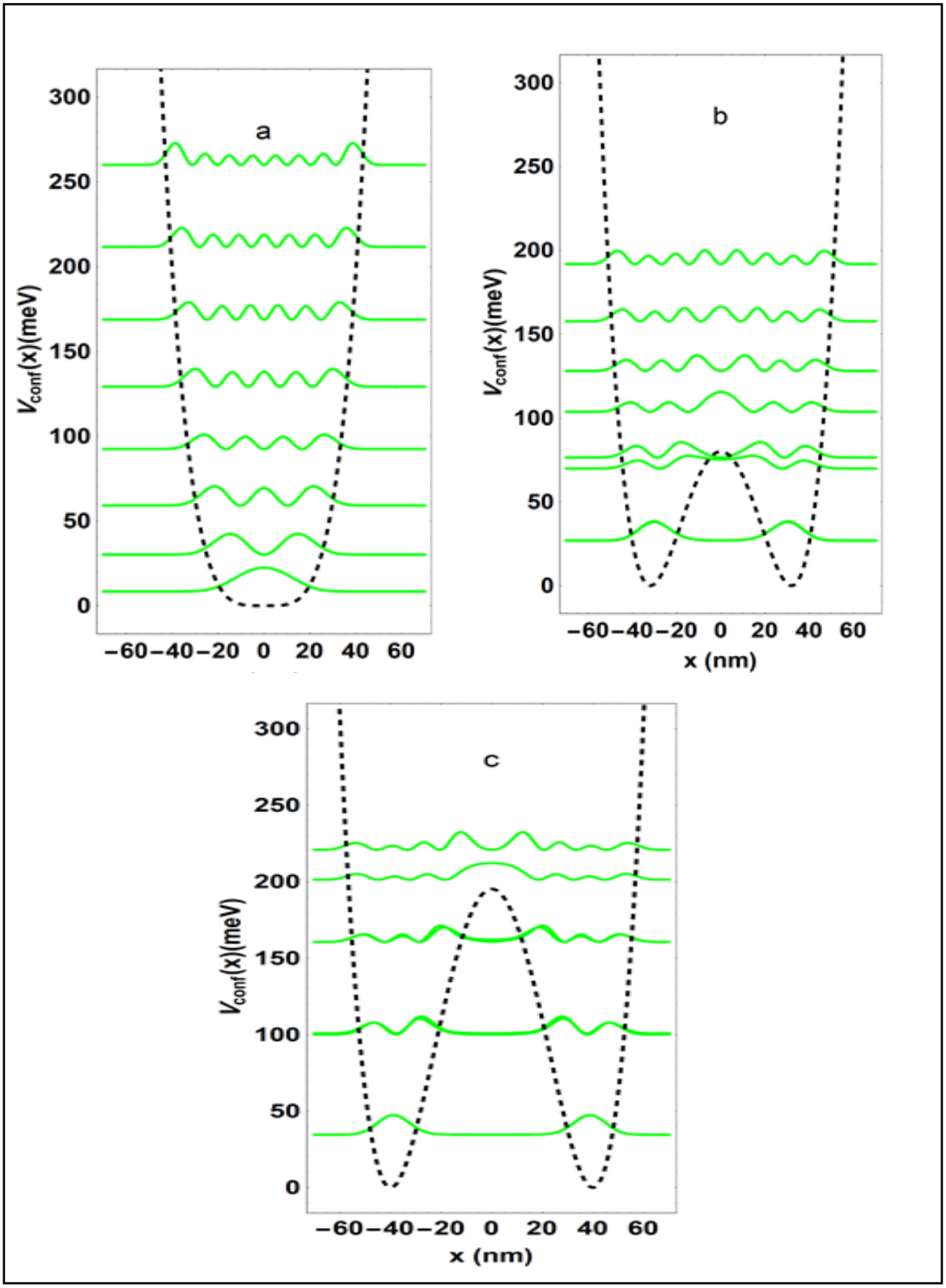

In Figure2, the influence of the adjustable parameter μ on probability density is apparent. When μ is set to zero, as illustrated in Figure2.a, leads to the formation of a single quantum wire (SQW) shape, Figure2.a presents a clear representation of the probability density distribution for the first few energy levels. However, in Figures2.b ($\mu = 0.56\ meV^{\frac{1}{2}}/nm$) and 2.c ($\mu = 0.7\ meV^{\frac{1}{2}}/nm$) (the values of μ and λ were chosen to be within the experimental range of the double quantum wire (DQW)), the introduction of a barrier results in a double quantum wires (DQW) configuration, causing a noticeable change in the distribution of the probability density. The effect of the barrier on the probability density is evident, as it decreases the probability density in its location of effect, especially for states with initially higher probability density at the barrier position. The redistributed probability density is equally distributed in two wires, and the energy value for each state increases, and this increase is greater for the levels that had a higher probability at the location of the barrier's effect. For example, the barrier's impact on the first level is greater than its impact on the second level because the wave function for the first level has an antinode at the barrier's location. Consequently, the barrier divides the probability into two equal parts in each wire, and the energy increase for this level is significant. As for the second level, which originally had a node in its wave function in the barrier's location, resulted in a smaller energy increase compared to the first level. Therefore, the first and second levels become degenerate within each wire. Furthermore, as μ increases, the barrier height also increases, affecting higher energy states. Therefore, μ causes a degenerate state in each wire and also causes symmetry degeneracy in probability density across the two wires, as it is clear from the comparison between Figures2.a and 2.b. The symmetry degeneracy becomes more pronounced at higher energy levels as the value of μ increases, as illustrated in Figure2.c.

Figure 3, provides insight into the effect of the impurity potential on the probability density within a double quantum wire system. The impurity was placed in the center of one of the wires ($x_1 = 19\ nm$) as shown in Figure3.b, the impurity significantly influenced the probability density of the energy levels.

Figure 3

The confinement potential and square wave functions corresponding to the first few energy levels a) DQW at $\mu = 0.7\ meV^{\frac{1}{2}}/nm$ *and* $\lambda =$

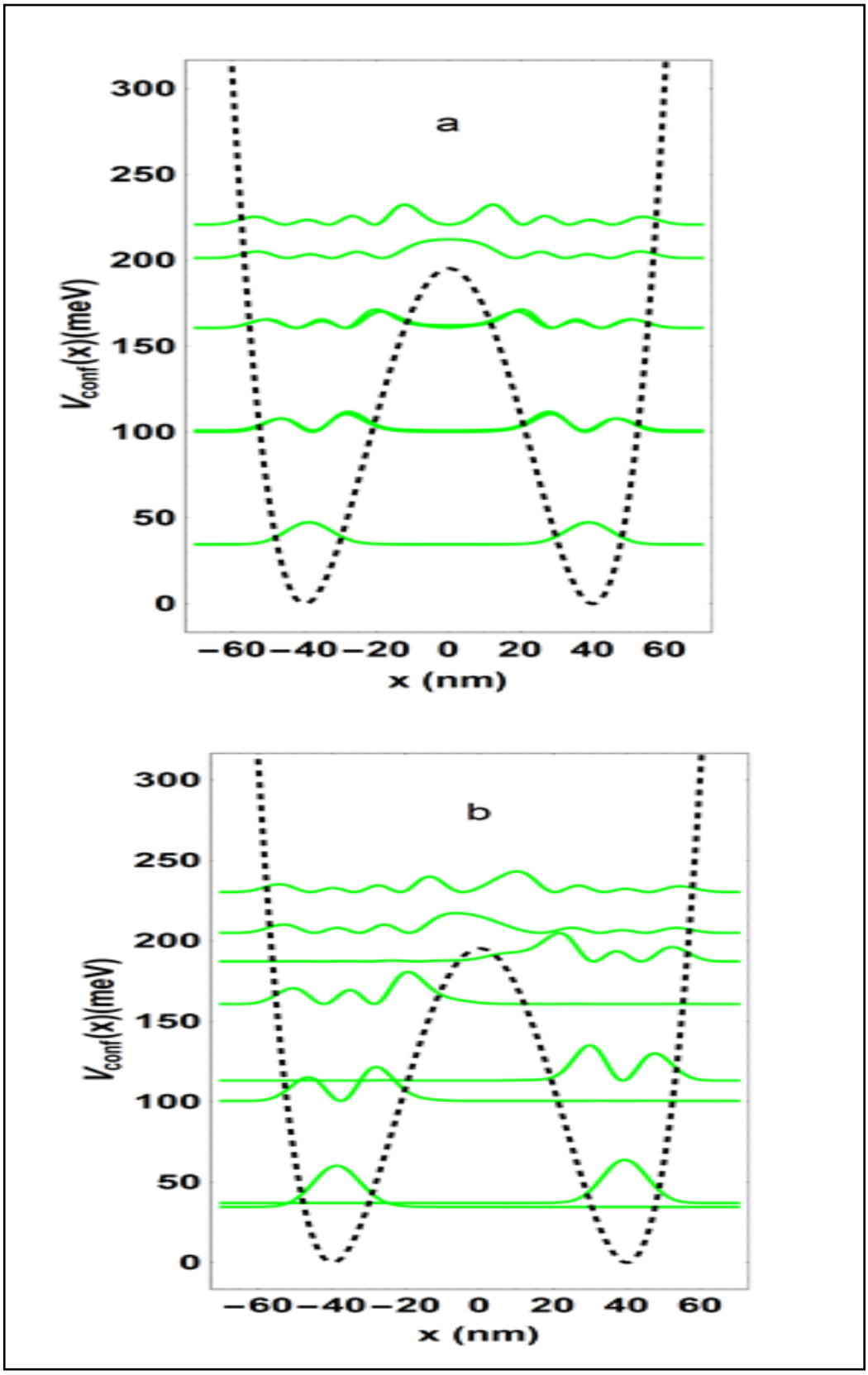

$3 * 10^{-4}\ meV/nm^4$ without vaiation, b) DQW at $\mu = 0.7\ meV^{\frac{1}{2}}/nm$ and $\lambda = 3 * 10^{-4} meV/nm^4$, $V_0 = 60\ meV$, $x_1 = 19\ nm$ and $d = 8\ nm$.

A comparative analysis between Figure3.a, and Figure3.b, reveals a significant change in the probability density due to the impurity potential, which results in an elevation of the energy levels within the wire where it is situated. This effect leads to redistribution of the probability density, resulting in the elimination of the symmetry degeneracy which is clearly evident in the Figure3 a.

From the comparison, it becomes evident that the probability density has made a marked redistribution. For example, the first peak in the left wire now corresponds to the ground energy level, while the first peak in the right wire, represents the first exited energy level. So the energy levels have been extensively redistributed, and the symmetry degeneracy has been removed.

The influence of the parameter μ on merging energy levels is distinctly evident in Figure4.a. It is apparent that at higher values of μ, the merging is exhibiting at higher energy levels. Additionally, the energy levels associated with the system have a degeneracy related to the spin of the electron, where each line in the figure represents two degenerate energy levels due to the spin of the electron.

The external magnetic field has a significant effect, as shown in Figure4.b, the external magnetic field plays a dual role by removing the spin degeneracy and causing the separation of energy levels that were previously merged due to the confinement potential in each wire.

This leads to a noticeable change in the levels of the energy and provides a clear illustration of the magnetic field's influence on the quantum characteristics of the system. The external magnetic field results in a shift up in the energy levels of the system. This shift is dependent on the magnetic field strength, and each energy level in the system will split into two sublevels due to the interaction with the external magnetic field this leads to the remove of the degeneracy in the energy levels.

Figure 4

The energy dispersion versus μ a) at $B = 0$ *b) at* $B = 0.2\,T$ *, at* $\lambda = 3 * 10^{-4}\ meV/nm^4$.

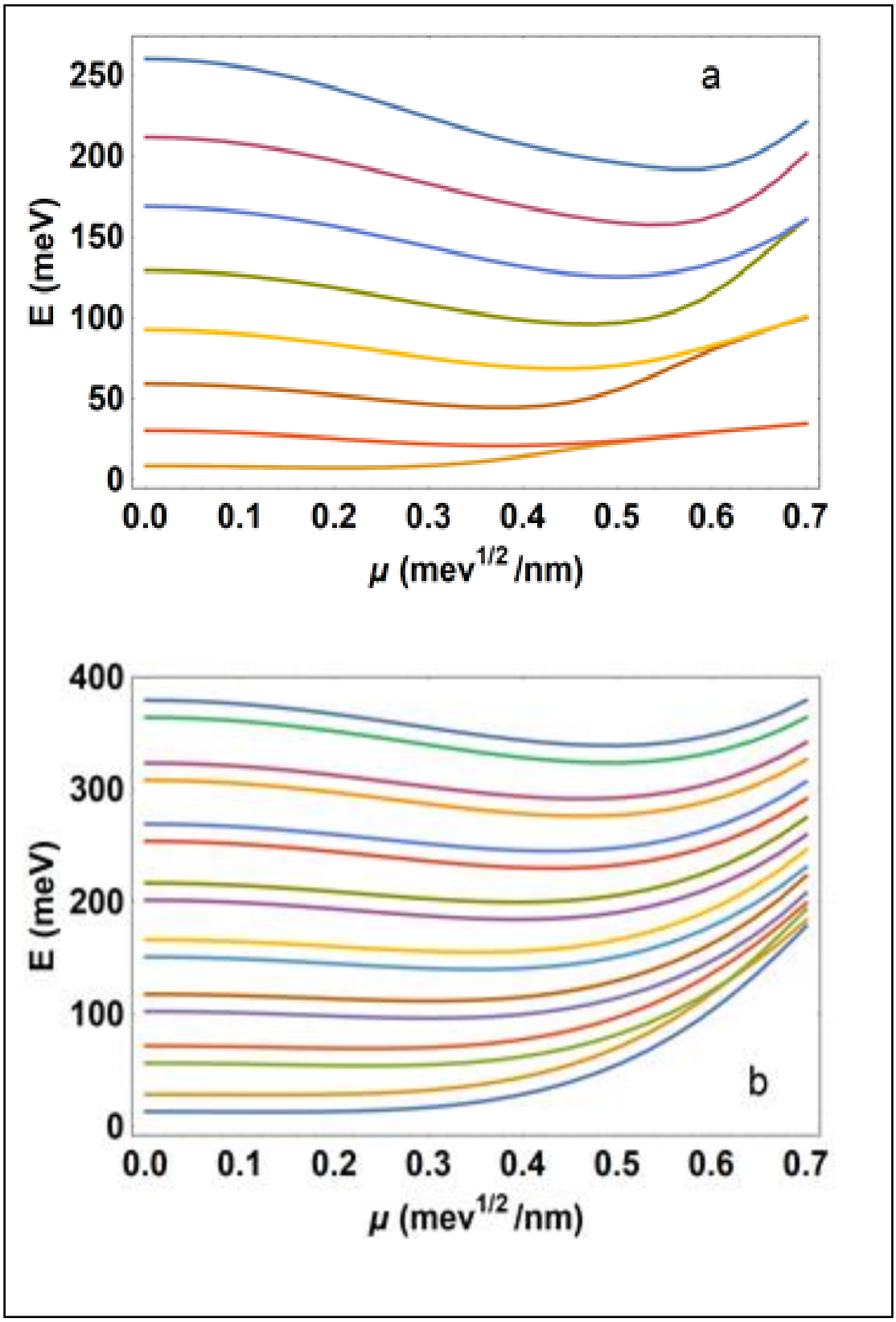

Figure 5

The energy dispersion at $k_y = 0$ *as a function of B for* $\mu = 0.7\ meV^{\frac{1}{2}}/nm$, $\lambda = 3 * 10^{-4}\ meV/nm^4$. *a)* $\alpha_R = 0$ *b)* $\alpha_R = 100$ *meV.nm.*

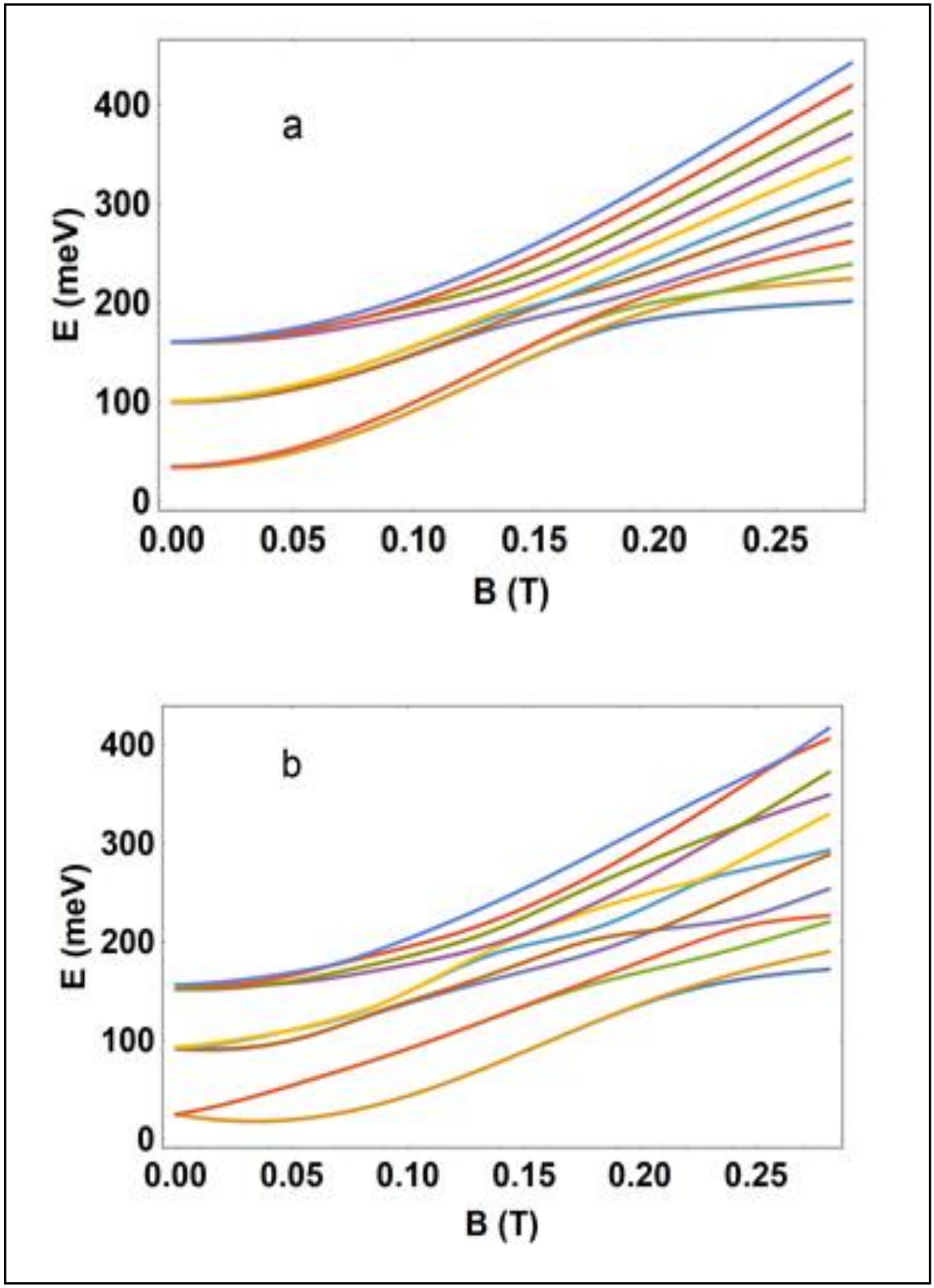

In conclusion, the external magnetic field has an essential effect on the double quantum wire system, causing the splitting of energy levels and giving rise to changes in the electronic structure. The ability to adjust the strength of the external magnetic field provides a technique to organize energy levels and control the electronic properties of the double quantum wire system.

For a more focused analysis of the magnetic field and Rashba spin-orbit coupling effect on the DQW system, Figure5 has been introduced. Figure5.a. illustrates the effect of the magnetic field on certain energy levels within the system. It is observed in the figure that the energy levels are merged due to the influence of the barrier potential created by the confinement potential. Lower energy levels experience a more significant impact from the barrier since they are situated where its effect is stronger. In the higher energy levels, the influence of the barrier diminishes. Thus, in lower energy levels where the influence of the barrier is significant, the magnetic field needs more strength to separate the merged energy levels, while higher energy levels require a smaller magnetic field strength.

As illustrated in the figure, the magnetic field eliminates the spin degeneracy and separates the merged energy levels, raising the energy for all levels. This emphasizes the role of the magnetic field in redistributing and controlling the energy levels, thereby influencing and controlling the physical properties of the DQW system.

The interaction between the magnetic field and Rashba spin-orbit coupling plays a critical role in creating a significant separation in spin-up and spin-down branches of the energy levels. When higher magnetic field values are applied, the behavior of the energy spectrum becomes complicated compared to the case where no Rashba spin-orbit coupling is present.

The interaction between the magnetic field and the Rashba spin-orbit coupling results in anti-crossings between the various sub-bands of energy states, leading to a more complex and rich structure in the overall energy spectrum of the system. These anti-crossings represent points where the energy levels of different spin states intersect, providing a unique insight into the dynamics of the system under the influence of both magnetic field and Rashba spin-orbit coupling as demonstrated in Figure5.b.

Figure 6

The energy dispersion at $k_y = 0$ *versus* x_1 *for* $(V_0 = 100\,meV, d = 8\,nm)$. *a)* $\mu = 0\,,\ \lambda = 3 * 10^{-4}\frac{meV}{nm^4}.,B = 0.$ *b)* $\mu = 0\,,\ \lambda = 3 * 10^{-4}\frac{meV}{nm^4}, B = 0.05T.$ *c)* $\mu = 0.7\frac{meV^{\frac{1}{2}}}{nm},\ \lambda = 3 * 10^{-4}\frac{meV}{nm^4}, B = 0$ *d)* $\mu = 0.7\frac{meV^{\frac{1}{2}}}{nm},\ \lambda = 3 * 10^{-4}\frac{meV}{nm^4}, B = 0.05T.$

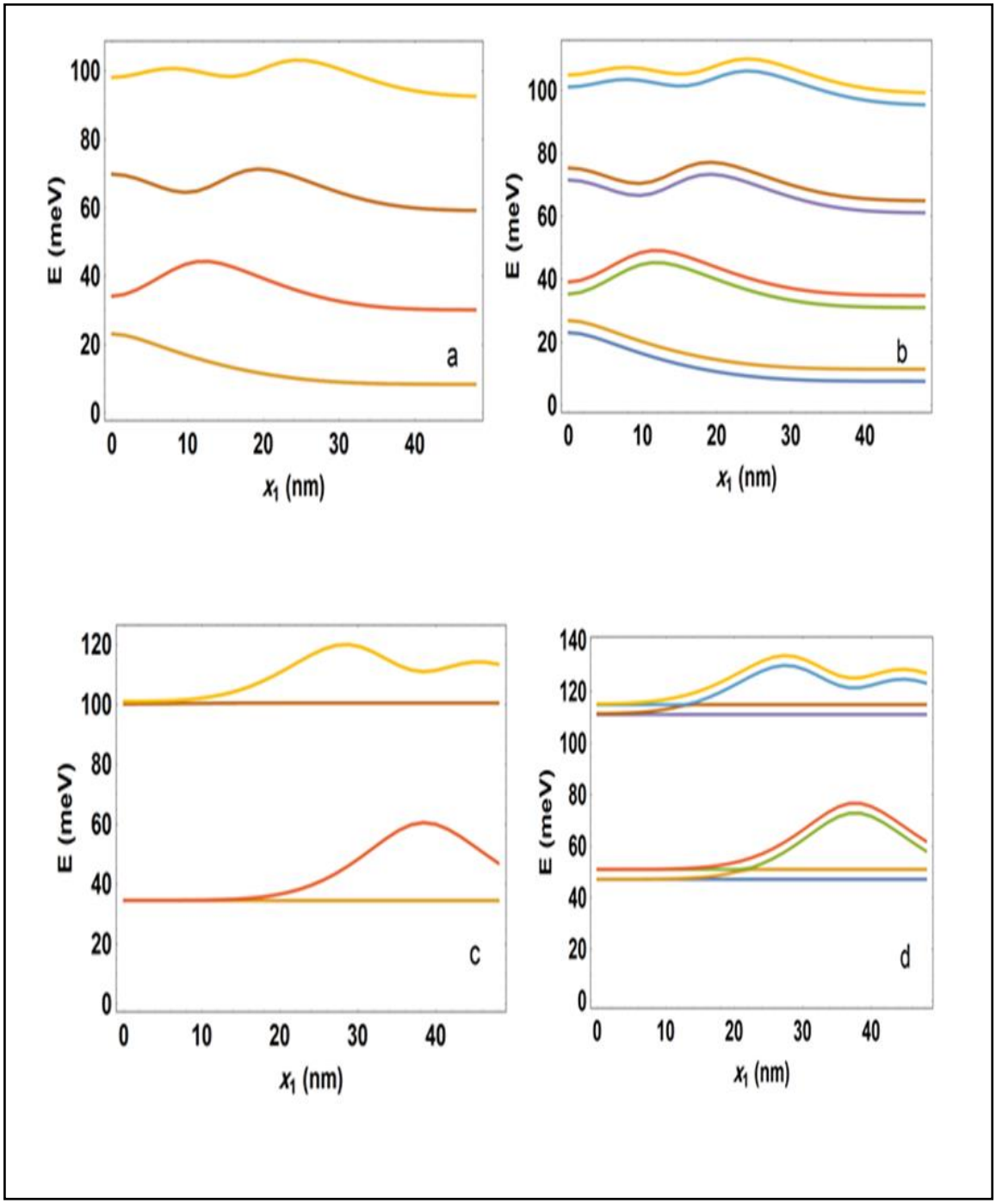

Figure 6, illustrates the effect of the impurity position and strength, as well as the external magnetic field on the energy levels in two cases: when $\mu = 0$ (no barrier) SQW and when $\mu = 0.7\frac{meV^{\frac{1}{2}}}{nm}$ (barrier) DQW. Through a detailed examination of figure6 (a and b) which represents the first case, the effect of the impurity on the energy levels at each position in the SQW system becomes evident. This effect will occur at the positions where there is a probability density of the energy level. Consequently, the extra potential will raise the energy levels in these positions. This also clarifies the probability density distribution in this case which we have previously discussed in Figure2. The magnetic field eliminates the spin degeneracy it separates the spin-up and spin-down branches of the energy levels. In Figure6 (c and d), the effect of the impurity 's position and the external magnetic field for the second case ($\mu = 0.7\frac{meV^{\frac{1}{2}}}{nm}$) is explained. Initially, the presence of the barrier re-distributes the energy levels, resulting in the merging of the first level with the second and the third level with the fourth. This phenomenon was previously illustrated in the second figure. Consequently, each spectral line corresponding to the energy levels represents a combination of four distinct levels: two merged due to the barrier and two due to spin degeneracy. The introduction of asymmetric impurity separates the merged levels caused by the barrier. Additionally, the application of an external magnetic field breaks the degeneracy associated with the spins.

Figure 7

The energy dispersion at $k_y = 0$ *as a function of* F *for* $\mu = 0.42 \frac{meV^{\frac{1}{2}}}{nm}$, $\lambda = 3 * 10^{-4} \frac{meV}{nm^4}$. *a)* $\alpha_R = 0,\ B = 0$. *b)* $\alpha_R = 0, B = 0.05\ T$. *c)* $\alpha_R = 100\ meV.nm, B = 0.05\ T$

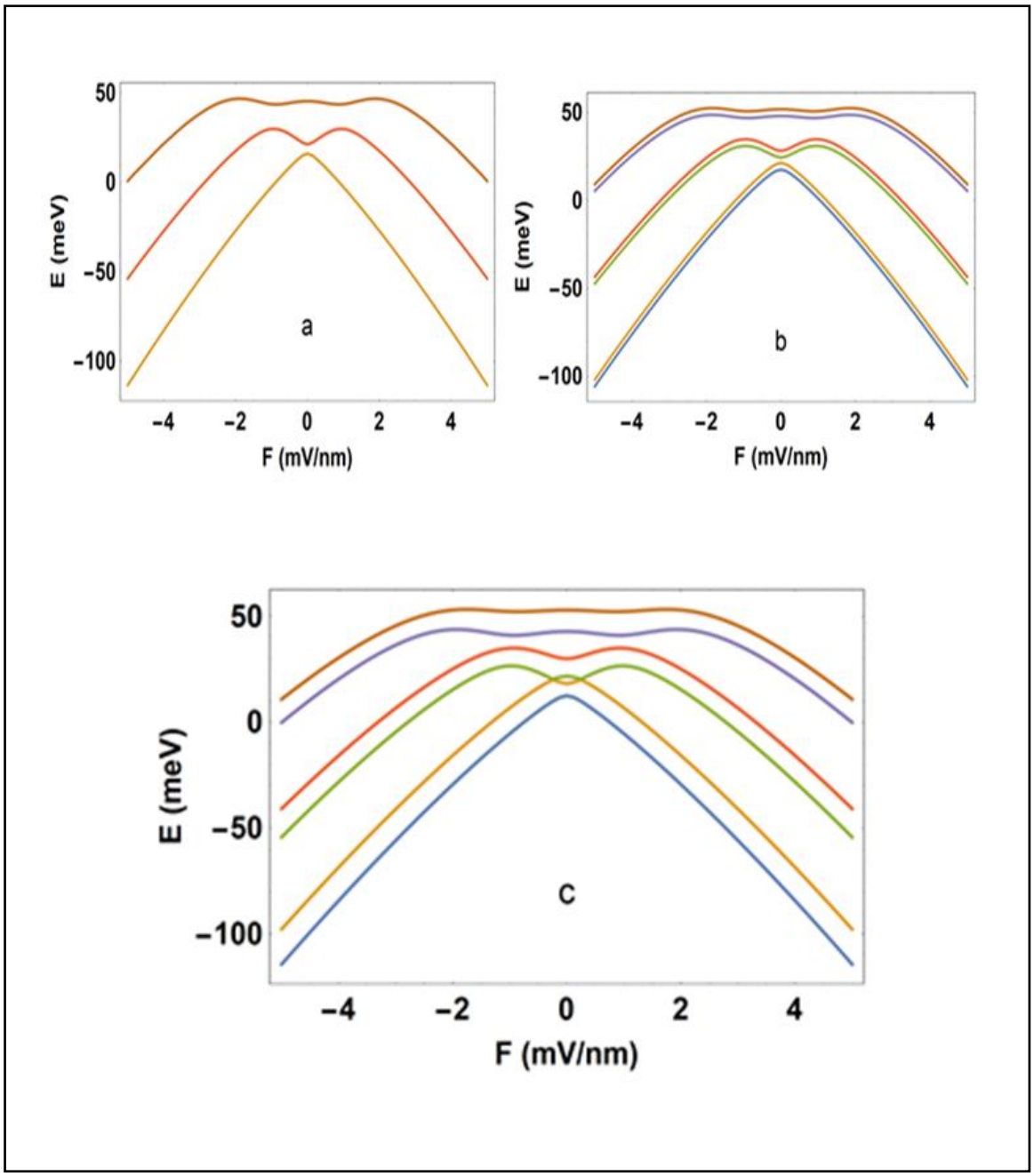

Figure 7, presents the energy of the system as a function of the applied electric field. In part a, the electric field causes a shift in the energy levels. This shift is typically due to the electrostatic potential introduced by the external electric field, the energy levels are spin-degenerate there is no spin splitting due to the absence of magnetic field and Rashba spin-orbit coupling means there's no splitting of energy levels based on spin. The energy levels for spin-up and spin-down states are degenerate.

In part b the magnetic field causes a spin splitting in the energy levels. The spin-up and spin-down energy levels separated by a constant amount due to the magnetic field, the electric field causes a uniform shift in the energy levels, the electric field affects both spin-up and spin-down states equally. In conclusion the energy levels will shift down as the magnitude of the electric field increases, while the separation between spin-up and spin-down states remains fixed by the magnetic field.

In part c both the Rashba spin-orbit coupling and magnetic field are present. Rashba spin-orbit coupling arises when there is a gradient in the potential, which can arise from structural asymmetry (such as different materials) or external electric fields. which couples the electron's spin to its momentum, the energy spectrum becomes spin-dependent, meaning that spin-up and spin-down states will no longer be degenerate. Instead, their energies will be split depending on the Rashba spin-orbit coupling.

The electric field can modulate the Rashba effect. This means that the strength of the spin-orbit coupling can change with the electric field, resulting in a variation in the energy splitting between spin-up and spin-down states. In general the increase in electric field strength leads to a stronger Rashba spin-orbit coupling, and therefore the energy splitting between the spin-up and spin-down bands becomes larger, so the spin-split bands becoming more pronounced as the electric field increases.

The magnetic field will cause additional splitting, in other words we have two types of splitting Rashba spin-orbit splitting and Zeeman splitting, this combined effect means that the spin-up and spin-down energy levels will no longer just be split by the Rashba, but also by the magnetic field. The total energy shift for each spin state will be the sum of these two effects.

Figure 8

local density of states at $x = 0$ *for* $B = 0$, *dashed lines for* $\mu = 0$, $\lambda = 3 * 10^{-4}\, meV/nm^4$, *solid lines for* $\mu = 0.7 \frac{meV^{\frac{1}{2}}}{nm}$, $\lambda = 3 * 10^{-4} \frac{meV}{nm^4}$.

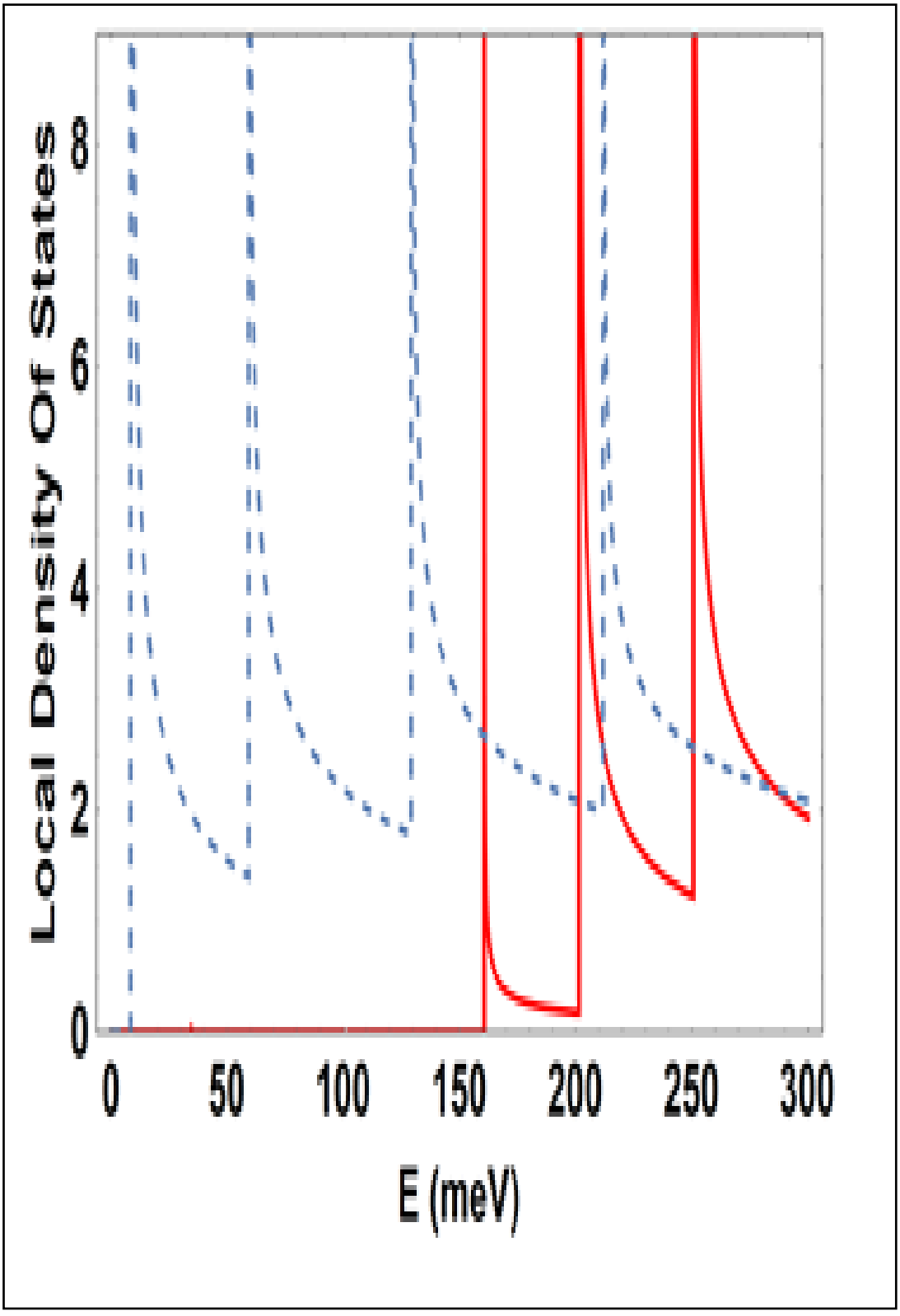

In figure8, the local density of states has been plotted at ($x = 0$) as a function of energy for ($\mu = 0$) dashed line and for ($\mu = 0.7 \frac{meV^{\frac{1}{2}}}{nm}$) solid line at a fixed value of λ ($\lambda = 3 * 10^{-4} \frac{meV}{nm^4}$). The vertical lines in the LDOS figure reflect the quantized nature of the energy levels and the presence of localized quantum states, and it gives an idea about the spatial distribution of electronic wavefunctions in the confined system. These features offer valuable insights into the electronic properties of the quantum system.

The vertical dashed lines in figure8 result from specific energy levels at ($x = 0$) position for a single quantum wire ($\mu = 0$), these lines represent energy levels with probability density at the center of the wire. This is evident when referring back to Figure2, where these vertical dashed lines in the figure correspond to the odd-numbered energy levels, such as the first and the third levels. These levels exhibit peaks in probability density at the center of the wire.

The solid line represents the local density of states at ($x = 0$) position for a double quantum wire separated by a barrier ($\mu = 0.7 \frac{meV^{\frac{1}{2}}}{nm}$) (see figure2). The presence of the barrier rearranges the probability density distribution as shown in Figure2. It is clear that the lowest energy levels, are significantly affected by the barrier and they lose the probability density at ($x = 0$) position compared with($\mu = 0$) case. Consequently, the local density of states at ($x = 0$) position will not have vertical lines for these lower energy levels. On the other hand, higher energy levels that are not significantly affected by the barrier exhibit vertical lines in the local density of states at ($x = 0$) position. These lines represent levels that have a probability density at this position, as they are not affected by the presence of the barrier potential.

Figure9, illustrates the effect of an external magnetic field and Rashba spin-orbit coupling on the local density of states, where the figure displays the local density of states as a function of energy at ($x = 27\ nm$) for a double quantum wire.

Figure9.a shows the local density of states in the absence of an external magnetic field. The first three vertical lines, each of them actually consists of four identical lines, meaning four degenerate energy levels, two because of the spin degenerate states and two due to the barrier. As for the remaining lines after the first three, each one

represents two degenerate energy levels due to the spin because the barrier's effect vanished and did not work to merge the energy levels.

Figure 9

local density of states at $x = 27\ nm,\ \mu = 0.7\frac{meV^{\frac{1}{2}}}{nm},\ \lambda = 3 * 10^{-4}\frac{meV}{nm^4}$

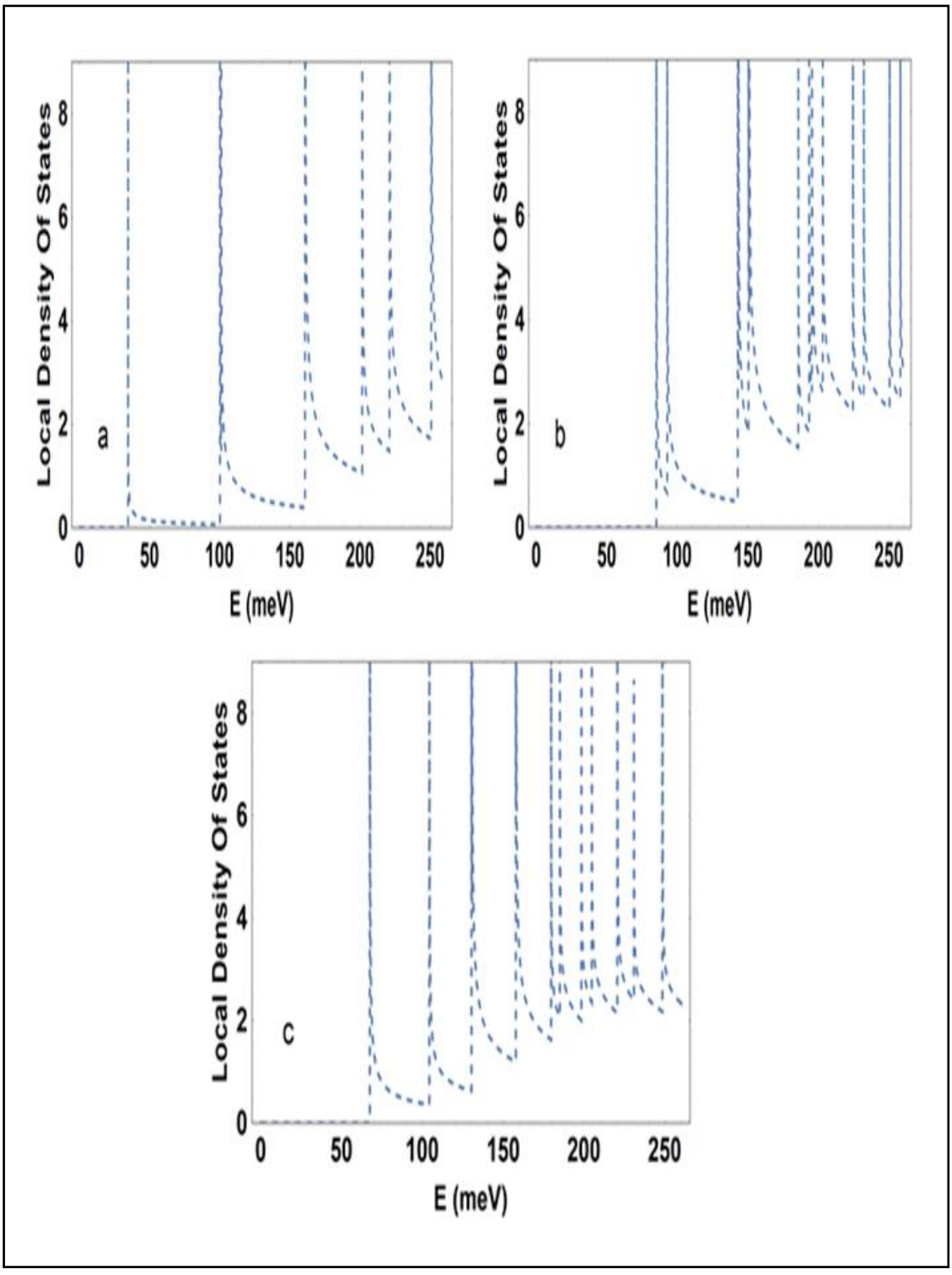

Figure 9.a for $B = 0$ and $\alpha_R = 0$ b) for $B = 0.1\,T$ and $\alpha_R = 0$. C) for $B = 0.1\,T$ and $\alpha_R = 100\,meV.nm$.

Figure 9.b, illustrates the local density of states under the presence of an external magnetic field ($B = 0.1\,T$). The effect of the external magnetic field becomes evident from this figure as it works to shift up energy levels, removes the spin degeneracy for all energy levels, and separates the merged energy levels caused by the barrier potential if they become higher than the barrier potential effective range. By raising the energy levels, the magnetic field effectively separates previously merged states that are pushed up higher than the barrier potential effective range. Consequently, states previously merged due to the barrier potential separate once more as evidenced by the four converging vertical lines in figure 9.b. The four converging vertical lines in the figure represent a single energy level before the magnetic field's influence, with the presence of the magnetic field, it separated into two levels, which were initially merged due to the barrier potential, and each level of these two levels split into two due to the removal of the spin degeneracy. The higher energy levels, which were not originally affected by the barrier potential, separate into two distinct levels upon the removal of spin degeneracy. The lower energy levels, such as the ground state, persist in their merged state due to the external magnetic field's insufficient strength to push it beyond the influence of the barrier potential, and the magnetic field only removed the spin degeneracy and separated it into two distinct levels. Rashba spin-orbit coupling generates a significant separation in spin-up and spin-down states in the energy spectra levels. This is clearly evident when comparing Figure3.b, where ($B = 0.1\,T$) and ($\alpha_R = 0$), with figure 9.c, where ($B = 0.1\,T$) and ($\alpha_R = 100\,meV.nm$), it is now evident how the Rashba spin-orbit coupling increases the separation between the spin-up and spin-down states.

Figure10, illustrates the Local Density of States ($LDOS$) as a function of energy for the double quantum wire. Figure10.a shows the $LDOS$ at the position($x = 20\,nm$), corresponding to parameters, $\mu = 0.7\frac{meV^{\frac{1}{2}}}{nm}$, $\lambda = 3 * 10^{-4}\frac{meV}{nm^4}$ and in the absence of impurity potential. Likewise, Figure 10.b exhibits the $LDOS$ at position ($x = -20\,nm$), maintaining the same parameter settings.

A notable observation lies in the remarkable symmetry between the $LDOS$ profiles presented in figure10.a and figure10.b.

Figure 10

local density of states for $\mu = 0.7\frac{meV^{\frac{1}{2}}}{nm}$, $\lambda = 3 * 10^{-4}\frac{meV}{nm^4}, B = 0$. *a) For* $x = 20\,nm$, *without impurity. b)For* $x = -20\,nm$, *without impurity. c) Dashed lines for* $x = 20\,nm$, $V_0 = 60\,meV$, $x_1 = 18\,nm, d = 8\,nm$. *solid lines for* $x = -20\,nm, V_0 = 60\,meV$, $x_1 = 18\,nm, d = 8\,nm$

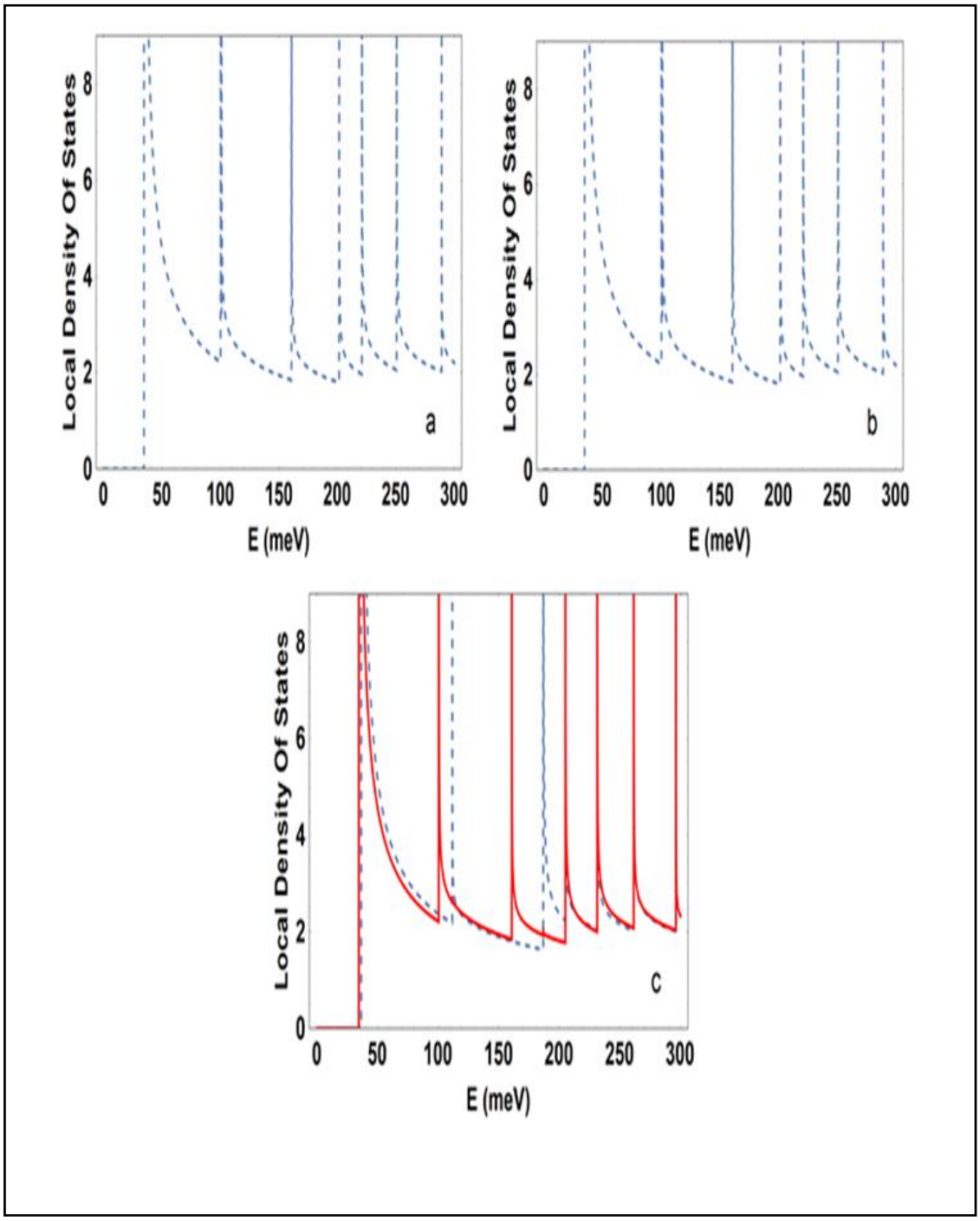

A closer examination in Figure10.c which represents the $LODS$ for the same parameter settings in Figure10.a and Figure10.b but in the presence of impurity potential ($V_0 = 60\,meV,\ x_1 = 18\,nm, d = 8\,nm.$) where the dashed line represents the LDOS plotted at the position ($x = 20\,nm$) and the solid line represents the $LDOS$ plotted at the position ($x = -20\,nm$), it becomes evident how the impurity effect the energy spectra. The introduction of the impurity potential brings a noticeable increase in the energy levels near its position. This observation implies that the adding impurity exerts a significant influence on the local electronic structure, resulting in changes to the energy levels within the quantum wire system. This observation aligns with the results discussed in figure3. Furthermore, when examining the dashed and solid lines in figure10.c, it becomes apparent that the two quantum wires exhibit different behaviors in response to the impurity potential. While one wire experiences notable shifts in its energy spectrum as a result of impurity potential, the other wire remains relatively unaffected. This selective effect can be attributed to the choice of the Gaussian distribution, which confines the impurity potential influence to specific regions within the quantum wire. Consequently, the difference in the energy profiles between the two wires confirms the localized nature of the impurity potential distribution and their effect on the energy levels of the double quantum wire system.

3.2 Magnetic Properties: Magnetization and Susceptibility

This section presents a comprehensive analysis of the magnetic properties of a double quantum wire system, focusing on the statistical energy, magnetization, and magnetic susceptibility derived from the theoretical framework.

In this work, the exact diagonalization method is employed to solve the Hamiltonian of the doped $InSb$ double quantum wire (DQW) system. This method involves representing the Hamiltonian as a matrix in a chosen finite basis and then numerically diagonalizing the matrix to obtain all eigenvalues (energy levels) and eigenfunctions (wavefunctions), for this purpose, we use a one-dimensional shifted harmonic oscillator basis.

The Hamiltonian includes the kinetic energy, confinement potential, Rashba spin-orbit interaction, electric and magnetic field contributions, and impurity terms. Once the matrix form of the Hamiltonian is constructed, it is diagonalized numerically to obtain the complete energy spectrum and corresponding wavefunctions.

Since the Hamiltonian is represented with a finite number of basis, it is essential to ensure that the results are numerically stable and do not significantly change with further increase in the number of basis states, this process is known as a convergence test.

Testing for convergence is essential, especially in the statistical energy calculations, because statistical energy is a key quantity in determining magnetic and thermodynamic properties such as magnetization, magnetic susceptibility, and entropy. If the statistical energy is not fully converged, errors can propagate into these quantities, leading to incorrect physical calculations, to quantify this, we used a tolerance threshold of 0.0001 meV between successive calculations. This value is sufficiently small to ensure that the result is accurate, but also helps to save computation time by avoiding unnecessary use of very large basis sets.

Therefore, in table3 the convergence of the statistical energy is analyzed by varying the number of basis states in the exact diagonalization method. The statistical energy is calculated for two temperatures values, $T = 0$ and $T = 200K$, where $T = 200K$ represents the highest temperature considered in this study. The results demonstrate that at $T = 0$, the statistical energy converges rapidly because the system is in its ground state. As the number of basis states increases, the statistical energy stabilizes, reaching its converged value at approximately 24 basis states. At $T = 200K$, the convergence is slower because thermal excitations cause higher-energy states to contribute to the statistical energy.

A larger number of basis states is necessary to accurately capture these contributions, with convergence occurring at approximately 28 basis states. To ensure numerical accuracy across all temperatures, 30 basis states are selected in this work. This choice guarantees that the statistical energy is fully converged.

Table 3

The convergence of the statistical energy for $\mu = 0.7\ meV^{\frac{1}{2}}/nm$, $\lambda = 3 * 10^{-4}\ meV/nm^4$.

Number of basis	$\langle E \rangle\ meV\ at\ T = 0$, $B = 0, F = 0, \alpha_R = 0$ *and without impurity*	$\langle E \rangle\ meV\ at\ T = 200K$, $B = 0, F = 0, \alpha_R = 0$ and without impurity	$\langle E \rangle\ meV\ at\ T = 300K$, $B = 1\mathrm{T}, F = 1.5\ mV/nm, \alpha_R = 15meV.nm$ $V_0 = 80\ meV$, $x_1 = 16\ nm, d = 8\ nm$
2	35.3897	45.3199	234.2198
4	29.7261	33.7471	234.2173
6	27.3561	32.4896	234.2171
8	27.3366	31.8295	234.2171
10	26.9049	31.4283	234.2170
12	26.7937	31.495	234.2170
14	26.7937	31.4965	234.2169
16	26.7796	31.4862	234.2169
18	26.7722	31.4915	234.2169
20	26.7715	31.4949	234.2169
22	26.7714	31.4953	234.2169
24	26.7710	31.4954	234.2169
26	26.7710	31.4957	234.2169
28	26.7710	31.4958	234.2169
30	26.7710	31.4958	234.2169
32	26.7710	31.4958	234.2169

Figure 11 (Appendix B), presents The statistical energy versus the external magnetic field at different temperature ($= 0$ and $T = 200\ K$), for low temperature ($T = 0$), the system occupies lower energy states due to the lack of sufficient thermal energy for significant excitations. The step-like behavior or the sharpness observed in the curve arises from transitions between discrete energy levels, which are a result of Landau quantization in the presence of the magnetic field.

At high temperatures ($T = 200\ K$), thermal energy enables population of higher energy states, the increased population of higher states reduces the influence of quantization leading to a smoother increase in the statistical energy curve.

The figure illustrates the dual nature of a double quantum wire system under varying magnetic fields and temperatures. At low temperature, the system exhibits strong quantum effect, while at high temperature, the behavior transitions to a thermally dominated system.

Figure12 (Appendix B), illustrates the variation of the statistical energy with B for two different electric field strengths values($F = 0$ and $F = 1.5\, mV/nm$). The electric field introduces an additional term in the Hamiltonian, which can shift the energy levels, leading to decrease the average statistical energy compared to the case without electric field. In conclusion, without the electric field, the system's statistical energy primarily arises from the magnetic quantization and thermal population of the Landau levels. However, with the electric field, the energy levels are shifted down. As a result, the statistical energy curve demonstrates a noticeable decrease.

The Rashba spin-orbit interaction significantly affect the statistical energy curve in a double quantum wire system as shown in figure13 (Appendix B) which shows the statistical energy as function of B at ($\alpha_R = 0$ and $\alpha_R = 100\, meV.nm$). The Rashba spin-orbit interaction induces spin splitting in the energy levels, creating two distinct spin subbands with different energies. This splitting affecting the statistical energy. Compared to the case without Rashba interaction, the statistical energy curve shows a reduction in the energy because Rashba make spin splitting, and this splitting modifies the population distribution among energy levels, leading to noticeable reduction in the statistical energy curve. For small magnetic fields, the splitting introduced by the Rashba interaction present a broader range of accessible low-energy states. This effect reduces the statistical energy at low magnetic fields. As the magnetic field increases, the energy contribution of Landau quantization dominates, reducing the effect of Rashba-induced splitting.

Figure14 (Appendix B), illustrates the behavior of the magnetization curve at low and high temperatures. At low temperature ($T = 0$), the magnetization curve exhibits sharper cusp. It arises due to the quantization of energy levels into discrete Landau levels. The thermal population of these levels is minimal, and only the lowest energy states are occupied, leading to sharp dip in the magnetization curve. At such low temperatures, quantum effects dominate the magnetization behavior. The sharp negative cusp indicates transitions where higher Landau levels become populated as the magnetic

field increases. At high temperature ($T = 200\ K$), thermal excitation causes population increase of higher states, reduces the influence of quantization leading to reduce the sharpness of the cusp seen at low temperatures, so the magnetization curve becomes flat and continuous. This flattening occurs because of the thermal disruption of the energy states.

In summary, the magnetization behavior at low and high temperatures highlights the interplay between quantum and thermal effects in the system. At low temperature, the sharp cusp in magnetization is directly linked to the quantum confinement of electrons in discrete Landau levels, providing a window into the quantum mechanical nature of the system. At high temperature, the absence of the sharpness in the cusp reflects the dominant role of the thermal distribution of the energy levels.

The effect of the electric field on the magnetization can be explained by considering its influence on the energy levels and the statistical energy as previously discussed. The electric field reduces the system's energy levels by introducing a potential gradient which shifts down the Landau levels. At low magnetic field the magnetization curve in the presence of the electric field shows a smoother variation. At higher magnetic field, the effect of the electric field diminishes as magnetic confinement dominates. Both magnetization curves (with and without the electric field) converge, as the system becomes dominated by the magnetic field as shown in figure15 (Appendix B). This behavior highlights the competing effects of electric and magnetic fields in the double quantum wire system. At higher magnetic field, the magnetization curves converge, indicating the dominance of magnetic field.

The Rashba interaction introduces spin-splitting in the energy levels. At low magnetic field, the part of the Rashba term which independent of the magnetic field dominates, causing a noticeable redistribution of the energy levels. This redistribution creates a sudden enhancement of magnetization, leading to the observed sharp peak (the sharp peak of the dotted curve in figure16 (Appendix B)), so this peak is associated with the Rashba term that is independent of the magnetic field. Across the magnetic field range, the Rashba SOI reduces the overall magnetization as evident from figure16. This is referring to the energy splitting caused by Rashba SOI which has both magnetic dependent and independent terms in the Hamiltonian so this redistribution and splitting

of the energy levels caused by Rashba SOI weakens the net magnetic response of the system.

Figure 17 (Appendix B), illustrates the behavior of magnetic susceptibility as a function of B at two different temperatures. The blue dashed curve represents susceptibility at low temperature ($T = 0$), while the black dotted curve corresponds to higher temperature ($T = 200\ K$). At low temperatures, the susceptibility exhibits a sharp peak at ($B \approx 0.15\ T$), this sharp peak is a characteristic of the low-temperature curve, where the thermal fluctuations are minimal, and there is a transition between discrete energy levels. At high temperature, the susceptibility curve is smoother, with a broader peak and lower amplitude.

Thermal population of higher energy levels causes broadens the discrete energy levels, reducing the system's sensitivity to changes in the magnetic field. This results into smooth variation in the susceptibility curve. At both temperatures, susceptibility transitions from negative to positive as B increase, mean the system transition from diamagnetic behavior to paramagnetic behavior, but the amplitude of susceptibility is significantly higher at low temperatures compared to high temperature and the transition at low temperature curve occurred at smaller magnetic field value compared with the high temperature curve. These differences are due to: at low temperature, the system occupies the lowest Landau levels, leading to a stronger response to magnetic field changes, while, at high temperature, Thermal excitation of higher energy levels broadens the discrete energy states, this reduces how strongly the system reacts to the change in the magnetic field, as a result reducing the susceptibility.

Figure 18 (Appendix B), shows the magnetic susceptibility as a function of B with and without an applied electric field. The susceptibility reflects the system's magnetic response to the changes in the applied magnetic field. In the presence of an electric field, the susceptibility curve exhibits broader features compared to the case without an electric field. The electric field reduces the energy levels, weakening the magnetic response of the system. This behavior results in less sharp peak. In the absence of an electric field, the susceptibility exhibits sharp peak. this feature is characteristic of Landau quantization, where the energy levels are highly discrete. The sharp peak in the susceptibility correspond to transitions between these quantized energy levels. Both curves converge at sufficiently high , where the magnetic field becomes dominant.

Figure 19 (Appendix B), presents the susceptibility as a function of B. The blue dashed line represents the case without Rashba SOC ($\alpha_R = 0$), while the black dotted line includes Rashba SOC ($\alpha_R = 100\, meV.nm$). In the absence of Rashba SOC (blue dashed line), the susceptibility exhibits a sharp peak around($B \approx 0.15\, T$), which corresponds to the Landau level crossing. This peak reflects the system's strong response to the change in the magnetic field. When Rashba coupling is introduced, the susceptibility peak is broadened and reduced in amplitude. This behavior results from the splitting of spin-degenerate levels due to spin-orbit interaction. The Rashba coupling modifies the energy spectrum, reducing the sharpness of quantum transitions and weakening the system's magnetic response.

At high values of (B), the susceptibility curves with and without Rashba begin to converge. This indicates that the effect of Rashba coupling diminishes in strong magnetic fields, where Landau level quantization dominates.

3.3 The Magnetocaloric Effect (MCE)

The magnetocaloric effect (MCE) describes the temperature change in a material when exposed to a varying magnetic field. This property is particularly important for low-temperature cooling technologies and sensitive magnetic sensors. In this section, we analyze the entropy change and adiabatic temperature variation in the $InSb$ double quantum wire system. The influence of spin-orbit coupling, impurity effects, and external electric fields on the MCE is explored in detail.

Figure20 (Appendix B), shows the magnetic entropy as a function of the temperature for two different values of the magnetic field (Blue curve $B = 0$, Orange curve $B = 0.05\, T$). For both curves, entropy starts near zero at very low temperatures and increases as temperature rises. This behavior is expected because, at low temperatures, the system is in more ordered state with most spins aligned. As the temperature increases, thermal excitations introduce disorder, increasing entropy. When a magnetic field is applied, the system tends to align its spins along the field direction, reducing randomness and lowering entropy, it is clear from the figure that the blue curve ($B = 0$) shows higher entropy compared to the orange curve ($B = 0.05\, T$) at the same temperature. As the temperature increases, the difference between the two curves decreases. At high temperatures, thermal energy dominates over the effect of the

magnetic field, making both curves approach similar entropy values. This suggests that at high T, spin alignment due to B becomes less significant compared to the thermal disorder. The figure confirms that the magnetic field reduces the entropy at low temperatures, means that MCE is most efficient in this range. The entropy difference between the two curves indicates the efficiency of MCE, larger difference in S means stronger MCE.

Figure 21 (Appendix B), presents the variation of the magnetic entropy change (ΔS) as a function of the temperature for different magnetic field differences (ΔB) values. Each curve exhibits a peak at a specific temperature range. For all values of ΔB, the entropy change initially increases as temperatures increase, reaches a maximum value, and then gradually decreases. This behavior reflects the interplay between thermal fluctuations and magnetic field-induced ordering. Each curve has a peak, indicating the temperature range where the maximum magnetocaloric effect (MCE) occurs. As ΔB increases, the peak shifts towards higher temperatures and broadens. This behavior indicates that increasing the magnetic field enhances the temperature range over which entropy change occurs. The width of the ΔS curves is another important factor. While the green curve ($\Delta B = 0.15\ T$) has a high ΔS over a wider range of temperatures, its peak value is lower than the blue curve. This indecates that increasing ΔB broadens the temperature response range but does not necessarily enhance the peak value in the entropy change curves, so that the material undergoes a more extended transition region under stronger magnetic field, making it more effective over a wider temperature range. The broader response is beneficial for applications requiring operation over a wider temperature range, while a sharper peak may be more effective for applications focused on maximizing cooling power at a specific temperature.

Table 4

The refrigerant capacity at deferent ΔB values for $(T_{\text{low}} = 0 \ and \ T_{high} = 25\ K)$ and for $(T_{low} = 0 \ and \ T_{high} = 75\ K)$, for $\mu = 0.84 \frac{meV^{\frac{1}{2}}}{nm}$, $\lambda = 3 * 10^{-4} \frac{meV}{nm^4}$, $F = 0$, $\alpha_R = 0$ and without impurity

$\Delta B\ (T)$	$RC\ (K_B T)$ for $T_{low} = 0 \ and \ T_{high} = 25\ K$	$RC\ (K_B T)$ for $T_{low} = 0 \ and \ T_{high} = 75\ K$
0.01	3.49594	4.7025
0.02	6.21568	9.05736
0.03	8.0349	12.4436
0.04	8.81014	14.2617
0.05	8.28587	14.1607
0.06	6.16403	12.3481
0.07	2.69682	9.819
0.08	0.748975	8.04223
0.09	1.33477	11.992
0.1	1.38314	13.7238
0.11	0.0240493	13.8779
0.12	1.59966	16.9303
0.13	3.51707	20.3248
0.14	4.89923	23.1133
0.15	5.70542	25.1616
0.16	5.99488	26.4758
0.17	5.8499	27.1397
0.18	5.35799	27.283
0.19	4.62788	27.0743
0.2	3.83336	26.7452

The refrigerant capacity (RC) is an essential parameter that quantifies the total amount of heat that can be transferred between the cold and hot reservoirs during a cooling cycle. High RC (large area under the curve) indicates that the material can absorb and release more heat per each cycle. It is defined as:

$$RC = \int_{T_1}^{T_2} \Delta S(T) dT \tag{3.1}$$

In the figure, RC corresponds to the area under each curve, which indicates the total entropy change over a given temperatures range. The temperatures T_1 and T_2 correspond to the low and high temperatures , respectively.

To gain a deeper understanding of the behavior of the system, the refrigerant capacity (RC) was calculated for two temperature intervals $(0\ to\ 25K)$ and $(0\ to\ 75K)$. The area under each curve, which represents RC, is presented in Table4.

By analyzing the data in the table for RC at the two temperature intervals, we can see how the magnitude of ΔB affects the efficiency of the magnetocaloric effect. This analysis provides valuable vision into selecting the most appropriate ΔB based on the operational temperature range of the system.

For narrow temperature range $(0\ to\ 25K)$, where cooling is required within a narrow interval, a small ΔB is more effective, where $\Delta B = 0.04\ T$ has the highest RC value . This is because small ΔB values lead to sharper entropy peaks, maximizing the cooling effect over a localized temperature window. The rapid variation in entropy ensures efficient heat absorption and release within the specific range. In contrast, for wide temperature ranges, a larger ΔB is more suitable, where $\Delta B = 0.18\ T$ has the highest RC value. As ΔB increases, the entropy change curve broadens, spreading the cooling effect over a wider temperature range and the peaks become slightly lower.

Figure 22 (Appendix B), illustrates the variation of the (RC) as a function of the Rashba parameter α_R. The figure shows that as α_R increases, RC also increases in a nonlinear curve. This indicates that the strength of the Rashba spin-orbit interaction plays a significant role in enhancing the cooling performance of the system. Rashba spin-orbit interaction can be an effective strategy for improving cooling performance. Tuning $\alpha_R$through various methods, such as selecting materials with strong Rashba coupling (e.g. $InSb$), applying an external electric field or gate voltage in heterostructures, and modifying the structure or thickness of semiconductor layers, can enhance the Rashba spin-orbit interaction. This enhancement, in turn, could lead to more efficient RC by optimizing the system's thermal and magnetic response.

The increasing in Rashba SOC enhances the refrigerant capacity (RC), improving the efficiency of thermal energy exchange. This finding is vital for developing advanced magnetocaloric materials where spin-orbit interactions can be engineered to optimize cooling performance. The ability to control α presents an additional degree of freedom for designing next-generation cooling technologies based on quantum materials.

The results of this study reveal a particularly interesting and important trend: as the strength of the Rashba spin–orbit coupling (SOC) increases, there is a noticeable and consistent enhancement in the refrigerant capacity (RC) of the system. In simpler terms, the system becomes more effective at exchanging thermal energy, which is a central requirement for any cooling process. This improvement isn't just a minor detail it actually opens up new possibilities for how we think about and design materials with strong magnetocaloric responses. What makes this especially significant is the fact that Rashba SOC is not a fixed property; rather, it can be tuned or controlled by external means, such as electric fields or structural modifications in the quantum wire. That means we're not just observing a passive effect we're identifying a practical way to actively manipulate and improve performance. The ability to control the Rashba coefficient, introduces a powerful and flexible tool into the field of quantum materials and nanoscale refrigeration. This added level of tunability makes it feasible to customize materials for specific applications, especially in environments where space, energy efficiency, and precision are critical. It's not just about achieving low temperatures; it's about doing so efficiently, reliably, and in a way that can be scaled or adapted to emerging technologies. When we talk about next-generation cooling systems whether in quantum computing, sensitive electronics, or miniature sensors the potential to engineer spin–orbit interactions directly into the design becomes changing advantage. Rather than relying solely on traditional material properties, we can now envision cooling technologies that are fundamentally rooted in quantum mechanical principles, giving researchers and engineers a much broader design space. This also aligns with current trends in condensed matter physics, where the interplay between spin, charge, and thermal properties is being explored not only for academic interest but for real-world innovation. In that sense, the observed relationship between Rashba SOC and RC isn't just a theoretical insight it's a concrete step toward smarter, more adaptable cooling technologies shaped by the physics of spin orbit coupling.

Figure 23 (Appendix B), shows the variation of (RC) as a function of the impurity position (x_1) in the double quantum wire system. From the figure, we can see that RC is relatively not affected when the impurity is close to the central barrier, it increases as the impurity moves away from the barrier toward the center of one of the quantum wires, reaches a peak, and then decreases again as the impurity moves further toward the edge.

Near the central barrier the impurity has a minimal effect because the barrier already strongly confines the electrons, the energy states and the probability density remain unchanged, leading to weak modifications in the entropy and, consequently, the RC. As the impurity moving away from the barrier towards the wire's center, the impurity starts to interact more effectively with the electronic states. It modifies the energy spectra and the probability density distribution. This results in enhancing the entropy change and as a result, RC increases, reaching a maximum value at an optimal impurity position. As the impurity moves further away from the center of the wire, its influence on the system begins to weaken. The impurity's effect is weak at the edges due to the low probability density and strong confinement potential in these regions, this causes RC to decrease beyond the peak position.

The behavior of RC is directly related to how the impurity modifies the system's energy states and the probability density distribution. When the impurity is optimally positioned, it leading to a peak in the RC value. This suggests that tuning the impurity by carefully selecting the impurity position is an effective way to control cooling performance in the double quantum wire systems.

In conclusion, the results clearly show that the position of the impurity has a strong impact on the system's energy structure and charge distribution. By placing the impurity in the right spot, we can significantly enhance the RC value, which means better cooling performance. This highlights how impurity tuning can be a simple yet powerful tool for optimizing double quantum wire devices.

Figure 24(Appendix B) presents the variation of refrigerant capacity (RC) as a function of the impurity strength (V_0) in a double quantum wire system. The results show that RC increases steadily as the impurity strength increases before slowly saturating at higher values. This behavior suggests that the impurity strength enhances the system's

refrigerant capacity up to a certain point, beyond which further increases in impurity strength have no effect.

A crucial factor in this analysis is the impurity position (x_1), which is set at $25\ nm$. This choice is based on the result of Figure23, where RC exhibited its strongest response when plotted against impurity position for a fixed value of V_0. Thus, selecting the impurity to be in this position ensures that the impurity has the most significant effect, which making it a key parameter in optimizing the refrigerant capacity of the system.

Figure 25 (Appendix B), presents the effect of the strength of the applied external electric field (F) on the refrigerant capacity (RC). The observed behavior of RC as a function of F can be explained based on how the electric field influences the energy states in the double quantum wire system. At low values of F, RC increases rapidly. This refer to the fact that the electric field shifts the electron wavefunctions within the wire, modifying the energy levels and enhancing the entropy change ΔS. Since RC is directly related to ΔS, this leads to a noticeable increase in RC. As F increases beyond a certain point (approximately $F \approx 0.5$ mV/nm), the RC curve flattens, indicating that further increases in F no longer significantly enhance RC. This saturation effect suggests that the electric field has already induced enough redistribution of electronic states, and additional increases in F do not contribute further to the entropy change.

The results indicate that applying an external electric field can enhance RC, but only up to a certain value. Beyond this value, increasing F does not provide further benefits.

Chapter Four
Conclusion

This theoretical study provides a detailed analysis of the electronic, magnetic, and thermodynamic properties of a double quantum wire (DQW) system fabricated from indium antimonide ($InSb$), a material distinguished by its strong spin-orbit coupling and high electron mobility. By solving the system's Hamiltonian by using exact diagonalization method, we systematically explore how the structural parameters of the confinement potential, external electric and magnetic fields, Rashba spin-orbit coupling (SOC), and impurity potential shape the electronic structure, magnetic response, and thermodynamic properties of the system. From the results we were able to identify the key factors that significantly influence the system's performance and behavior. These factors include spin-orbit coupling, external electric and magnetic fields, and impurity potential, all of which play a critical role in shaping the electronic, magnetic, and thermodynamic properties of the system. The findings offer valuable insights into the design of advanced nanoscale devices, as they demonstrate how these parameters can be adjusted to optimize performance for specific applications.

The electronic structure of the DQW system is highly sensitive to the structural parameters of the confinement potential (μ and λ) and the Rashba SOC, which modify the energy dispersion and create spin-split quantum states. These spin-polarized states, arising from the SOC and the external magnetic field, enable exact control over electron spin which is critical feature for spintronic applications such as spin-based transistors or quantum memory devices. External magnetic fields further induce an oscillatory magnetization behavior, and causing a quantum phase transitions that depend on field strength.

The impurity potentials introduce asymmetry into the system, breaking spatial symmetry between the two quantum wires and redistributing electron probability densities. This asymmetry leads to selective energy shifts, where one wire experiences significant spectral modifications while the other remains largely unaffected. Impurity also affect the local density of states ($LDOS$). The magnetic susceptibility and the magnetization are studied, the system show a transition from diamagnetic to paramagnetic behavior.

The magnetocaloric effect (MCE) is investigated through the entropy changes (ΔS) and the refrigerant capacity (RC) under varying the magnetic field strength. Our calculations demonstrate that the Rashba SOC enhances the refrigerant capacity. Additionally, the influence of the impurity on the refrigerant capacity has been systematically investigated and the analysis shows that at a specific position, the impurity enhances the refrigerant capacity of the system, the calculations show that the presence of the external electric fields improved the refrigerant capacity of the system up to a critical value. Beyond this value further increases in the electric field do not yield additional enhancements in the refrigerant capacity of the system.

In conclusion, this thesis has provided a detailed understanding of the electronic, magnetic, and thermodynamic properties of the InSb-based double quantum wire system. By examining the effects of impurity potentials, Rashba spin-orbit coupling, and external electric and magnetic fields, we have shown how these factors can be used to control the system's properties. These findings offer valuable insights for the development of advanced quantum devices and materials.

List of Abbreviations

Abbreviation	Meaning
SOC	Spin-Orbit Coupling
DQW	double quantum wire
$LDOS$	local density of states
DOS	Density of states
$2D$	Two-dimension
$1D$	One-dimensional
$3D$	Three-dimension
$0D$	Zero-dimension
MCE	magnetocaloric effect
S	Entropy
M	Magnetization
χ	Magnetic susceptibility
n	Principal quantum number
ω_c	Cyclotron frequency
RC	refrigerant capacity
λ	Parameter that controls the strength of the confinement
μ	Separation between the minima of double-well potential
k_{eff}	Effective spring constant
F	Strength of the electric field
V_{conf}	Confinement potential
B	Magnetic field
F	Electric field

ω_0	Isotropic radial confinement frequency
m^*	Effective mass
$\hbar$	Reduced Plank constant
e	Electron charge
V_0	Impurity strength
d	Impurity stretches
μ_B	Bohr magneton
α_R	Rashba coefficient
σ	Pauli matrices
δ	Kronic Delta
ψ	Wave function
Z	Partition function
Γ	Broadening factor
E_n	Energy value for the nth eigenstate
QWs	Quantum wires
VLS	Vapor-liquid-solid
EBL	Electron-beam lithography
$LEDs$	Light-emitting diodes
$MRAM$	Magnetoresistive random-access memory
$RSOC$	Rashba spin-orbit coupling
SdH	Shubnikov–de Haas
STM	Scanning tunneling microscopy
E_F	Fermi level
V_{bias}	Bias voltage

STS	Scanning tunneling spectroscopy
LLs	Landau levels
ΔS_{iso}	Isothermal entropy change
g^*	Effective Lande g-factor
p_x, p_y	X and y components of the momentum operator
μ_B	Bohr magneton
ω	Effective oscillator frequency
l_0	Characteristic length of the harmonic oscillator
x_0	Guiding center coordinate
k_B	Boltzmann constant
$\langle E \rangle$	Averaged energy
N	Number of basis states
E_f	Highest energy level
SQW	Single quantum wire
T	Temperature
RC	Refrigerant capacity
x_1	Impurity position

References

[1] Dakhlaoui, H., *Linear and nonlinear optical absorption coefficients and refractive index changes in GaN/AlxGa (1− x) N double quantum wells operating at 1.55 μm.* Journal of applied physics, 2015. 117(13).

[2] Ali, M., & Elsaid, M. K. (2024). Effect of structural parameters, and spin-orbit interaction on the electronic properties of double quantum wire systems in the presence of external magnetic field. Nanosystems: Physics, Chemistry, Mathematics, *15*(5), 658-669.

[3] Shilpa, G., et al., *Recent advances in the development of high efficiency quantum dot sensitized solar cells (QDSSCs): A review.* Materials Science for Energy Technologies, 2023. 6: p. 533-546.

[4] Chen, W. and P.R. i Cabarrocas, *Rational design of nanowire solar cells: from single nanowire to nanowire arrays.* Nanotechnology, 2019. 30(19): p. 194002.

[5] Espinet-Gonzalez, P., et al., *Radiation tolerant nanowire array solar cells.* ACS nano, 2019. 13(11): p. 12860-12869.

[6] Hsu, C.-L., et al., *Ultraviolet/visible photodetectors based on p–n NiO/ZnO nanowires decorated with Pd nanoparticles.* ACS Applied Nano Materials, 2019. 2(10): p. 6343-6351.

[7] Liao, Q.-L., et al., *A single nanowire sensor for intracellular glucose detection.* Nanoscale Research Letters, 2019. 11(22): p. 10702-10708.

[8] Robertson, K.W., R.R. LaPierre, and J.J. Krich, *Efficient wave optics modeling of nanowire solar cells using rigorous coupled-wave analysis.* Optics express, 2019. 27(4): p. A133-A147.

[9] Wu, Y. and P. Yang, *Direct observation of vapor− liquid− solid nanowire growth.* Journal of the American Chemical Society, 2001. 123(13): p. 3165-3166.

[10] Madaria, A.R., et al., *Toward optimized light utilization in nanowire arrays using scalable nanosphere lithography and selected area growth.* Nano letters, 2012. 12(6): p. 2839-2845.

[11] Fischer, S., et al., *Tunnel-coupled one-dimensional electron systems with large subband separations.* Physical Review B—Condensed Matter 2006. 74(11): p. 115324.

[12] El-Said, M., *The energy states of excitons in a harmonic quantum dot.* physica status solidi, 1994. 184(2): p. 385-392.

[13] El-Said, M., *The magnetoabsorption spectra of donors in a quantum well wire.* Semiconductor science technology, 1994. 9(10): p. 1787.

[14] El-Said, M., *The energy level ordering in two-electron quantum dot spectra.* Superlattices microstructures, 1998. 23(6): p. 1237-1243.

[15] Lei, Z., et al., *Quantum transport in high-quality shallow InSb quantum wells.* Applied Physics Letters, 2019. 115(1).

[16] Sun, P., et al., *Recent advances in quantum dots photocatalysts.* Chemical Engineering Journal, 2023. 458: p. 141399.

[17] Zhang, J., et al., *Colloidal quantum dots: synthesis, composition, structure, and emerging optoelectronic applications.* Laser, 2023. 17(3): p. 2200551.

[18] Shan, Q., et al., *Perovskite quantum dots for the next-generation displays: progress and prospect.* Advanced Functional Materials, 2024. 34(36): p. 2401284.

[19] Martynenko, I., et al., *Application of semiconductor quantum dots in bioimaging and biosensing.* Journal of Materials Chemistry B, 2017. 5(33): p. 6701-6727.

[20] Hao, M., et al., *Perovskite quantum dot solar cells: current status and future outlook: focus review.* ACS Energy Letters, 2024. 9(1): p. 308-322.

[21] Schliemann, J., J.C. Egues, and D. Loss, *Nonballistic spin-field-effect transistor.* Physical review letters, 2003. 90(14): p. 146801.

[22] Bravyi, S., et al., *The future of quantum computing with superconducting qubits.* Journal of Applied Physics, 2022. 132(16).

[23] Naydenov, B. and J.J. Boland, *Variable-height scanning tunneling spectroscopy for local density of states recovery based on the one-dimensional WKB approximation.* Physical Review B—Condensed Matter, 2010. 82(24): p. 245411.

[24] Murayama, M., et al., *Gallium nitride-based resonant tunneling diode oscillators.* Applied Physics Letters, 2024. 125(11).

[25] Simhony, S., et al., *Double quantum wire GaAs/AlGaAs diode lasers grown by organometallic chemical vapor deposition on grooved substrates.* IEEE Photonics Technology Letters, 1990. 2(5): p. 305-306.

[26] Jakubczyk, P., K. Majchrowski, and I. Tralle, *Quantum entanglement in double quantum systems and Jaynes-Cummings model.* Nanoscale research letters, 2017. 12: p. 1-9.

[27] Žutić, I., J. Fabian, and S.D. Sarma, *Spintronics: Fundamentals and applications.* Reviews of modern physics, 2004. 76(2): p. 323.

[28] Wolf, S., et al., *Spintronics: a spin-based electronics vision for the future.* science, 2001. 294(5546): p. 1488-1495.

[29] Žutić, I., J. Fabian, and S.D. Sarma, *Spintronics: Fundamentals and applications.* Reviews of modern physics, 2004. 76(2): p. 323.

[30] Kumar, M., et al., *Energy dispersion and electron g-factor of quantum wire in external electric and magnetic fields with Rashba spin orbit interaction.* Superlattices Microstructures, 2013. 57: p. 11-18.

[31] Knobbe, J. and T. Schäpers, *Magnetosubbands of semiconductor quantum wires with Rashba spin-orbit coupling.* Physical Review B—Condensed Matter, 2005. 71(3): p. 035311.

[32] Zhang, S., et al., *Magnetosubbands of semiconductor quantum wires with Rashba and Dresselhaus spin-orbit coupling.* Physical Review B—Condensed Matter, 2006. 73(15): p. 155316.

[33] Malet, F., et al., *Exchange-correlation effects on quantum wires with spin-orbit interactions under the influence of in-plane magnetic fields.* Physical Review B—Condensed Matter, 2007. 76(11): p. 115306.

[34] Schäpers, T., J. Knobbe, and V. Guzenko, *Effect of Rashba spin-orbit coupling on magnetotransport in InGaAs/ InP quantum wire structures.* Physical Review B—Condensed Matter, 2004. 69(23): p. 235323.

[35] Noat, Y., et al., *Unconventional superconductivity in ultrathin superconducting NbN films studied by scanning tunneling spectroscopy.* Physical Review B—Condensed Matter, 2013. 88(1): p. 014503.

[36] Lodge, M.S., et al., *Atomically thin quantum spin hall insulators.* Advanced Materials, 2021. 33(22): p. 2008029.

[37] Yin, L.-J., et al., *Landau quantization of Dirac fermions in graphene and its multilayers.* Frontiers of Physics, 2017. 12: p. 1-37.

[38] Negrete, O.A., F.J. Peña, and P. Vargas, *Magnetocaloric effect in an antidot: The effect of the Aharonov-Bohm flux and antidot radius.* Entropy, 2018. 20(11): p. 888.

[39] Tishin, A., et al., *A review and new perspectives for the magnetocaloric effect: New materials and local heating and cooling inside the human body.* International Journal of Refrigeration, 2016. 68: p. 177-186.

[40] Reis, M.S., *Oscillating magnetocaloric effect.* Applied Physics Letters, 2011. 99(5).

[41] Reis, M., *Oscillating adiabatic temperature change of diamagnetic materials.* Applied Physics Letters, 2012. 152(11): p. 921-923.

[42] Paixão, L., Z. Alisultanov, and M. Reis, *Oscillating adiabatic temperature change of 2D diamagnetic materials.* Journal of magnetism, 2014. 368: p. 374-378.

[43] Smith, A., et al., *Materials challenges for high performance magnetocaloric refrigeration devices.* Advanced Energy Materials, 2012. 2(11): p. 1288-1318.

[44] Treado, P.J., I.W. Levin, and E.N. Lewis, *Indium antimonide (InSb) focal plane array (FPA) detection for near-infrared imaging microscopy.* Applied spectroscopy, 1994. 48(5): p. 607-615.

[45] Shkedy, L., et al., *Megapixel digital InSb detector for midwave infrared imaging.* Optical Engineering, 2011. 50(6): p. 061008-061008-8.

[46] Frolov, S.M., et al., *Quantum computing based on semiconductor nanowires.* MRS bulletin, 2013. 38(10): p. 809-815.

[47] Yang, Z., et al., *Spin transport in ferromagnet-InSb nanowire quantum devices.* Nano letters, 2020. 20(5): p. 3232-3239.

[48] Peng, L., et al., *InSb/InP Core–Shell Colloidal Quantum Dots for Sensitive and Fast Short-Wave Infrared Photodetectors.* ACS nano, 2024. 18(6): p. 5113-5121.

[49] Sandhu, A., et al., *High sensitivity InSb ultra-thin film micro-hall sensors for bioscreening applications.* Japanese journal of applied physics, 2004. 43(7A): p. L868.

[50] Bouarissa, N. and H. Aourag, *Effective masses of electrons and heavy holes in InAs, InSb, GaSb, GaAs and some of their ternary compounds.* Infrared physics technology, 1999. 40(4): p. 343-349.

[51] Nilsson, H.A., et al., *Giant, level-dependent g factors in InSb nanowire quantum dots.* Nano letters, 2009. 9(9): p. 3151-3156.

[52] Kriegner, D., et al., *Unit cell structure of crystal polytypes in InAs and InSb nanowires.* Nano letters, 2011. 11(4): p. 1483-1489.

[53] Rahou, D., et al., *Electronic and optical properties of InSb quantum dots from pseudopotential calculation.* Chinese Journal of Physics, 2020. 66: p. 206-213.

[54] Gumber, S., et al., *Thermal and magnetic properties of cylindrical quantum dot with asymmetric confinement.* Canadian Journal of Physics, 2015. 93(11): p. 1264-1268.

[55] BZOUR, F. and M.K. ELSAID, *THE EFFECTS OF PRESSURE AND TEMPERATURE ON THE MAGNETIZATION OF A PARABOLIC QUANTUM DOT IN A MAGNETIC FIELD.* Malaysian Journal of Science, 2018. 37(2): p. 103-117.

[56] Alia, A.A., et al., *Effect of Tilted Electric Field and Magnetic Field on the Energy Levels, Binding Energies and Heat Capacity of Donor Impurity in GaAs Quantum Dot.* Indian Journal of Pure & Applied Physics (IJPAP), 2021. 5.

[57] Elsaid, M., M. Ali, and A. Shaer, *The energy spectra and heat capacity of gaas gaussian quantum dot in an external magnetic field.* Baghdad Science Journal, 2021. 18(2): p. 0409-0409.

[58] Elsaid, M.K., M.A. Al-Naafa, and S. Zugail, *Spin singlet-triplet energy splitting in the ground state of a quantum dot with a magnetic field: effect of dimensionality.* Journal of Computational Theoretical Nanoscience, 2008. 5(4): p. 677-680.

[59] Datta, N.K. and M. Ghosh, *Impurity strength and impurity domain modulated frequency-dependent linear and second non-linear response properties of doped quantum dots.* physica status solidi, 2011. 248(8): p. 1941-1948.

[60] Boda, A. and A. Chatterjee, *Transition energies and magnetic properties of a neutral donor complex in a Gaussian GaAs quantum dot.* Superlattices Microstructures, 2016. 97: p. 268-276.

[61] Alia, A.A., M.K. Elsaid, and A. Shaer, *Magnetic properties of GaAs parabolic quantum dot in the presence of donor impurity under the influence of external tilted electric and magnetic fields.* Journal of Taibah University for Science, 2019. 13(1): p. 687-695.

[62] Elsaid, M.K., et al., *Impurity effects on the magnetization and magnetic susceptibility of an electron confined in a quantum ring under the presence of an external magnetic field.* Chinese Journal of Physics, 2020. 64: p. 9-17.

[63] Hosseinpour, P., *Effect of Gaussian impurity parameters on the valence and conduction subbands and thermodynamic quantities in a doped quantum wire.* Physica B: Condensed Matter, 2020. 322: p. 114061.

[64] Shaer, A., E. Hjaz, and M.K. Elsaid, *The influence of off-centre donor impurity on the tuning of the quantum ring magnetic susceptibility.* Chemical Physics Impact, 2023. 6: p. 100194.

[65] El-Said, M., *Effects of applied magnetic field on the energy levels of shallow donors in a parabolic quantum dot.* Physica B: Condensed Matter, 1994. 202(1-2): p. 202-206.

[66] Elsaid, M., M. Ali, and A. Shaer, *The magnetization and magnetic susceptibility of GaAs Gaussian quantum dot with donor impurity in a magnetic field.* Modern Physics Letters B, 2019. 33(34): p. 1950422.

[67] Ali, A.A., A. Shaer, and M. Elsaid, *Simultaneous effects of Rashba, magnetic field and impurity on the magnetization and magnetic susceptibility of a GaAs-semiconductor quantum ring.* Journal of Magnetism Magnetic Materials, 2022. 556: p. 169435.

[68] Ibrahim, N., et al., *Effects of Rashba spin–orbit interaction and topological defect on the magnetic properties of an electron confined in a 2D quantum dot.* Journal of Taibah University for Science, 2021. 15(1): p. 1210-1216.

[69] Hosseinpour, P., *The role of Rashba spin-orbit interaction and external fields in the thermal properties of a doped quantum dot with Gaussian impurity.* Physica B: Condensed Matter, 2020. 593: p. 412259.

[70] Elsaid, M.K., A.A. Alia, and A. Shaer, *Rashba spin-orbit interaction effects on thermal and magnetic properties of parabolic GaAs quantum dot in the presence of donor impurity under external electric and magnetic fields.* Chinese Journal of Physics, 2020. 66: p. 335-348.

[71] Voskoboynikov, O., et al., *Magnetic properties of parabolic quantum dots in the presence of the spin–orbit interaction.* Journal of applied physics, 2003. 94(9): p. 5891-5895.

[72] Su, Y., et al., *Nonlinear optical properties of semiconductor double quantum wires coupled to a quantum-sized metal nanoparticle.* Optics Letters, 2020. 45(2): p. 379-382.

[73] Huang, D., et al., *Field-induced modulation of the conductance, thermoelectric power, and magnetization in ballistic coupled double quantum wires under a tilted magnetic field.* Physical Review B—Condensed Matter, 2008. 77(8): p. 085320.

[74] Wang, D.-W., E. Mishchenko, and E. Demler, *Pseudospin ferromagnetism in double-quantum-wire systems.* Physical review letters, 2005. 95(8): p. 086802.

[75] Moon, J., et al., *Magnetoresistance of one-dimensional subbands in tunnel-coupled double quantum wires.* Physical Review B—Condensed Matter, 1999. 60(16): p. 11530.

[76] Gudmundsson, V. and C.-S. Tang, *Magnetotransport in a double quantum wire: Modeling using a scattering formalism built on the Lippmann-Schwinger equation.* Physical Review B—Condensed Matter, 2006. 74(12): p. 125302.

[77] Gisi, B., et al., *Effects of an in-plane magnetic field on the energy dispersion, spin texturing and conductance of double quantum wires.* Superlattices Microstructures, 2016. 91: p. 391-400.

[78] Korepov, S. and M. Liberman, *Tunnel-coupled double quantum wires in a magnetic field: electron scattering on impurities and boundary roughness.* Physica B: Condensed Matter, 2002. 322(1-2): p. 92-109.

[79] Sarıkurt, S., et al., *Spin texturing in a parabolically confined quantum wire with Rashba and Dresselhaus spin—orbit interactions.* Chinese Physics B, 2013. 23(1): p. 017102.

[80] Karaaslan, Y., et al., *Spin–orbit interaction and magnetic field effects on the energy dispersion of double quantum wire.* Superlattices Microstructures, 2015. 85: p. 401-409.

[81] Karaaslan, Y., et al., *Electric and magnetic field modulated energy dispersion, conductivity and optical response in double quantum wire with spin-orbit interactions.* Physics Letters A, 2018. 382(7): p. 507-515.

[82] Reis, M., *Oscillating magnetocaloric effect of a two dimensional non-relativistic diamagnetic material.* Journal of Applied Physics, 2013. 113(24).

[83] Reis, M., *Oscillating magnetocaloric effect on graphenes.* Applied Physics Letters, 2012. 101(22).

[84] Alisultanov, Z., *Oscillating magnetocaloric effect in size-quantized diamagnetic film.* Journal of Applied Physics, 2014. 115(11).

[85] Alisultanov, Z., et al., *Oscillating magnetocaloric effect in quantum nanoribbons.* Physica E: Low-dimensional Systems Nanostructures, 2015. 65: p. 44-50.

[86] Martín-Jiménez, A., et al., *Unveiling the radiative local density of optical states of a plasmonic nanocavity by STM.* Nature communications, 2020. 11(1): p. 1021.

[87] Widmer, R., et al., *Experimental signatures of spiky local density of states in quasicrystals.* Physical Review B—Condensed Matter, 2009. 79(10): p. 104202.

[88] Segovia-Chaves, F., H. Vinck-Posada, and E.P. Navarro-Barón, *Local density of states in a one-dimensional photonic crystal with a semiconducting cavity.* Results in Physics, 2022. 33: p. 105129.

[89] Ignatchenko, V. and D. Tsikalov, *Local density of states in one-dimensional photonic crystals and sinusoidal superlattices.* Physics Procedia, 2017. 86: p. 113-116.

[90] Bena, C. and S.A. Kivelson, *Quasiparticle scattering and local density of states in graphite.* Physical Review B—Condensed Matter Materials Physics, 2005. 72(12): p. 125432.

[91] Shimomura, Y., Y. Takane, and K. Wakabayashi, *Electronic states and local density of states in graphene with a corner edge structure.* Journal of the Physical Society of Japan, 2011. 80(5): p. 054710.

[92] Li, J., et al., *Observation of spin dependent photocoductivity in InSb quantum well nanowires.* Applied Physics Letters, 2012. 101(15).

[93] Schmidt, T.L., *Finite-temperature conductance of interacting quantum wires with Rashba spin-orbit coupling.* Physical Review B—Condensed Matter, 2013. 88(23): p. 235429.

[94] Poghosyan, B.Z., *Binding energy of hydrogen-like impurities in quantum well wires of InSb/GaAs in a magnetic field.* Nanoscale Research Letters, 2007. 2: p. 515-518.

[95] Khomitsky, D., E. Lavrukhina, and E.Y. Sherman, *Electric dipole spin resonance at shallow donors in quantum wires.* Physical Review B—Condensed Matter, 2019. 99(1): p. 014308.

[96] Zhukov, N., E. Glukhovskoy, and D. Mosiyash, *Local field emission spectroscopy of InSb micrograins.* Technical Physics Letters, 2015. 41: p. 1068-1071.

[97] Zhang, L.Z., W. Sun, and P. Cheng, *Spectroscopic and theoretical studies of quantum and electronic confinement effects in nanostructured materials.* Molecules, 2003. 8(1): p. 207-222.

[98] Rastegar-Sedehi, H., *Magnetocaloric effect in Rashba spin-orbit coupling and Zeeman splitting of a narrow nanowire quantum dot.* The European Physical Journal Plus, 2021. 136(5): p. 1-8.

[99] Chen, Q., L. Li, and F. Peeters, *Magnetic field dependence of electronic properties of MoS 2 quantum dots with different edges.* Physical Review B—Condensed Matter, 2018. 97(8): p. 085437.

Appendices

Appendix A

Published Paper

NANOSYSTEMS:
PHYSICS, CHEMISTRY, MATHEMATICS

Original article

Ali M., Elsaid M. *Nanosystems: Phys. Chem. Math.*, 2024, **15** (5), 658–669.
http://nanojournal.ifmo.ru
DOI 10.17586/2220-8054-2024-15-5-658-669

Effect of structural parameters, and spin-orbit interaction on the electronic properties of double quantum wire systems in the presence of external magnetic field

Mahmoud Ali, Mohammad Elsaid

Physics Department, An-Najah National University, Palestine

Corresponding author: Mohammad Elsaid, mkelsaid@najah.edu

ABSTRACT This study explores the effect of the structural parameters of the confining potential and external magnetic field on the electronic properties of a double quantum wire (DQW) system. Using theoretical analysis and graphical representations, we investigate the effects of varying parameters such as structural parameters (μ and λ) on the confinement potential profiles, probability density distributions and energy spectra of DQWs. Furthermore, we investigate the effect of variation of the confinement potential, the Rashba spin-orbit coupling and the external magnetic field on the energy spectra and the local density of states of the system. The changes in the energy spectra and the local density of states of the system due to Rashba spin-orbit coupling, and the external magnetic field were highlighted. The shifts and variations in energy and in the local density of states were discussed in detail. Our research results provide valuable insights into possibility of using the structural parameters and the external magnetic fields for control the electronic properties of the double quantum wire system.

KEYWORDS double quantum wire, spin-orbit interaction, local density of states

FOR CITATION Ali M., Elsaid M. Effect of structural parameters, and spin-orbit interaction on the electronic properties of double quantum wire systems in the presence of external magnetic field. *Nanosystems: Phys. Chem. Math.*, 2024, **15** (5), 658–669.

Appendix B

Figures of Study

Figure 11

The statistical energy versus B *for* $\mu = 0.7\frac{meV^{\frac{1}{2}}}{nm}$, $\lambda = 3 * 10^{-4}\frac{meV}{nm^4}$, $F = 0$, $\alpha_R = 0$ *and without impurity at* $T = 0$ *and* $T = 200\ K$

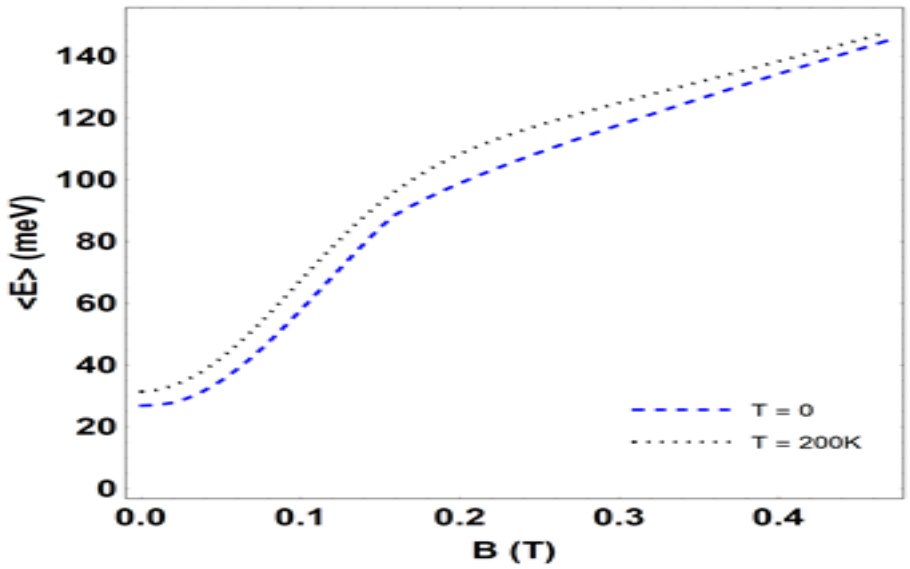

Figure 12

The statistical energy versus B *for* $\mu = 0.7\frac{meV^{\frac{1}{2}}}{nm}$, $\lambda = 3 * 10^{-4}\frac{meV}{nm^4}$, $\alpha_R = 0$ *and without impurity at* $T = 0, F = 0$ *and* $F = 1.5\ mV/nm$

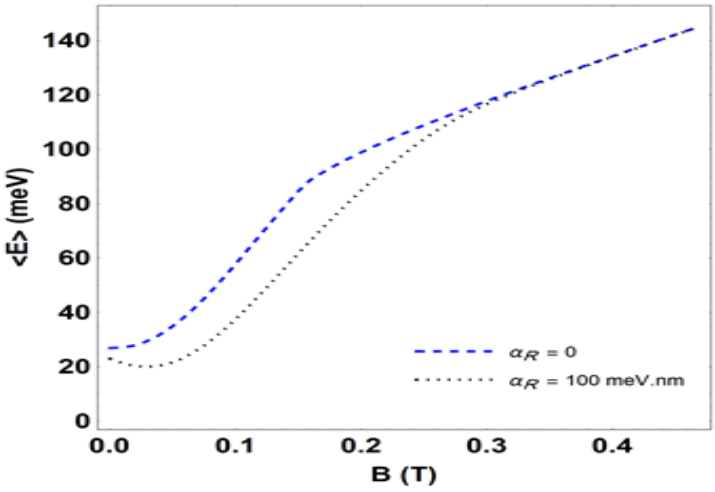

Figure 13

The statistical energy versus B for $\mu = 0.7\frac{meV^{\frac{1}{2}}}{nm}$, $\lambda = 3 * 10^{-4}\frac{meV}{nm^4}$, $F = 0$, *and without impurity at* $T = 0$, $\alpha_R = 0$ *and* $\alpha_R = 100\ meV.nm$

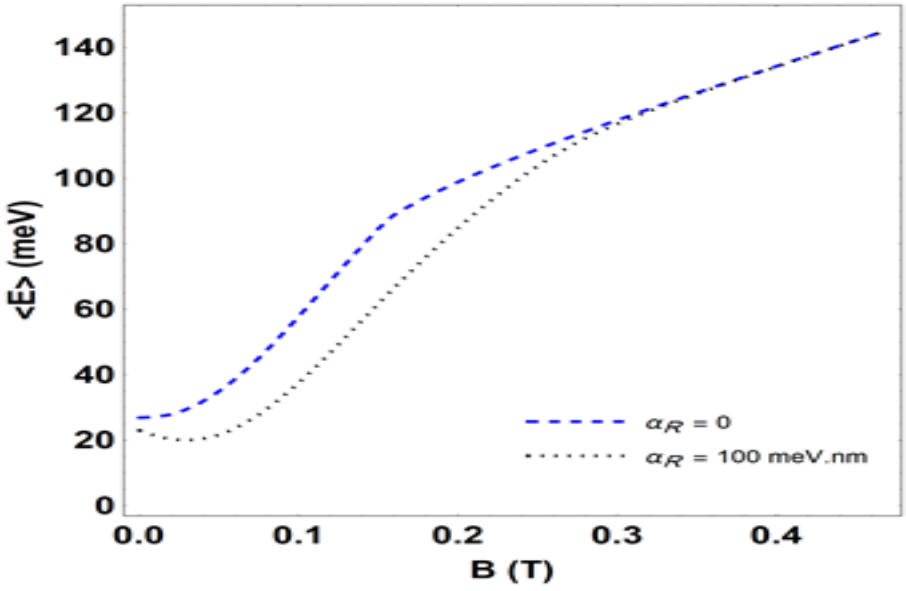

Figure 14

The magnetization versus B for $\mu = 0.7\frac{meV^{\frac{1}{2}}}{nm}$, $\lambda = 3 * 10^{-4}\frac{meV}{nm^4}$, $F = 0$, $\alpha_R = 0$ *and without impurity at* $T = 0$ *and* $T = 200\ K$

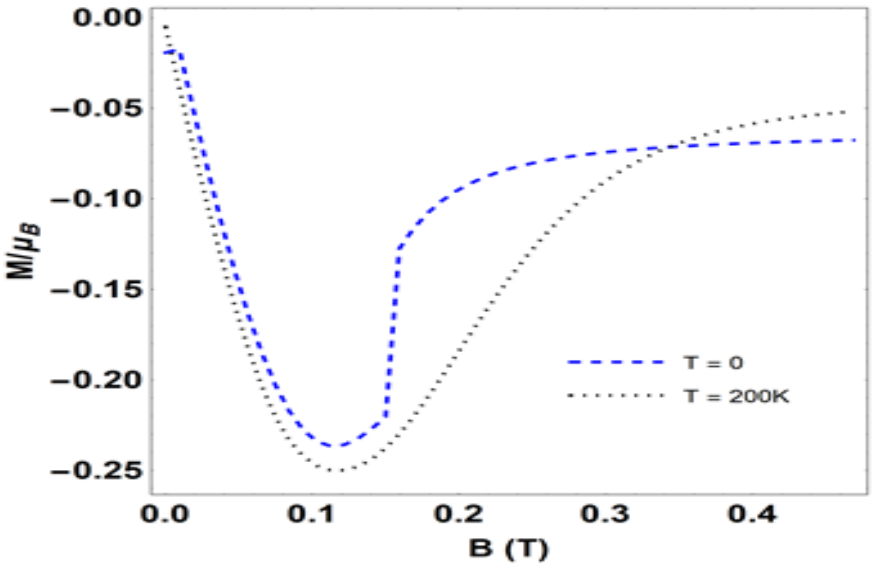

Figure 15

The magnetization versus B for $\mu = 0.7\frac{meV^{\frac{1}{2}}}{nm}$, $\lambda = 3 * 10^{-4}\frac{meV}{nm^4}$, $\alpha_R = 0$ *and without impurity at* $T = 0$, $F = 0$ *and* $F = 1.5\ mV/nm$

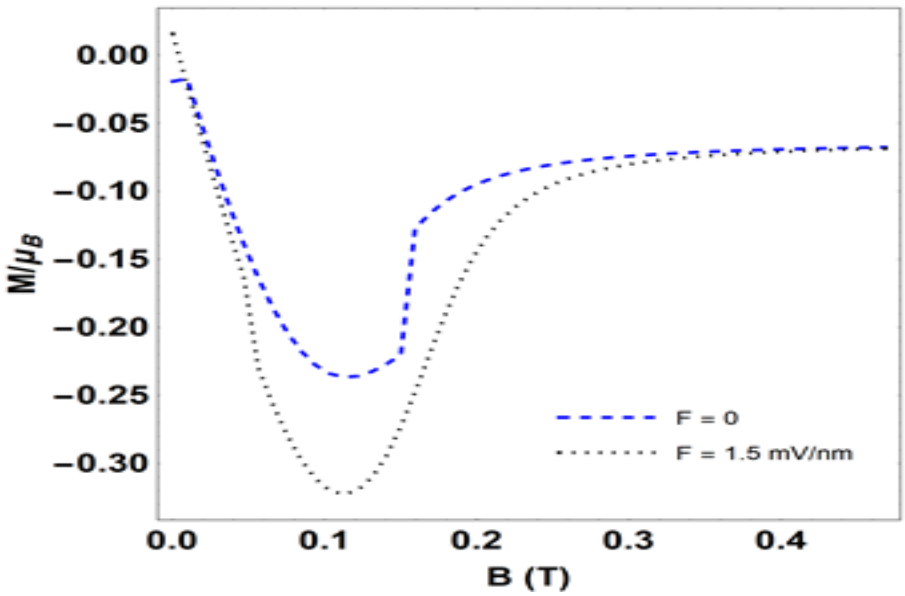

Figure 16

The magnetization versus B for $\mu = 0.7\frac{meV^{\frac{1}{2}}}{nm}$, $\lambda = 3 * 10^{-4}\frac{meV}{nm^4}$, $F = 0$ *and without impurity at* $T = 0$, $\alpha_R = 0$ *and* $\alpha_R = 100\ meV.nm$

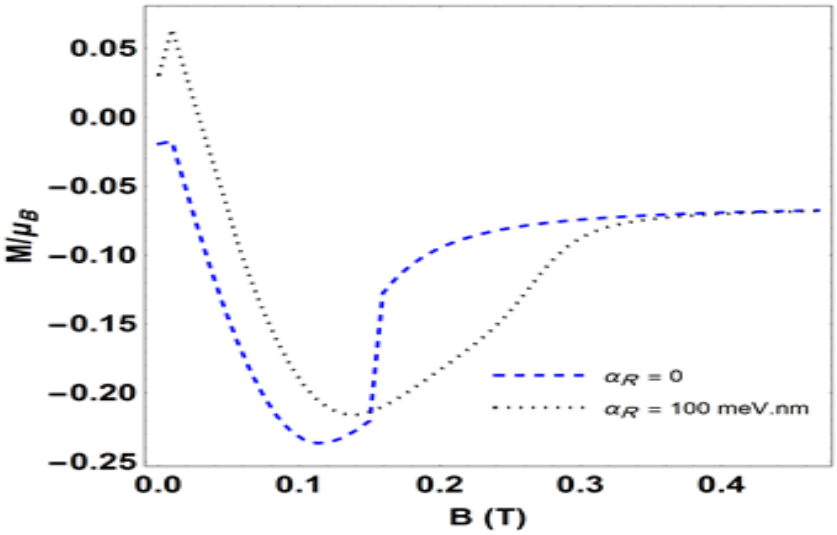

Figure 17

The magnetic susceptibility versus B for $\mu = 0.7\frac{meV^{\frac{1}{2}}}{nm}$, $\lambda = 3 * 10^{-4}\frac{meV}{nm^4}$, $F = 0$, $\alpha_R = 0$ *and without impurity at* $T = 0$ *and* $T = 200\ K$

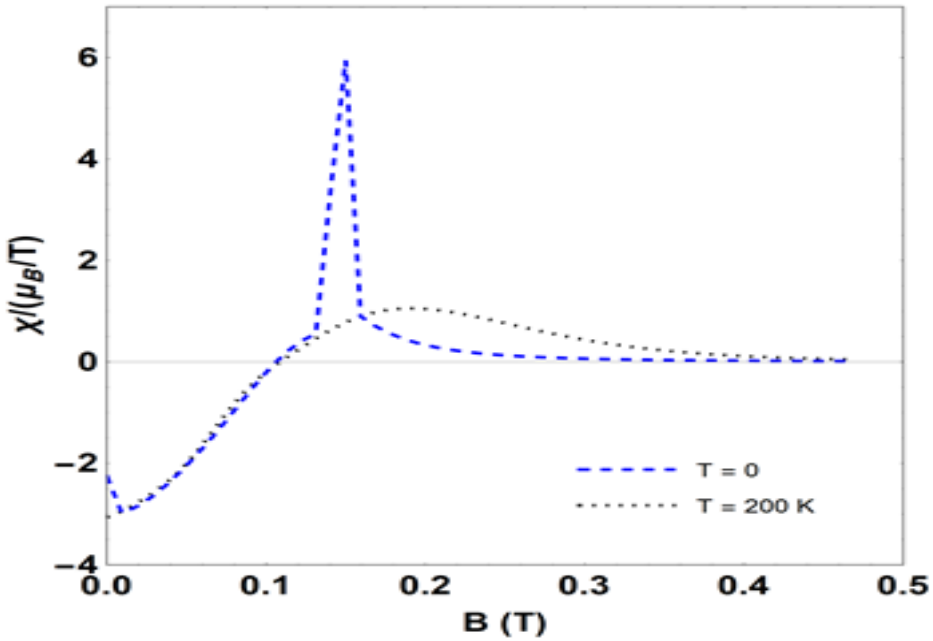

Figure 18

The magnetic susceptibility versus B for $\mu = 0.7\frac{meV^{\frac{1}{2}}}{nm}$, $\lambda = 3 * 10^{-4}\frac{meV}{nm^4}$, $\alpha_R = 0$ *and without impurity at* $T = 0$, $F = 0$ *and* $F = 1.5\ mV/nm$

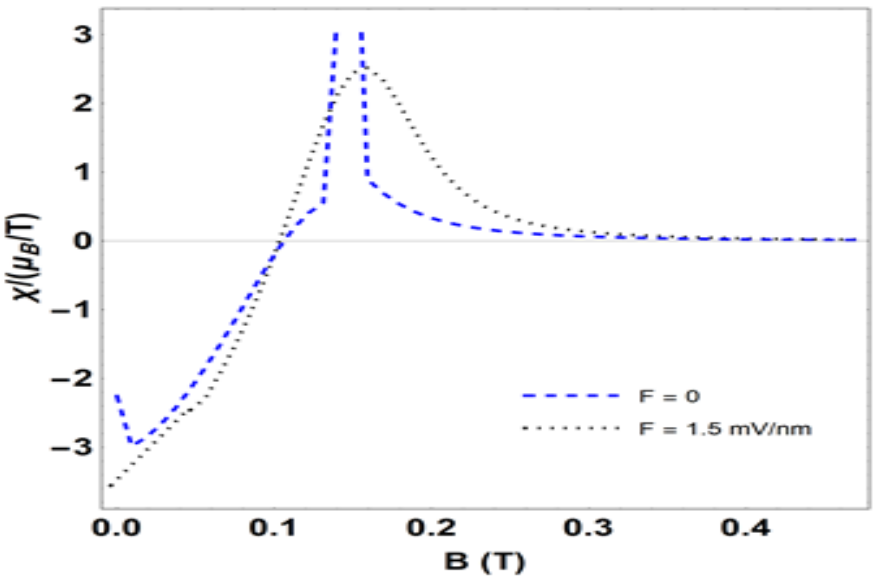

Figure 19

The magnetic susceptibility versus B for $\mu = 0.7\frac{meV^{\frac{1}{2}}}{nm}$, $\lambda = 3 * 10^{-4}\frac{meV}{nm^4}$, $F = 0$, *and without impurity at* $T = 0$, $\alpha_R = 0$ *and* $\alpha_R = 100\ meV.nm$

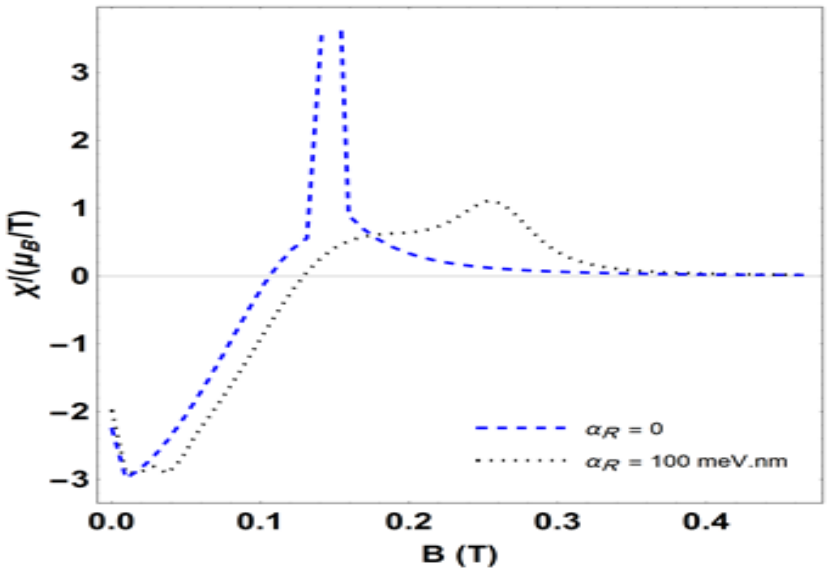

Figure 20

The magnetic entropy versus T *for* $\mu = 0.84\frac{meV^{\frac{1}{2}}}{nm}$, $\lambda = 3 * 10^{-4}\frac{meV}{nm^4}$, $F = 0$, $\alpha_R = 0$ *and without impurity at* $B = 0$ *and* $B = 0.05\ T$

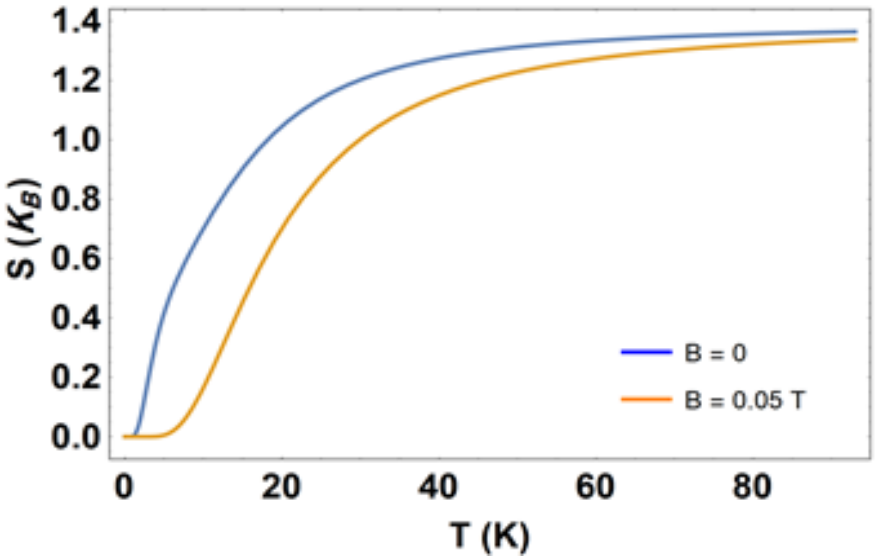

Figure 21

The magnetic entropy change versus T for $\mu = 0.84\frac{meV^{\frac{1}{2}}}{nm}$, $\lambda = 3 * 10^{-4}\frac{meV}{nm^4}$, $F = 0$, $\alpha_R = 0$ *and without impurity at* $different\ \Delta B$ *values*

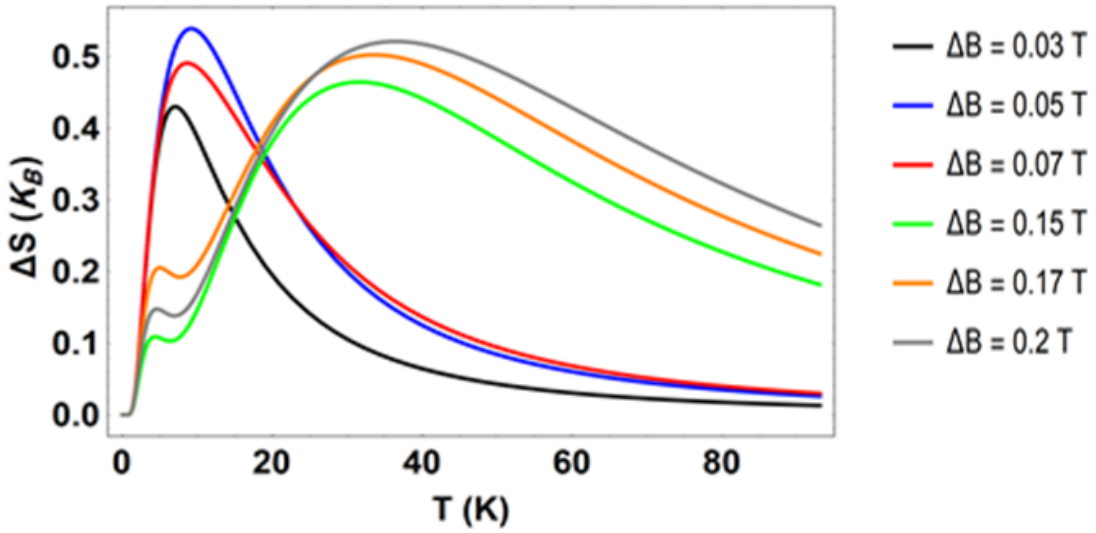

Figure 22

The refrigerant capacity versus α_R *for* $\mu = 0.84\frac{meV^{\frac{1}{2}}}{nm}$, $\lambda = 3 * 10^{-4}\frac{meV}{nm^4}$, $F = 0$, *and without impurity. at* $\Delta B = 0.2\ T$ *for* $T_{cold} = 0$ *and* $T_{hot} = 75\ K$

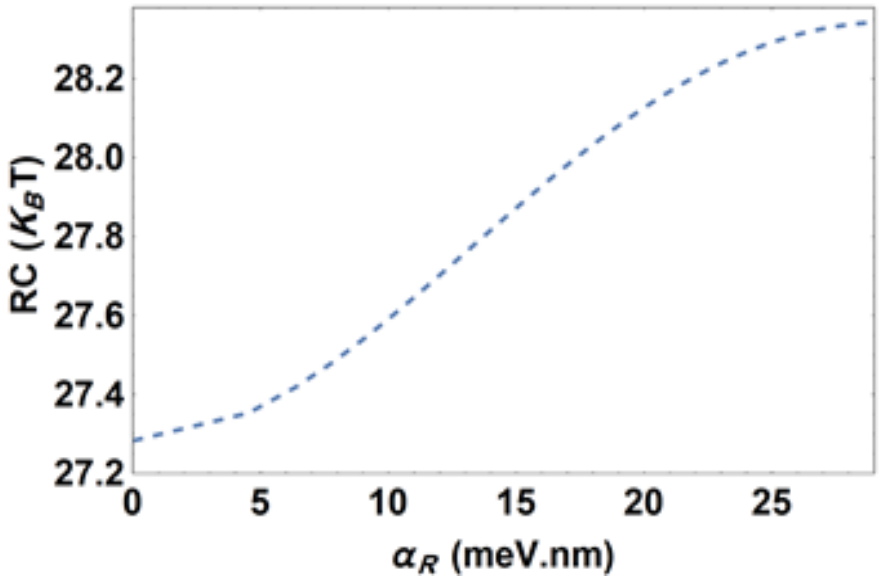

Figure 23

The refrigerant capacity versus the impurity position for $= 0.84\frac{meV^{\frac{1}{2}}}{nm}$, $\lambda = 3 * 10^{-4}\frac{meV}{nm^4}$, $F = 0$, $\alpha_R = 0$, $V_0 = 80\ meV$ *and* $d = 8\ nm$. *at* $\Delta B = 0.2\ T$ *for* $T_{cold} = 0$ *and* $T_{hot} = 75\ K$

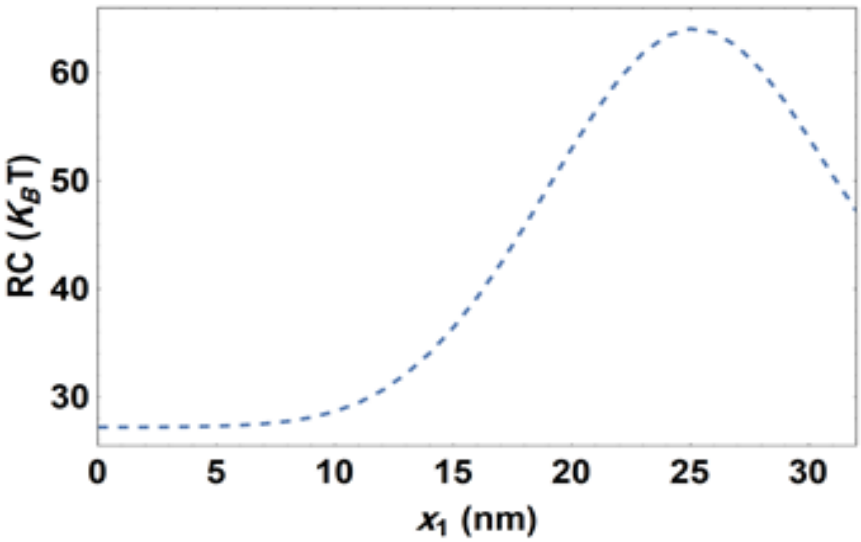

Figure 24

The refrigerant capacity versus the impurity strength for $= 0.84\frac{meV^{\frac{1}{2}}}{nm}$, $\lambda = 3 * 10^{-4}\frac{meV}{nm^4}$, $F = 0$, $\alpha_R = 0$, $x_1 = 25\ nm$ *and* $d = 8\ nm$. *at* $\Delta B = 0.2\ T$ *for* $T_{cold} = 0$ *and* $T_{hot} = 75\ K$

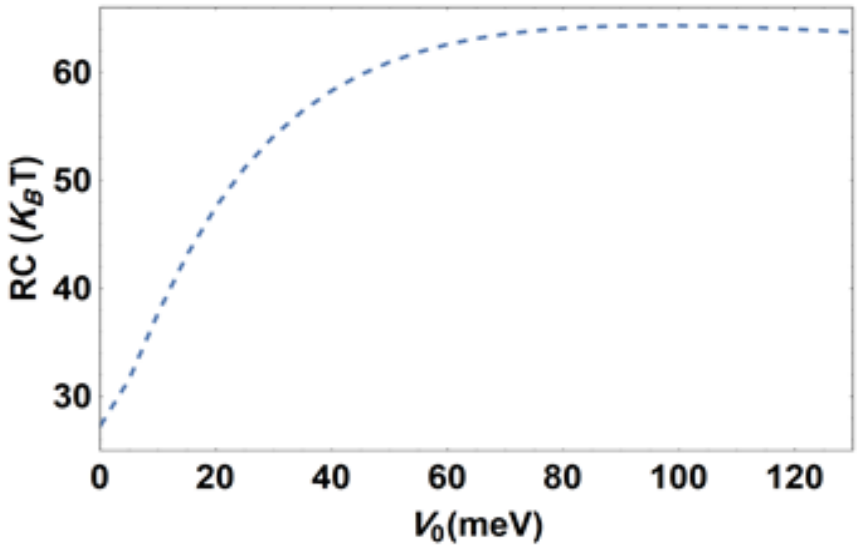

Figure 25

The refrigerant capacity versus F for $\mu = 0.84 \frac{meV^{\frac{1}{2}}}{nm}$, $\lambda = 3 * 10^{-4} \frac{meV}{nm^4}$, $\alpha_R = 0$ *and without impurity. at* $\Delta B = 0.2\ T$ *for* $T_{cold} = 0$ *and* $T_{hot} = 75\ K$

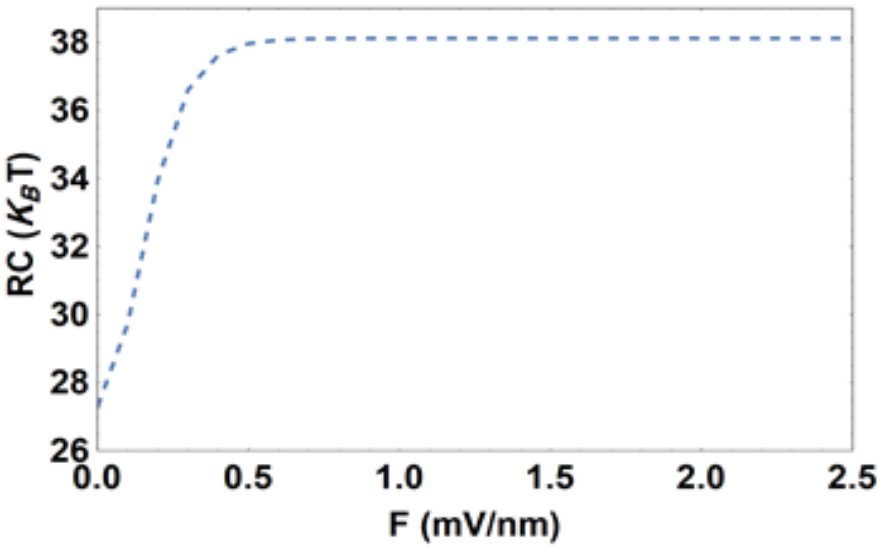

Figure 26

The effect of the dimensionality on the density of states yields a different change in the system properties

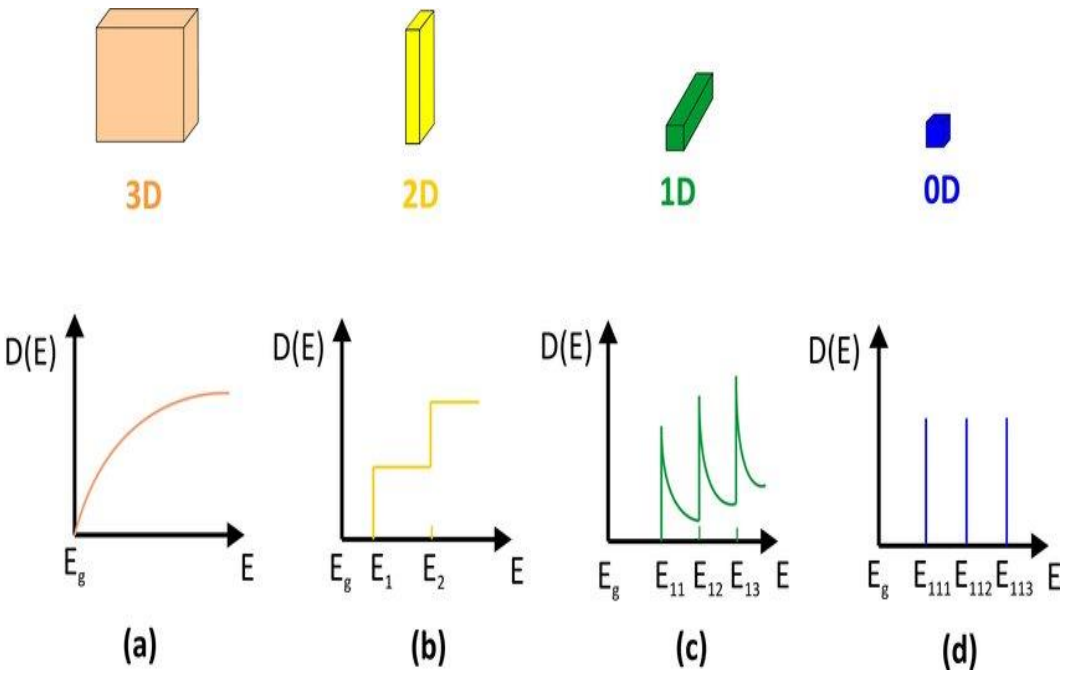

Figure 27

STM one-dimensional tunneling configuration

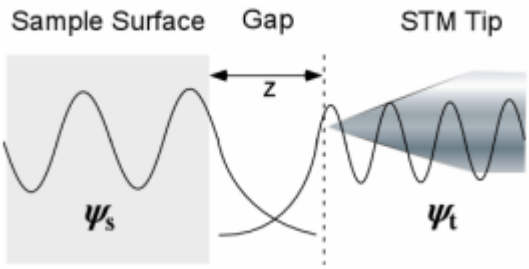

Figure 28

Metal-insulator-metal tunneling junction

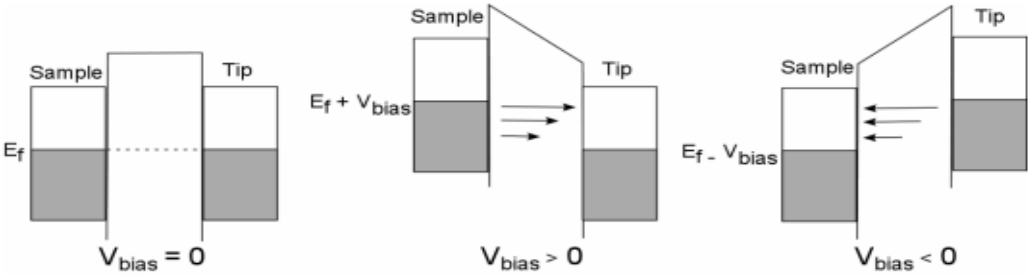

Figure 29

Metal-insulator-semiconductor tunneling junction

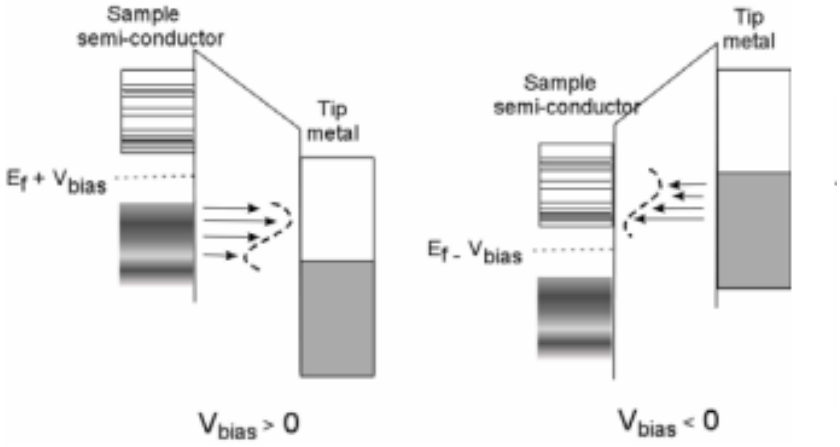

Figure 30

The magnetocaloric effect

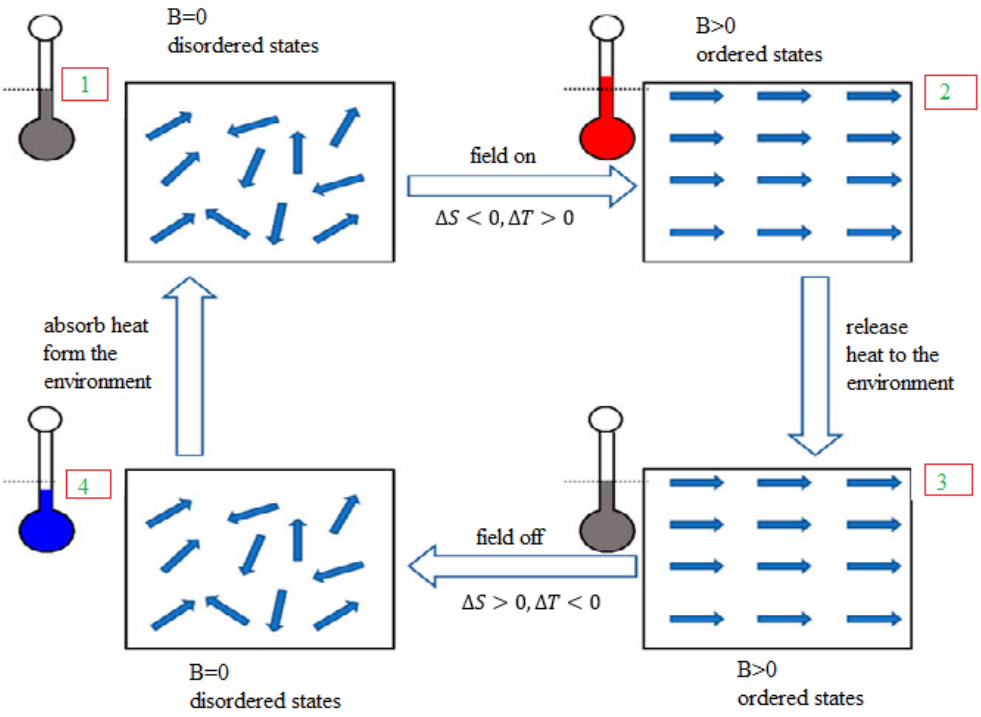

جـامعـــة النجاح الوطنية
كليـــة الدراســـات العليـــا

التأثير المغناطيسي الحراري والخصائص الإلكترونية لسلك كمي مزدوج مع وجود شوائب ومجالات كهربائية ومغناطيسية خارجية

إعداد
محمود ماجد محمود علي

إشراف
أ. د. محمد خليل السعيد

قدمت هذه الأطروحة استكمالا لمتطلبات الحصول على درجة الدكتوراه في الفيزياء، من كلية الدراسات العليا، في جامعة النجاح الوطنية، نابلس– فلسطين.

2025

التأثير المغناطيسي الحراري والخصائص الإلكترونية لسلك كمي مزدوج مع وجود شوائب ومجالات كهربائية ومغناطيسية خارجية

اعداد

محمود ماجد محمود علي

إشراف

أ. د. محمد خليل السعيد

الملخص

تقدم هذه الأطروحة دراسة نظرية شاملة للخصائص الإلكترونية والمغناطيسية والحرارية لسلكين كموميين مزدوجين (DQW) مصنوعين من إنديوم أنتيمونيد (InSb)، المعروف بحرية حركة الإلكترون العالية وارتباط الغزل والمدار القوي. تُحلل الدراسة تأثير معاملات جهد الحصر، وارتباط راشبا، والحقول الكهربائية والمغناطيسية الخارجية، والشوائب الجاوسية على هذه الخصائص في النظام.

تم حل دالة هاميلتون باستخدام طريقة التقسيم القطري الدقيق، واستُخرجت أطياف الطاقة، والكثافة الموضعية لمستويات الطاقة (LDOS)، وقابلية المغنطة، والاعتلاج، والتأثير المغناطيسي الحراري (MCE) للنظام.

تُظهر النتائج أن الشوائب تُحدث تعديلاً كبيرًا في البنية الإلكترونية، مما يسبب انزياحًا في مستويات الطاقة وكسرًا في التماثل بين السلكين، مع انزياح انتقائي لطيف أحد السلكين. كما يظهر الانقسام في مستويات الطاقة وإعادة توزيع كثافة الاحتمال أن الحقول الخارجية توفر وسيلة فعالة لضبط الخصائص الإلكترونية.

تم توضيح تأثير ارتباط راشبا على LDOS وقابلية المغنطة، وتحليل القابلية المغناطيسية كدالة للمجال المغناطيسي. كما دُرس تأثير درجة الحرارة، وقوة راشبا، والمجال الكهربائي على الخواص المغناطيسية، حيث لوحظ انتقال النظام من السلوك الديامغناطيسي إلى البارامغناطيسي.

دُرس التأثير المغناطيسي الحراري (MCE) من خلال حساب التغير في الاعتلاج (ΔS) نتيجة تغير المجال المغناطيسي الخارجي، إضافة إلى تحليل سعة التبريد (RC)، وهي كمية تحدد انتقال الحرارة بين وسطين خلال دورة التبريد. تُظهر النتائج أن RC تزداد لا خطيًا مع زيادة معامل راشبا(α_R)، مما يؤكد تأثير راشبا على كفاءة نقل الحرارة.

تشير الدراسة إلى أن وجود الشوائب في مواضع محددة، وزيادة المجال الكهربائي حتى قيمة معينة، يُعززان من RC، بينما لا تؤدي الزيادة الإضافية في شدة المجال الكهربائي إلى تحسينات إضافية.

يُظهر البحث أن تأثير راشبا، وتوزيع الشوائب، وشدة المجال الكهربائي يؤثر بشكل كبير على الخصائص الإلكترونية والمغناطيسية والحرارية للأنظمة النانوية. تقدم هذه النتائج رؤية قيمة لتحسين المواد ذات التأثير المغناطيسي الحراري من خلال ضبط ارتباط الغزل والمدار، والتحكم في الشوائب، وتطبيق المجالات الكهربائية الخارجية. هذه التعديلات تتيح إمكانية التحكم في تأثير التبريد المغناطيسي، مما يجعل هذه المواد واعدة للتطبيقات التكنولوجية المتقدمة.

الكلمات المفتاحية: سلك كمومي مزدوج، ارتباط الغزل والمدار، شائبة جاوسية، الكثافة الموضعية لمستويات الطاقة، المغنطة، القابلية المغناطيسية، التأثير المغناطيسي الحراري، جهد الحصر، الاعتلاج، سعة التبريد.